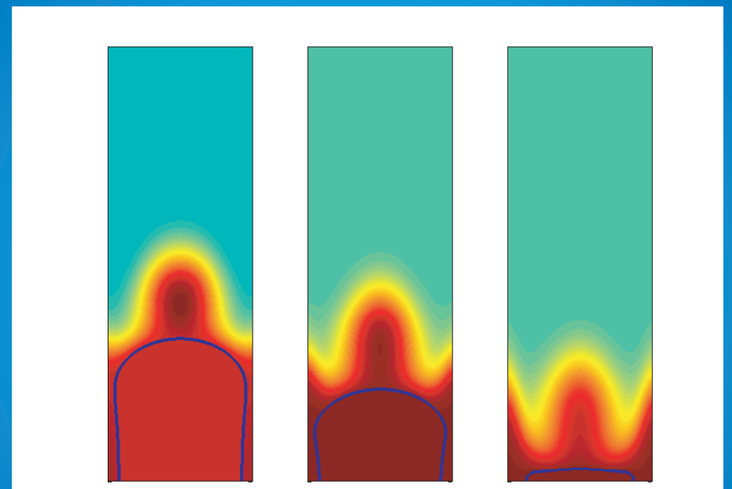

Vapor Bubbles in Confined Geometries: A Numerical Study Edip Can

Vapor Bubbles in Confined Geometries:

A Numerical Study

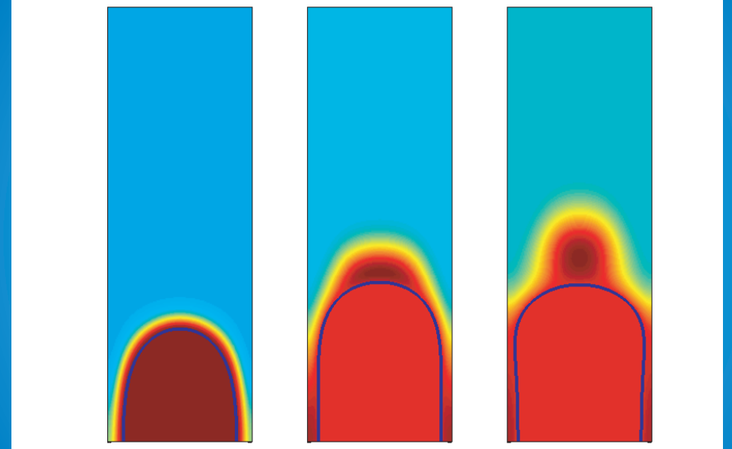

Edip Can

UITNODIGING

voor het bijwonen van
de verdediging van mijn
proefschrift, getiteld

Vapor Bubbles in
Confined Geometries:
A Numerical Study

welke zal plaatsvinden
op woensdag 12 mei 2010
om 16.30 collegezaal 4
van gebouw de Waaier
Universiteit Twente
Enschede

Vanaf 21.00 uur bent u
uitgenodigd voor het
feest in restaurant
Markanti
aan de Brinkstraat 7-B
in Hengelo

e.can.80@gmail.com

Vapor Bubbles in Confined Geometries: A Numerical Study

Edip Can

Samenstelling promotiecommissie:

Prof. dr. G. van der Steenhoven (voorzitter, secretaris)	Universiteit Twente
Prof. dr. A. Prosperetti (promotor)	Universiteit Twente
Prof. dr. rer. nat. D. Lohse (promotor)	Universiteit Twente
Prof. dr. J.A.M. Kuipers	Universiteit Twente
Prof. dr. B.J. Geurts	Universiteit Twente
Prof. dr. -ing N.A. Adams	Technische Universität München
Prof. dr. A.E.P. Veldman	Rijksuniversiteit Groningen
Prof. dr. ir. L. van Wijngaarden (vervangend voorzitter)	Universiteit Twente

The work in this thesis was carried out at the Physics of Fluids group of the Faculty of Science and Technology of the University of Twente.

Nederlandse titel:
Dampbellen in begrensde geometriën: een numerieke studie.

Publisher:
Edip Can, Physics of Fluids, University of Twente,
P.O. Box 217, 7500 AE Enschede, The Netherlands
pof.tnw.utwente.nl

Cover design: Edip Can
Front cover illustration: Numerical simulation of a vapor bubble expanding in a microtube depicting the bubble shape and temperature field at three separate instants.(see chapter 6)
Back cover illustration: Numerical simulation of a vapor bubble collapsing in a microtube depicting the bubble shape and temperature field at three separate instants. (see chapter 6)
Print: Gildeprint, Enschede

ISBN 978-90-365-3030-9

VAPOR BUBBLES IN CONFINED GEOMETRIES: A NUMERICAL STUDY

PROEFSCHRIFT

ter verkrijging van
de graad van doctor aan de Universiteit Twente,
op gezag van de rector magnificus,
prof. dr. H. Brinksma,
volgens besluit van het College voor Promoties
in het openbaar te verdedigen
op woensdag 12 mei 2010 om 16.45 uur

door

Edip Can

geboren op 10 Juni 1980

te Enschede

Dit proefschrift is goedgekeurd door de promotoren:
Prof. dr. A. Prosperetti
Prof. dr. rer. nat. Detlef Lohse

Contents

1 Introduction

Phase change phenomena are ubiquitous in our lives. From boiling water to make a nice cup of coffee to producing the vapor that drives the turbines which currently produce most of the world's electrical energy, liquid-to-vapor phase change occupies a prominent - indeed vital - position in society. Driven by the plethora of industrial and engineering applications, boiling has been the subject of intense study for many decades. Numerous empirical correlations have been developed for particular boiling stages and surface geometries, but, though necessary and useful, such correlations do not explain the fundamental physical processes governing the various phenomena encountered in boiling as stressed in several recent reviews [1, 2].

The fundamental entity in the boiling process is a single vapor bubble forming in a region of superheated liquid. Its growth proceeds in three stages. The initial growth phase is restrained by surface tension. If the liquid superheat is not too small, this initial phase is followed by an inertial-controlled stage. This was first studied by Lord Rayleigh who was the first to put to practical use an existing equation of motion for a cavity in an unbounded liquid [3], neglecting viscosity and surface tension. The bubble radial growth rate in this stage is constant in time. Finally, the growth becomes heat-transfer-limited, by which time it proceeds as $dR/dt \propto \sqrt{t}$, with R the bubble radius. This stage was studied in [4, 5] where Rayleigh's equation coupled with the energy equation was solved, thereby taking into account the temperature dependency of the bubble pressure. Subsequently, these two limits were connected in [6] where a general relation for spherical bubble growth in a uniformly superheated liquid was

derived. Experimental studies [7] have corroborated the asymptotic solutions.

While very interesting, these results had limited applicability due to the idealization of the absence of boundaries. The importance of boundaries has increased due to the recent interest in vapor bubbles for microfluidic applications. Here the primary objective is the precise control and manipulation of liquids on the submillimeter scale. Typical components for which there is a widely recognized need are, among others, pumps, valves and actuators. Due to the small sizes microfluidic devices typically operate in the low-Reynolds-number regime where viscous forces dominate. In this regime it is difficult to achieve the desired goals. Rapidly growing vapor bubbles have proven to be useful tools that are able to overcome this limitation because flow speeds of the order of meters per second are easily reached. Furthermore, the complete process of growth and collapse of the bubble is rapid enough to allow for high repetition rates. Perhaps the most widely known and most successful example is the development of ink-jet printing [8–11], in which the rapid growth of a vapor bubble in a narrow passage produces and ejects a droplet of ink. Due to the fast bubble dynamics this process is repeated a few thousand times each second. This is certainly not the only application. Various actuators based on the fast dynamics of a vapor bubble, nucleated on an impulsively heated element, have been designed, resulting in displacements in the micrometer range and frequencies up to several kHz [12, 13].

Another illustration of the use of vapor bubbles is the development of micro pumps. Tsai and Lin [14] developed such a pump. In their design an oscillating bubble creates an aperiodic flow which is given a preferred direction through the chip geometry. In [15] a similar concept is used. Here a vapor bubble is periodically generated in a long channel. The bubble is created away from the center, resulting in a net flow towards the longer half of the channel. A different mechanism to achieve pumping is described in [16] where a focussed laser pulse is used to create a cavitation bubble near a rigid boundary. During collapse of a cavitation bubble near a boundary typically a jet is formed directed towards the boundary. By fabricating a hole in the boundary at the position where the jet would hit, this mechanism is used to pump liquid through the hole.

These are but a few examples of utilization of vapor bubble in microfluidics. Several others applications include e.g. switching [17], mixing [18] and surface cleaning [19].

The underlying principle of these applications is fairly simple. However, a complete understanding of the growth and collapse of the bubble in these conditions is far from trivial. Several models for the behavior of confined vapor bubbles have been developed [8, 20] which had to rely on many simplifying assumptions. Despite the relative success of these models, it is clear that the full complexities of the problem

cannot be captured by simplified modeling. The highly transient bubble shape, complex geometries, thermo-mechanical coupling, viscous and surface tension effects, evaporation and condensation must all be accounted for if a good understanding of this fascinating and useful system is to be acquired.

The development of numerical methods capable of solving the governing equations of two-phase flows, including the motion of interfaces and phase change, has reached a level of maturity and advancement that their usage offers a promising avenue for studying the dynamics of vapor bubbles in various circumstances. One of the main challenges to overcome in this type of problems is transporting the phase boundary with the flow velocity. This is also the feature in which the various methods differ most from each other. For this reason, we give a short overview of the basic ideas employed in some of the most commonly used methods for the representation and transport of the interface; for recent more detailed literature see [21–25]

1.1 Numerical methods for two phase flows

Many different methods have been developed for the direct numerical simulation of gas-liquid flows. The various methods can be broadly divided into two approaches, depending on the nature of the grid used.

Moving grid methods

One approach is the use of moving grids. In these methods the phase interface coincides with a grid line. This greatly facilitates the application of the interface conditions. One example of a structured moving grid is the body fitted grid. In [26, 27] the steady state shapes of axi-symmetric buoyant bubbles were computed. This development brought the method to the attention of a wider fluid dynamics community. Accurate results can be obtained with this method, but its application is limited to relatively simple interface configurations because of the difficulty of grid generation in complex situations and, in particular, in three dimensions. Another example of this type is the unstructured finite-element grid [28], usually consisting of triangular elements in two dimensions and tetrahedral in three dimensions. This method offers flexibility because of its ability to tackle complex geometries. An additional advantage is the fact that the grid resolution can be locally varied within the computational domain so that small flow structures can be accurately resolved without unnecessary increase in the overall computational effort. The method however is complex in its implementation and computationally expensive due to the need to generate a new grid at every time step.

The use of structured fixed grids is preferable due to their flexibility, efficiency and ease of implementation. In these methods the governing equations are solved on a stationary grid while the interface moves through it. Here, the challenges are twofold. One is the representation and advection of the phase boundary. The second one is the treatment of the interface conditions.

Two philosophies for the representation of an interface may be identified: explicit tracking by means of markers on the interface, or implicit capture by means of a marker function.

Front tracking

In front tracking the interface (or front) is represented by connected marker points that move with the fluid flow. The first use of such marker points in the solution of the Navier-Stokes equations was for the purpose of computing surface tension effects [29, 30]. Unverdi and Tryggvason were the first to use the method for the advection of a boundary between two different fluids [23]. The advection of the interface is carried out in a Lagrangian fashion. For this purpose the velocity field is interpolated from the fixed grid locations to the locations of the surface markers. The advection scheme is not completely mass conserving. This is due to the fact that even though the discrete velocity field on the fixed grid is divergence-free, the interpolated velocity field may not be divergence-free.

As the front moves, it may deform and stretch. The resolution of some parts of the front can become too low, while other parts may become crowded with markers. To maintain accuracy, either additional markers must be added when their separation becomes too large or existing markers must be redistributed or deleted. These procedures of restructuring the grid can be rather complex to implement in three dimensions because, in addition to adding and removing markers, one must consider the connectivity and shape of the resulting discretization of the front.

One of the major drawbacks of the front-capturing method is the fact that changes in interface topology caused e.g. by coalescence or break-up, are not handled automatically. Instead, such changes must be accounted for by changing the connectivity of the markers in an appropriate way. In two dimensions the merging of interface is easily treated by merging two interfaces if their separation is less than one grid spacing. Again, in three dimensions this becomes much more difficult.

In spite of these shortcomings, front tracking can give very accurate results and impressive simulations have been performed.

Volume of fluid

The Volume of Fluid (VOF) method is one of the earliest methods developed for two-phase flows. It evolved from the Marker and Cell method [31]. In the VOF method the interface is captured implicitly by a function, F known as the volume fraction. It represents the amount of fluid within a computational cell. For a cell completely filled with phase I it is $F = 1$, while $F = 0$ for a cell completely filled with phase II. A cell cut by the interface has $0 < F < 1$. The transport of the interface by the fluid flow is described by the advection equation

$$\frac{\partial F}{\partial t} + \nabla \cdot (\mathbf{u}F) = 0\,. \tag{1.1}$$

Before the interface can be advected, it must first be reconstructed from the volume fraction function. This means that for each computational cell cut by the interface, an approximation must be found to the section of the interface within that cell. This must be carried out using information from the volume fraction at that particular cell and its neighbors. The earlier VOF methods [32, 33] used a simple lines interface calculation (SLIC) for the reconstruction procedure, in which the interface segments within the cut cells were aligned with the grid lines. This method results in a rather crude interface reconstruction and upon advection, even with relatively simple flows such as solid body rotations, many small non-physical satellite droplets are formed. A more accurate reconstruction results from fitting the interface with piecewise linear segments (PLIC) [34, 35].

The VOF method has several features that are advantageous with respect to other methods, the most important one being that the method is inherently mass conserving due to an advection algorithm based on a discrete representation of the conservation law. Furthermore, changes in interface topology are handled automatically by the method so that there is no need for outside interventions.

However, the reconstruction of the interface is a major drawback of the method, which is further amplified when considering its implementation in three dimensions. Additionally, due to the relative crudeness of the interface reconstruction, it is difficult to account for surface tension effects accurately as an accurate curvature computation is needed for this purpose.

Level Set Method

The level set method is another example of front capturing, introduced by Osher in 1988 for computing the motion of interfaces [36]. Here the interface is implicitly embedded as the zero level set of a continuous function, known as the level set function,

ϕ, defined in principle over the whole computational domain. Typically, ϕ is taken as a signed distance function, which gives the shortest signed distance from a point in the computational domain to the interface. This choice is made because large and small gradients are best avoided for accurate numerical treatment. The advantage of having a continuous function is that the interface normal vectors and curvature can be accurately computed from ϕ through the expressions

$$\mathbf{n} = \frac{\nabla\phi}{|\nabla\phi|}, \quad \kappa = \nabla \cdot \mathbf{n}. \tag{1.2}$$

The level set function is updated by solving the advection equation

$$\frac{\partial\phi}{\partial t} + \mathbf{u} \cdot \nabla\phi = 0. \tag{1.3}$$

Upon advection the signed distance character is lost, however, which can result in unwanted large gradients. For this reason ϕ is reinitialized back to a signed distance function at each time step [37–39]. Ideally, the reinitialization is performed without moving the zero level set, i.e. the interface. This however proves difficult to do in practice, and the repeated application of the reinitialization over the course of a simulation causes an unphysical loss of mass (or volume/area). Much work has focussed on improving this behavior [40–42]. As a result the level set method has been markedly improved and has been able to produce impressive results the past few years to the point of becoming competitive with the front tracking and VOF methods.

A major recent development has been the coupling of the volume-of-fluid and level-set methods, which combines the advantages of both [43, 44].

Diffuse vs. sharp interface

The equations expressing conservation of mass, momentum and energy can be formulated for the whole computational domain treating the different fluids as a single fluid with discontinuous physical properties at the interface. The main challenge in this so-called ”one-fluid approach” is to compute the terms concentrated at the interface, such as surface tension. These interface terms are computed using delta functions localized at the interface. Numerical treatment of sharp discontinuities is very problematic however. Therefore, to facilitate the numerical treatment, usually a certain thickness is assigned to the interface, typically a few grid cells, where the physical properties vary in a continuous fashion. The interface is therefore smeared, or diffuse.

The attraction of the ”one-fluid” approach is its simplicity and efficiency, which however one has to pay for by being satisfied with a lower accuracy. This inspired attempts to develop methods without smearing of the interface. In sharp interface methods, the governing equations are solved for each fluid separately, while matching the conditions at the interface. The previously mentioned body-fitted grid and the moving unstructured grid methods are examples of these attempts. Another, more recent, approach is to retain the stationary structured grid and improve the interface treatment by, for example, introducing special difference formulas that incorporate the jump across the interface [45–48]. One of these is the Ghost Fluid method, in which the jump conditions that hold at the interface are captured implicitly. For this purpose, the jump conditions, which can be computed explicitly, are used for defining a ”ghost fluid” on the other side of the interface, so that essentially the flow properties are continued across the interface as if the interface were not there. In this way the governing equations for this fluid in the neighborhood of the interface are discretized using the ”ghost fluid” values. This is carried out for both fluids separately.

Including phase change

The above methods have all been used for simulating bubbles and boiling. The first successful attempt was made in [49] where a fully deformable, two-dimensional (not axi-symmetric) bubble was simulated by means of a moving triangular grid. The simulations were limited to relatively short times however, due to the distortion of the grid. Similar problems were encountered in [50]. This limitation was overcome in [51] where a two-dimensional front tracking method was developed to study film boiling. The method used the ”one-fluid approach” and thus the interface was diffuse. Similar computations of film boiling were carried out using the VOF in [52] and Level Set method in [53], both using a diffuse interface. Three dimensional simulations of film boiling were carried out in [54]. Very recently, film boiling on an immersed solid surface has been simulated using the Level Set method together with the Ghost Fluid Method for a sharp interface treatment [55].

Bubble dynamics in confined geometries have also been studied numerically. In [56, 57] the growth and collapse of a vapor bubble in a narrow tube were studied by means of a front tracking method. The thermal aspects of the problem however were neglected: the bubble growth was initiated by applying a pressure pulse. The growth of a vapor bubble in a rectangular micro-channel was studied in [58] with a diffuse-interface level set method. Full simulation of a thermal ink jetting process was carried out in [59] with a level set method. Dynamics of vapor bubbles created on a micro heater were performed in [60] with a VOF method, treating the vapor as a cavity with uniform temperature and pressure.

1.2 Scope of the present work

The previous considerations demonstrate the interest suscitated by the problem of accurate numerical simulations of gas-liquid and vapor-liquid flows. Our contribution focuses on the latter problem and is motivated by possible applications in microfluidics.

We simplify the problem by neglecting the flow in the vapor phase, which only provides a constant pressure at the liquid interface equal to the saturation pressure at the interface temperature. This assumption limits the method to closed vapor volumes, but this is not a significant limitation in dealing with vapor bubbles. In exchange, the simplification that it permits enables us to represent the interface as sharp, which is of particular importance in a problem driven by phase change, the calculation of which requires a very accurate estimate of the interface temperature gradients.

We describe the interface by means of a level-set function which is advected by the liquid velocity over a fixed Cartesian grid under the assumption of axial symmetry. To avoid the use of irregular stencils we extrapolate the liquid velocity into the vapor region and make use of a procedure reminiscent of the ghost-fluid method to discretize the pressure Poisson equation.

To illustrate the method we consider the growth and collapse of vapor bubbles generated by the absorption of an intense laser pulse in a tube and between two parallel plates.

1.3 Guide through the thesis

To set the stage for the type of problems which motivate the work, in chapter 2 we study in simplified manner the dynamics of a vapor bubble growing and collapsing in a cylindrical micro-tube. We develop two models. The first one describes the system by including mechanical effects only. This model is found to be inadequate by comparison with experiment.The second model incorporates thermal effects and greatly improving the results.

In chapter 3 we describe the governing equations and interface conditions to be solved numerically. The governing equations are the liquid mass, momentum and energy equations. The vapor momentum is neglected in view of its small effect on the dynamics. The vapor energy balance is used to derive an equation for the temporal change of the surface temperature, from which the vapor pressure is computed. Thus, the role of the vapor is to set the temperature and pressure which act as interface conditions.

In chapter 4 we describe in detail the numerical method that has been implemented. Basically the method solves the liquid mass and momentum equations by means of a projection method on a fixed staggered grid. The moving phase interface is captured implicitly using the level set formulation. The pressure and temperature fields are solved with a known value, i.e. Dirichlet interface conditions, on the bubble surface. For accurately advancing the interface, a velocity extrapolation is performed satisfying the incompressibility constraint, while simultaneously imposing the zero tangential shear stress at the interface. For accurate computation of the bubble dynamics, the thermal gradients at the interface need to be computed accurately. For this reason the liquid temperature advection-diffusion equation is solved on a separate refined grid. Interpolation is used from the momentum grid to the thermal grid for quantities that are needed there. Various levels of refinement are implemented and grid independence is demonstrated.

Chapter 5 presents several test cases for the validation of the numerical method. We show results pertaining to the volume oscillations performed by a spherical bubble that is initialized with a radius larger than its equilibrium radius. The validation of the thermo-mechanical coupling is done by simulating of a collapsing vapor bubble in a subcooled liquid.

The bubble-in-tube of chapter 2 is studied again by means of the numerical method in chapter 6. Due to the computational demands of simulating the exact physical system we take a shorter tube in the numerical treatment. The dynamics resulting from the full solution of the governing equations are shown to be qualitatively similar. Furthermore, the bubble shapes and temperature fields are predicted by the method. It was already known that the particular choice of initial temperature field has a large effect on the subsequent dynamics. Here we perform the simulations with varying initial conditions in order to study its effect.

In chapter 7 we study the growth and collapse of a vapor bubble between two discs. We present experimental results and develop simplified models similar to those for the tube. For this system however these models are less satisfactory. The full numerical method is used for the direct simulation of this system. The main difference in results due to the different type of confinement is the bubble shape attained during the collapse. The rim of the bubble is shown to acquire a concave shape. By performing calculations based on geometrical optics we show that assuming a concave bubble shape as predicted by the simulations, typical intensity structures that are observed in experiments can be reproduced, thus corroborating the simulation prediction.

2

Growth and collapse of a vapor bubble in a microtube : the role of thermal effects *

2.1 Introduction

The dynamics of a free bubble have been studied extensively [61–63] due to their relevance for a wide range of phenomena. The first studies devoted to bubbles in confined geometries were motivated by the development of ink-jet printing technology [9–11]. This early interest has been subsequently sustained by the rapid development of microfluidics [see e.g. 64–66]. Other applications have focused on the actuation properties of rapidly growing and collapsing bubbles. For example, the high liquid velocity induced by transient bubbles has been used to provide high-Reynolds number flow in microsystems [19]. [67] and [56] have studied the dynamics of highly transient vapor bubbles in a tube and have demonstrated a pumping effect [15, 68]; see also [69, 70].

Here we study the growth and collapse of a vapor bubble inside a microtube both experimentally and theoretically. In previous studies [9, 15, 68], the vapor bubble was created using a thin-film heater at the tube surface. In the present work, the bubble is generated in the central region of a tube by focusing a laser pulse. The experiments

*Published as: [Chao Sun, Edip Can, Rory Dijkink, Detlef Lohse and Andrea Prosperetti, *Growth and collapse of a vapor bubble in a microtube : the role of thermal effects*, J. Fluid Mech.,2009].

are conducted varying the tube diameter and length and the laser energy. To increase heat absorption by the liquid, water mixed with dye is used.

The early models [15, 56, 68, 71] of these processes assumed that the high vapor pressure in the bubble caused by the initial heat pulse persisted only for a very short time and the subsequent dynamics was mostly governed by inertial and viscous effects. We find that these essentially mechanical models are inadequate to describe the observations and develop a new model which incorporates thermal effects.

2.2 Experimental setup

A sketch of the experimental setup, similar to the one used in the earlier experiments of [72], is shown in Fig.2.1. Two glass microtubes were used in the experiments, one with an inner diameter $D = 50$ μm, outer diameter 80 μm and length $L = 27$ mm, the other one with an inner diameter of 24.9 μm, outer diameter 80 μm and length 25 mm. For all experiments the same mixture of water and red food dye was used. The tubes were filled with the liquid, and both ends were covered by large droplets of the same solution (diameter ~ 5 mm) exposed at the atmosphere. The bubble was created at the midpoint of the microtube by focusing a laser pulse of a wavelength 532 nm (Nd:YAG laser, Solo PIV, New Wave, Fremont, CA, USA) with a time duration of 6 ns by means of a 40$\times$ objective. The energy of the laser varied from 27.6 μJ to 49.3 μJ for the $D = 50$ μm tube, and from 27.6 μJ to 56.3 μJ for the $D = 24.9$ μm tube. For calibrating energy, an energy meter (Gentec-eo XLE4) was positioned above the tubes. The energy absorbed by the working fluid was calibrated by measuring the difference of the reading of the meter with the empty glass tube and the glass tube filled with the working fluid. For the $D = 50$ μm tube, the absorbed energy varied from 6.5 μJ to 11.6 μJ. The energy absorbed by the liquid in the $D = 24.9$ μm tube varied from 3.0 μJ to 6.1 μJ.

A filter was used to block the reflected laser light to prevent damage to the camera. The motion of the bubble was recorded by a high speed camera with a maximum frame rate of 10^6 fps (HPV-1, Shimadzu Corp., Japan). In the experiments, 1.25×10^5 fps proved sufficient. The inter-frame and exposure times are 8 μs and 4 μs respectively. The maximum uncertainty of the bubble size due to blurring on a single frame is less than 5% when the velocity of the interface is maximum. Illumination for the camera was provided by a fiber lamp (Olympus ILP-1) emitting a light spectrum part of which passed through the filter to the camera. A digital delay generator (Model 555, Berkeley Nucleonics Corp. CA, USA) was used to synchronize the camera and the laser.

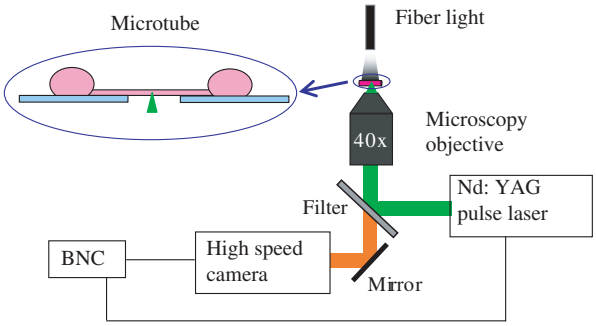

Figure 2.1: A sketch of the experimental setup.

2.3 Experimental results

Some representative frames taken during the evolution of the vapor bubble in the larger tube are shown in figure 2.2. The tube is initially full of water as shown in figure 2.2 (a). The vapor bubble appears rapidly at the midpoint of the tube after the liquid has absorbed 11.6 μJ from the laser pulse. The bubble is initially a small sphere (figure 2.2(b)), it expands spherically until it nearly occupies the whole diameter of the tube, after which preferential growth in the axial direction begins (figure 2.2(c)). The shape of the bubble changes approximately to that of a cylinder occupying the majority of the cross section of the tube (figures 2.2(c,d,e)). A very thin liquid film on the tube wall, as expected from the no-slip condition on a hydrophilic surface, is barely visible in these pictures but with insufficient detail for a quantitative study. The appearance of the bubble during the expansion (figure 2.2(c)) and collapse (figure 2.2(e)) is similar except for the final stage (figure 2.2(f)), where it differs appreciably from its shape at the moment of formation (figure 2.2(b)). The final shape is oblate and the motion remains very nearly one-dimensional until the very end because surface tension does not have the time to make the interface curved. Thus, the flow retains its approximately one-dimensional nature due to its brief duration [56], which makes a one-dimensional model a reasonable approximation.

By approximating the bubble as a cylinder, its length L_{bubble} along the axis of the tube and its diameter W can be extracted from the high-speed movies. The volume of the bubble is calculated as $V_{bubble} = \pi W^2 L_{bubble}/4$. Approximately the bubble volume in this way involves some error which is only appreciable in the first few frames. The estimated errors for figures 2 (b), (c) and (d) are 25%, 10% and 4% respectively. Since the system is symmetric with respect to the midpoint of the tube, we only consider half of the bubble. From here on, the bubble length is defined as

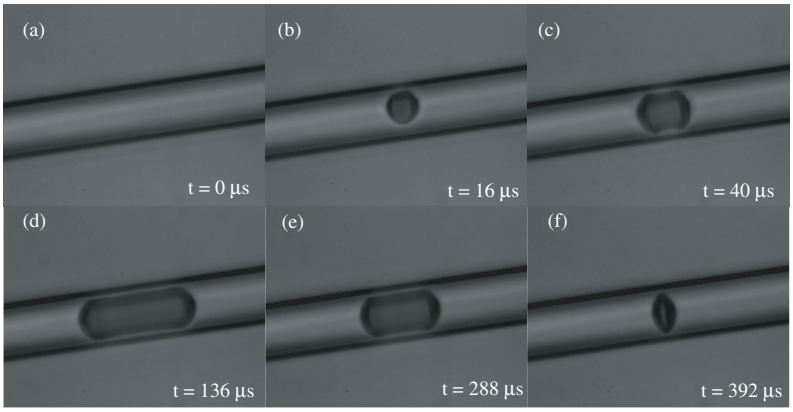

Figure 2.2: Representative frames of the vapor bubble evolution inside the microtube with an inner diameter 50 μm and length 27 mm; the absorbed laser energy is 11.6 μJ.

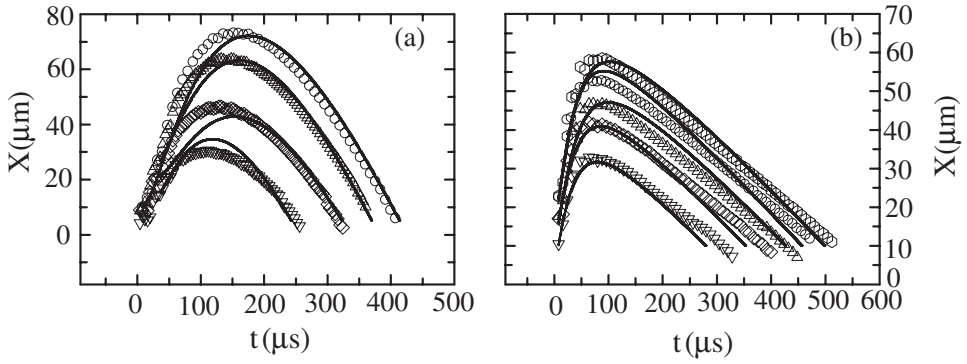

Figure 2.3: Time evolution of the bubble length X for different energy levels (a) in the tube with $D = 50$ μm; in descending order E = 11.6, 10.4, 8.2 and 6.5 μJ; (b) in the tube with $D = 24.9$ μm, for E = 6.1, 5.3, 4.8, 3.8 and 3.0 μJ. The open symbols are the experimental results and the lines are the results of the thermal model. See text for detailed parameters for the model.

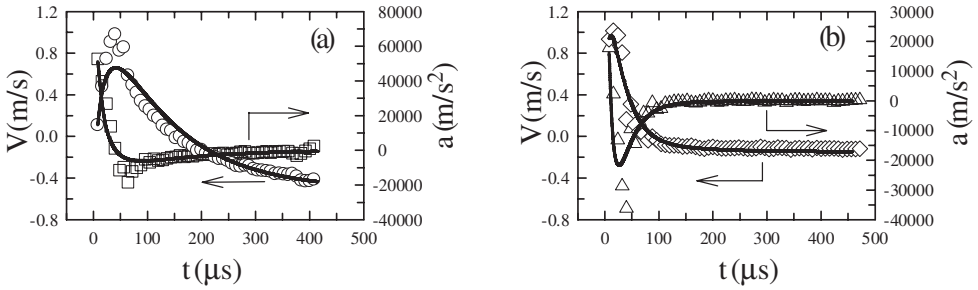

Figure 2.4: Velocity and acceleration of the interface versus time. (a) $D = 50\ \mu$m with $E = 11.6\ \mu$J, and (b) $D = 24.9\ \mu$m with $E = 5.3\ \mu$J. The open symbols are the experimental results and the lines the numerical results given by the thermal model.

$X = \frac{1}{2}V_{bubble}/(\pi D^2/4)$.

The time evolution of the measured bubble length X for different energy levels in the larger tube is plotted with open symbols in figure 2.3(a). In descending order, the absorbed energy is 11.6 μJ, 10.4 μJ, 8.18 μJ and 6.5 μJ. The maximum bubble size and its duration increase with increasing energy. The overall trends of the $X(t)$ curves for different energy levels are quite similar. The vapor bubble expands quickly, and shrinks more slowly after reaching its maximum size.

The contrast between growth and collapse is even sharper with the smaller tube. The bubble length versus time for different energy levels for this case is shown with open symbols in figure 2.3(b). More experimental runs were available with this tube and each $X(t)$ curve shown is the result of averaging three different experiments under the same nominal conditions. Shot-to-shot reproducibility was however good. In descending order, the absorbed energy is 6.1 μJ, 5.3 μJ, 4.8 μJ, 3.8 μJ and 3.0 μJ. Again, the maximum length and the duration of the bubble increase with increasing energy and the overall trends of the $X(t)$ curves for different energy levels are quite similar. However, the collapse of the bubble in this case proceeds much more slowly than its expansion. Unlike the larger tube case, the collapse process lasts about 10 times longer than the expansion.

To fit the measured $X(t)$, we used cubic splines from which the velocity and acceleration of the liquid/vapor interface can be extracted. The time dependence of the velocity in the larger tube is shown for E = 11.6 μJ by the circles in figure 2.4 (a). The velocity of the interface increases quickly to a maximum around 1 m/s at

$t \sim 40$ μs, and then decreases continuously to a minimum value around -0.4 m/s when the bubble disappears. The time dependence of the velocity in the smaller tube, for $E = 5.3$ μJ, is shown by the open diamonds in figure 2.4 (b). The velocity of the interface increases to around 1 m/s at $t \sim 16$ μs and then decreases continuously. The maximum velocity in the smaller tube is reached earlier than in the larger tube and the collapse velocity (0.2 m/s) is smaller than that in the larger tube (0.4 m/s). Since the very first instants of the bubble growth were too fast to be recorded, the first data readings that could be taken correspond to a finite velocity.

The acceleration of the interface is also shown in figure 2.4 (a). Here the squares are for the larger tube with $E = 11.6$ μJ. The acceleration begins with a huge value around 55,000 m/s^2, then immediately becomes negative down to around $-10{,}000$ m/s^2, and finally increases again to a very small value. The huge value at the beginning is a remarkable feature which may be potentially useful in microfluidic systems. The acceleration of the interface in the smaller tube, with $E = 5.3$ μJ, is shown by the triangles in figure 2.4 (b). It begins with a positive value around 20,000 m/s^2, and decreases rapidly to a negative value around $-35{,}000$ m/s^2, after which it increases quickly to a very small value. The stronger deceleration for the thinner tube reflects the enhanced viscous forces on the small scale.

We now describe two simple theoretical models which are helpful to shed some light on these observations.

2.4 Theoretical models

As remarked before, the approximate one-dimensional nature of the bubble evolution suggests the possibility of using a simple one-dimensional model for its behavior which is sketched in figure 2.5. Here the left vertical line is the plane of symmetry at the midpoint of the tube which coincides with the center of the bubble. We are interested in the motion of the right vapor-liquid interface located at $X(t)$. If the pressure at the other end of the liquid column is a constant p_∞, the equation of motion of the liquid column in the tube is, approximately [71],

$$\ell_L \rho_L \frac{d^2X}{dt^2} \quad = \quad p_V(t) - P_\infty - \mathscr{R}\frac{dX}{dt}\,. \tag{2.1}$$

Here ℓ_L is the length of the liquid column, which we keep constant and equal to half of the tube length given the smallness of the the bubble; p_V is the vapor pressure in the bubble and $\mathscr{R}$ represents on approximation to the effect of viscous losses due to the wall. By approximating the flow in the tube as quasi-steady fully developed Poiseuille flow, we model this term as $\mathscr{R} = 32\mu\ell_L/D^2$, in which μ is the liquid

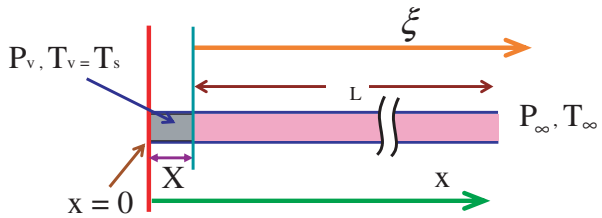

Figure 2.5: Conceptual sketch used in the formulation of the thermal model.

viscosity. This approximation is justified if the viscous diffusion length is comparable to, or larger than, the tube radius $D/2$, i.e. $2\sqrt{\nu\tau_b}/D \gtrsim 1$. With a bubble duration $\tau_b \simeq 400\ \mu$s and $D = 50\ \mu$m, this ratio is about 0.8. This value does not fully support the approximation, which will therefore tend to underestimate somewhat the true viscous loss. However the error may be expected to be moderate, which is supported by the results that will be shown later. Since the pressure inside the bubble is essentially uniform there is no pressure gradient to drive the flow in the film so that viscous dissipation in it can be neglected.

2.4.1 The step-function pressure model

In past work [see e.g. 56] the dynamics of the bubble was modeled including inertia and viscosity but neglecting thermal effects. The pressure inside the bubble was taken equal to the vapor pressure of the liquid at the initial undisturbed temperature, except for a short interval $0 \leq t < \Delta t$ during which it was given a large value $p_0 + \Delta p$. We can now compare the predictions of this model with our data.

This simple model has two free parameters, Δp and the duration of the overpressure Δt. As suggested by the data to be shown later, we take the initial high pressure $p_V = p_0 + \Delta p = 10^6$ Pa and fit Δt so as to match approximately the observed maximum elongation of the bubbles in figures 2.3. For the larger tube (D =50 μm) and E = 11.6 μJ we take τ = 22 μs while, for the smaller tube (D =24.9 μm) with E = 5.3 μJ, we take τ = 25 μs. For $t > \Delta t$ the pressure inside the bubble falls to $p_V = p_V(25^\circ\text{C}) = 3.2 \times 10^3$ Pa. The initial bubble length for both cases was selected from experiment, $X(0) = 10\ \mu$m for $D = 50\ \mu$m and $X(0) = 20\ \mu$m for $D = 24.9\ \mu$m. The initial velocity for both cases was taken as 0.

The results of this step-function pressure model for the two cases are shown with the dashed lines in figure 2.6. The open symbols are the experimental data (a) $D =$ 50 μm with $E = 11.6\ \mu$J and (b) $D = 24.9\ \mu$m with $E = 5.3\ \mu$J. Although in a very general way some aspects of the observed bubble dynamics are reproduced, a

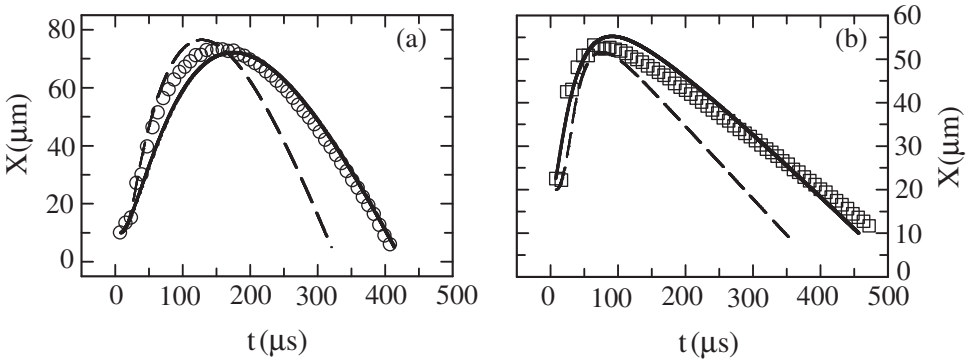

Figure 2.6: Comparison of the bubble length $X(t)$ vs. time as measured and predicted by the models for the cases (a) $D = 50$ μm and (b) $D = 24.9$ μm. The open symbols are the experimental results; the dashed lines are the predictions of the step-function pressure model and the solid lines those of the thermal model.

major difference between this model and our data lies in the much faster collapse than in the experiment. This aspect cannot be changed by simply playing with the free parameters Δp, Δt and the initial velocity of the interface.

In order to get some insight into the failure of this model, we use the dynamic equation (2.1) in reverse to calculate p_V from the measured velocity and acceleration of the bubble interface. If we assume that the vapor is saturated, we can calculate the vapor temperature $T_S(t)$ from $p_V(t)$ by using the approximate relation

$$p_V = p_{V0} \exp\left[\frac{H_{Latent}}{R_v}\left(\frac{1}{T_0} - \frac{1}{T_S}\right)\right], \tag{2.2}$$

deduced from the Clausius-Clapeyron equation assuming a constant latent heat H_{Latent}; this approximation is legitimate over the limited temperature range of our experiment. In this equation R_v is the universal gas constant divided by the vapor mass; we take $p_{V0} = 10^5$ Pa and $T_0 = 100°$C.

For $D = 50$ μm with $E = 11.6$ μJ, the results of these calculations are shown with open diamonds in figures 2.7 (a) and (b). The pressure starts at around 8 atm, which leads to the huge acceleration of the liquid column. The insert in figure 2.7 (a) is the vapor pressure versus time on an enlarged vertical scale, which clearly shows that the pressure decreases with time continuously instead of reaching a constant value. The corresponding vapor temperature is shown by the open triangles in figure 2.7(b). The temperature starts at 170°C, and decreases continuously with time. A very sur-

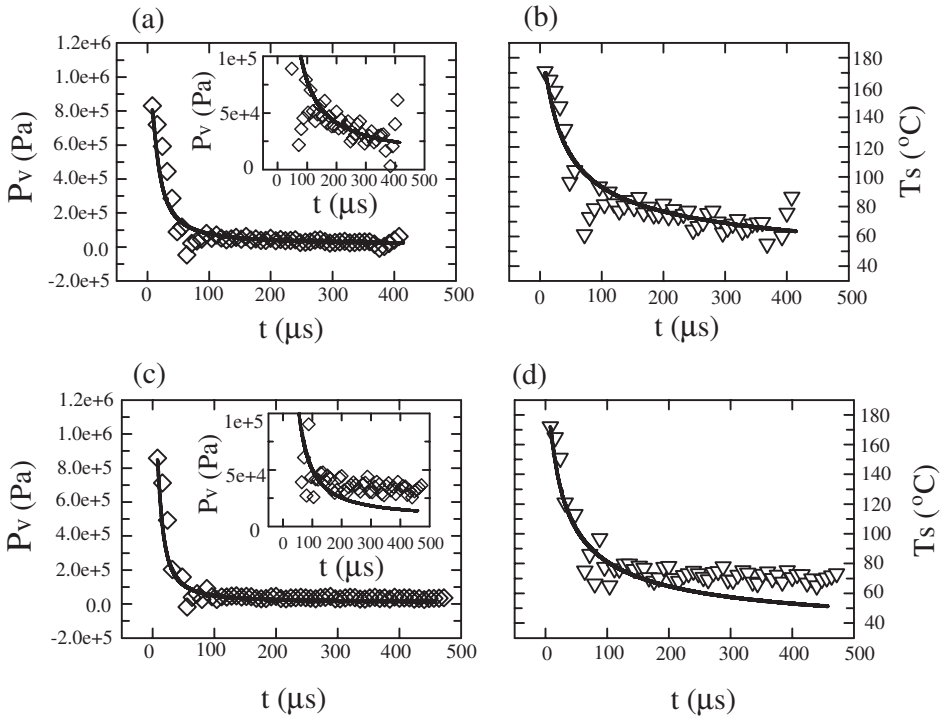

Figure 2.7: Vapor pressure and temperature vs. time for the larger tube with $E = 11.6\ \mu$J (a, b), and the smaller tube with $E = 5.3\ \mu$J (c, d). The open symbols are experimental results, the lines the thermal model predictions. The insert in (a) and (c) shows the vapor pressure vs. time on an enlarged vertical scale.

prising result is that at the finial stage the temperature is still $\sim 60°$C instead of the undisturbed liquid temperature $\sim 25°$C. The similar trends of the vapor pressure and temperature in the smaller tube with $E = 5.3\ \mu$J are shown by open symbols in figures 2.7 (c) and (d).

This analysis shows that the previous model fails because it replaces the actual slow pressure fall by an abrupt decrease.

2.4.2 The thermal model

It is interesting to explore to what extent these data can be reproduced by complementing the mechanical model of Eq. (2.1) with a thermal model. For this purpose

we write an energy balance for the vapor in the following form [see e.g. 73]:

$$H_{Latent}\frac{d}{dt}(\rho_V X) = k\frac{\partial T}{\partial x}\bigg|_{x=X} - \rho_V c_s X\frac{dT_S}{dt}. \tag{2.3}$$

The left-hand side of this equation is the latent heat associated with the vapor generation or condensation. The first term in the right-hand side, in which k is the thermal conductivity of the liquid, is the energy conducted to the vapor space from the liquid column. The last term, in which c_s is the specific heat along the saturation curve and $T_S(t) = T(X(t),t)$ is the temperature at the liquid surface, accounts for the energy necessary to maintain the vapor at saturation conditions; c_s is given by $c_s = c_{pV} - H_{Latent}/T_S$ in which c_{pV} is vapor specific heat [74].

In formulating the energy balance, Eq. (2.3), we have assumed that the vapor is in spatially uniform conditions and that it exchanges energy by conduction with the liquid column but not with the tube wall. We will return to this point later.

The temperature change of the liquid column is controlled by the advection-diffusion equation

$$\rho_L c_p\left[\frac{\partial T}{\partial t} + \mathbf{u}\cdot\nabla T\right] = k\nabla^2 T\,, \tag{2.4}$$

where c_p is the liquid specific heat. The thermal penetration length over the duration of the entire process is of the order of 5 μm, which is much less than the tube radius. Furthermore, the initial energy density may be expected to be reasonably uniform radially over the heated liquid volume and the transverse velocities are very small. For this reason, the only significant temperature gradient may be expected to be near the bubble surface so that the equation can be simplified to

$$\rho_L c_p\left[\frac{\partial T}{\partial t} + u\frac{\partial T}{\partial x}\right] = k\frac{\partial^2 T}{\partial x^2}. \tag{2.5}$$

We change the frame of reference to the moving interface by making the coordinate transformation $\xi = x - X(t)$; the final form of the equation is then

$$\rho_L c_p\frac{\partial T}{\partial t} = k\frac{\partial^2 T}{\partial \xi^2}. \tag{2.6}$$

This equation must be solved subject to the boundary conditions

$$T(\xi = 0,t) = T_S(t); \qquad T(\xi = \ell_L,t) = T_\infty. \tag{2.7}$$

In order to solve the liquid diffusion equation we also need to provide the initial temperature profile along the liquid column. This is a matter of considerable uncertainty because we do not have sufficient information on the spatial distribution of the absorbed laser energy. Furthermore, one-dimensional model cannot capture the detailed three-dimensional character of the initial temperature distribution. Very close to the instant of bubble nucleation, we can envisage a small vapor nucleus surrounded by a hot liquid layer which thins as the vapor expands. By the time the bubble has grown to occupy the cross section of the tube and the one-dimensional approximation becomes applicable, this layer will be adjacent to the bubble surface on the faces of the two liquid columns which bound it. On this basis, we postulate an initial temperature distribution given by

$$T(\xi) = T_\infty + (T_S(t_0) - T_\infty)\exp[-(\xi/2\delta)^2], \tag{2.8}$$

where $T_S(t_0)$ is the initial vapor temperature and δ is the thickness of the thermal layer surrounding the vapor space. This quantity maybe expected to be of the order of the laser beam width and we will use it as a fitting parameter.

We start the integration attributing to the bubble the measured length and velocity at the first instant t_0 at which the movie record shows an effectively one-dimensional bubble near the beginning of each experiment. For the larger tube with $E = 11.6$ μJ, we take the data recorded $t_0 = 8$ μs after the laser triggering: initial bubble size $X(t_0)$ = 10 μm, initial velocity $V(t_0) = 0.11$ m/s and initial vapor temperature $T_S(t_0) = 170°$C; the initial vapor pressure is calculated from initial vapor temperature according to Eq. (2.2) and is 8.07×10^5 Pa. Furthermore, ℓ_L is 13.5 mm, $p_\infty = 10^5$ Pa, $T_\infty = 25°$C. By choosing the parameter $\delta = 2.9$ μm we find the bubble-length-versus-time shown by the solid line in figure 2.6 (a). The time dependence of the bubble size agrees well with experimental data (open circles). The velocity and acceleration of the interface, shown by the solid lines in figure 2.4 (a), also agree well with experiment.

The vapor pressure and temperature versus time are shown by the solid lines in figure 2.7 (a) and (b). Both predictions are seen to be consistent with the experiment. In particular, the model captures well the continuous decrease of these quantities. It is remarkable also that the final bubble temperature, $\sim 60°$C, is reproduced by the model.

The actual heat exchange between the bubble and its surroundings is a complex problem for which too little information is available to permit the formulation of a faithful model. The thermal diffusion length over a time of 100 μs is about 4 μm, which is comparable with the thickness of the liquid film deposited on the tube wall, expected to be of the order of micrometers. This liquid layer is probably formed

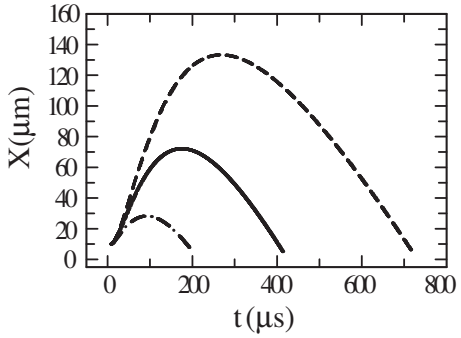

Figure 2.8: Calculated $X(t)$ curves for the thermal model with different values of the parameter δ for the larger tube with the same initial conditions as for $E = 11.6$ μJ; in descending order δ is 4.5, 2.9 and 1.5 μm. The middle line with δ = 2.9 μm is the best fit to the experimental data shown in figure 2.3 and 2.6.

from the liquid heated by the laser pulse and therefore will have some initial energy content. It is therefore not clear whether the tube wall, which should be cold as it will not have absorbed energy from the laser, plays a role in the thermal exchange. In view of all these uncertainties, the one-dimensional thermal model used before may perhaps best be seen as a phenomenological model which appears nevertheless able to capture at least a good part of the relevant physics. The importance of heat diffusion is brought into evidence by the sensitivity of the model to the value of the parameter δ. This point is illustrated in figure 2.8 which shows the bubble length vs. time as obtained with δ = 1.5, 2.9 and 4.5 μm.

The results of the model for the other cases of figure 2.3(a) are shown by the lines in the same figure. The initial conditions used in each case together with the corresponding value of δ for the larger tube with different energy levels are listed in table 2.1. At low laser energy it takes a few frames for the bubble to acquire a one-dimensional character and therefore t_0 is somewhat greater. The parameter δ does not change too much except for the lowest energy level. The solid lines in figure 2.3 (a) are the calculated bubble length versus time. A reasonably good agreement is apparent for each energy level. Only at the lower value of the energy does the model start to show some noticeable discrepancy with experiment, presumably because the one-dimensional approximation becomes invalid.

As a typical example for the smaller tube we consider the case with $E = 5.3$ μJ, again taking as the initial conditions the data: $t_0 = 8$ μs, initial velocity $V(t_0)$ = 0.94

Table 2.1: The initial conditions and the respective fitting parameter δ of the thermal model for different energy levels.

D (μm)	E (μJ)	$X(t_0)$ (μm)	$V(t_0)$ (m/s)	$T_S(t_0)(^\circ\mathrm{C})$	δ (μm)
50	11.6	10.0	0.11	170.0	2.9
	10.4	26.7	0.42	134.7	3.1
	8.2	21.0	0.11	135.7	3.6
	6.5	15.5	0.33	141.3	1.9
24.9	6.1	21.9	0.77	179.4	1.9
	5.3	22.5	0.94	172.0	1.8
	4.8	16.9	0.67	172.7	2.2
	3.8	15.7	0.77	163.2	2.1
	3.0	10.1	0.80	151.2	2.4

m/s, initial bubble size $X(t_0) = 22.5$ μm, initial vapor temperature $T_S(t_0) = 172.0^\circ$C and initial vapor pressure $p_V(t_0) = 8.48 \times 10^5$ Pa. Furthermore, ℓ_L is 12.5 mm with p_∞ and T_∞ as before. A reasonable fit to the data is obtained by taking $\delta = 1.8$ μm. The bubble length versus time calculated from the thermal model is shown by the solid line in figure 2.6 (b). The bubble size versus time again agrees very well with experiment (open squares). The velocity and acceleration of the interface are shown by the solid lines in figure 2.4 (b) and they are both seen to be consistent with experiment. The vapor pressure and temperature versus time in this case are shown by the solid lines in figure 2.7 (c) and (d). Although in this case the predictions are not in as good an agreement with experiment as for the larger tube, they are nevertheless consistence with observation. It is likely that a significant factor in the difference between model and data results in an inaccurate account of viscous effects which play a great role in the smaller tube.

The performance of the model for the other experiments in figure 2.3 (b) is shown by the solid lines in the same figure. The initial conditions and the respective values of δ are listed in table 2.1. The δ-values for different energy levels are quite close, ranging between 1.8 and 2.4 μm. The comparisons between the experiments (open symbols) and the results shows a very good agreement for all energy levels.

2.4.3 Energy partition

The present model contains both mechanical and thermal aspects and it is interesting to examine how the energy is apportioned among the different components. Let us consider the larger tube $D = 50$ μm with an absorbed energy $E = 11.6$ μJ. From

figure 2.4 the maximum velocity is 0.98 m/s; the corresponding kinetic energy is $2(\frac{1}{2}\rho_L S\ell_L \dot{X}^2) \simeq 0.025$ μJ, where $S = \pi D^2/4$ is the tube cross section and the factor of 2 accounts for both liquid columns. The instantaneous viscous energy dissipated is $2\mathscr{R}S\dot{X}^2\Delta t$, and $2\mathscr{R}S\dot{X}^2$ evaluated at the maximum velocity is 576 μJ/s. No matter what value of Δt is selected, this energy term is negligible. If we take Δt = 100 μs, $2\mathscr{R}S\dot{X}^2\Delta t$ = 0.058 μJ. Both these mechanical energies are much smaller than the laser energy absorbed by the liquid.

The total latent heat necessary to keep the bubble filled with saturated vapor at the point of its maximum volume is $2S\rho_V H_{latent} X_{max}$. At maximum expansion $T_S = 79\,^\circ$C, $\rho_V = 0.29$ kg/m^3, $X_{max} = 72$ μm so that $2S\rho_V H_{latent} X_{max}$ = 0.18 μJ, which is also much smaller than the 11.6 μJ absorbed by the liquid. Where is the remainder of the energy? The answer is that most of the laser energy has gone into heating up the liquid. The energy required to generate the temperature distribution Eq. (2.8) is

$$2\int_0^{\ell_L} (T_S(t_0) - T_\infty) \exp[-(\xi/2\delta)^2] c_p \rho S d\xi \,. \tag{2.9}$$

Evaluating this integral using δ = 2.9 μm, $T_S(t_0) = 170\,^\circ$C, we find $\sim$11.7 μJ, which is quite close to the laser energy input.

2.5 Conclusions

The dynamics of a laser-generated vapor bubble in microtubes with different diameters has been studied experimentally and theoretically. A pure inertia-driven model, neglecting thermal effects, failed to capture quantitatively the growth and collapse of the bubble. A new model was developed by considering heat transfer in addition to inertia and viscosity. This model has proved to be capable of reproducing the observed behavior of the bubble. It is concluded that thermal effects play an essential role during the whole process of growth and collapse.

3
Mathematical Formulation

3.1 Introduction

The governing equations that need to be solved in order to study the dynamics of vapor bubbles are stated in this chapter. The equations are the equations of motion for the fluid, namely the Navier-Stokes equations. When dealing with vapor bubbles the advection-diffusion equation for the temperature field must also be solved. Several assumptions are made in writing down the equations. First of all the liquid is taken to be incompressible. Since the velocities reached in the systems under consideration are much lower that the speed of sound in the liquid this is a valid approximation. Furthermore the physical properties of the liquid are taken to be constant in space and time. The momentum of the vapor/gas phase is assumed to be negligible due to the large difference in densities. The effect of the vapor/gas is thus to impose a surface pressure on the bubble. The pressure and temperature field inside the vapor/gas bubble is assumed to be spatially uniform. Finally we will use a cylindrical geometry and assume axial symmetry.

3.2 Governing Equations

In the following vapor quantities carry the subscript v, quantities evaluated at the phase interface carry the subscript s, while liquid quantities are not subscripted.

The equations governing the conservation of mass, momentum and energy are

$$\nabla \cdot \mathbf{u} = 0 \tag{3.1}$$

$$\frac{\partial \mathbf{u}}{\partial t} + \mathbf{u} \cdot \nabla \mathbf{u} = -\frac{1}{\rho}\nabla p + \frac{\mu}{\rho}\nabla^2 \mathbf{u} \tag{3.2}$$

$$\frac{\partial T}{\partial t} + \mathbf{u} \cdot \nabla T = \alpha \nabla^2 T\,, \tag{3.3}$$

with $\mathbf{u}$, p and T the liquid velocity, pressure, and temperature fields, ρ the liquid density, μ the liquid dynamic viscosity and α the liquid thermal diffusivity. The problems that will be investigated involve small temperature variations so that all the physical properties of the liquid as well as the surface tension can be considered constant. Temperature variations along the interface would be equilibrated on a smaller timescale than any other process in the systems under consideration by local evaporation and condensation. Furthermore, due to the very small vapor inertia, pressure gradients cannot persist beyond the acoustic timescale. The vapor phase is therefore modeled as a region with negligible mass and spatially uniform pressure.

At the interface the normal and tangential stresses must be balanced. The tangential stress on the interface vanishes due to neglecting the vapor viscous stress:

$$\mathbf{t} \cdot \mathbf{D}_s \cdot \mathbf{n} = 0\,, \tag{3.4}$$

where $\mathbf{D} = \mu\left(\nabla \mathbf{u} + \nabla \mathbf{u}^T\right)$ is the stress tensor, and $\mathbf{n}$ and $\mathbf{t}$ are the unit normal and tangent vectors at the interface respectively. The normal vector to the interface is defined to point into the liquid region. The normal stress balance results in

$$p_v = p_s + \sigma\kappa - \mathbf{n} \cdot \mathbf{D} \cdot \mathbf{n}\,, \tag{3.5}$$

where p_s is the pressure at the interface on the liquid side, p_v the vapor pressure, σ the surface tension and κ the local curvature of the interface.

We consider problems in which the rate of phase change is moderate and the vapor velocity is much smaller the the speed of sound so that we can assume thermodynamic equilibrium at the liquid/vapor interface. We therefore take p_v to be the saturation pressure at the interface temperature T_s. The Clausius-Clapeyron relates these two quantities as

$$\frac{dp_v}{dT_s} = \frac{L\rho_v}{T_s}\,, \tag{3.6}$$

with L the latent heat of evaporation and condensation and ρ_v the vapor density. The latent heat of phase change for water varies approximately by ten percent in the

temperature range of interest [75]. We can consider it to be constant as a first approximation, in view of the fact that also the temperature dependence of the physical fluid properties is neglected. Using the perfect gas law for the vapor and keeping L constant this equation can be integrated to find

$$p_v = p_{v,0} \exp\left(-\frac{L}{\mathscr{R}}\left[\frac{1}{T_0}-\frac{1}{T_s}\right]\right), \tag{3.7}$$

where $p_{v,0}$ and T_0 are reference values for the vapor pressure and temperature. T_s is the interface temperature and $\mathscr{R}$ the universal gas constant divided by the molecular mass of the vapor.

Conservation of energy at the interface can be expressed as

$$(\mathbf{q}_s - \mathbf{q}_v)\cdot\mathbf{n} = L\rho_v(\mathbf{u}_v - \mathbf{v})\cdot\mathbf{n} \equiv L\dot{m}, \tag{3.8}$$

where $\mathbf{u}_v$ is the vapor velocity at the interface, $\mathbf{v}$ the interface velocity, $\dot{m}$ the local mass flux due to phase change and $\mathbf{q} = -k\nabla T\cdot\mathbf{n}$ is the heat flux with k the thermal conductivity. At this point we assume the vapor volume is a closed and finite region in space. Integration over the closed surface of the phase interface S gives

$$L\oint \dot{m}\,dS = L\frac{d}{dt}(\rho_v V) = \oint (\mathbf{q}-\mathbf{q}_v)\cdot\mathbf{n}\,dS, \tag{3.9}$$

where V is the volume of the vapor region and, in the first step, we have assumed the vapor density to be spatially uniform. Using the estimate of the heat flux on the vapor side, derived in [73] and reproduced here in Appendix A for completeness, this equation can be written as

$$L\frac{d}{dt}(\rho_v V) + \rho_v V c_s \frac{dT_s}{dt} = \oint k(\nabla T\cdot\mathbf{n})\,dS, \tag{3.10}$$

with $c_s = c_{pv} - L/T_s$ the vapor specific heat along the saturation line, where c_{pv} is the (constant) specific heat at constant pressure for the vapor. The first term in the left hand side of Eq.(3.10) represents the latent heat of phase change, the second term represents the change of the vapor enthalpy and the right hand side represents the heat flux on the liquid side.

Conservation of mass at the interface is expressed by

$$\dot{m} = \rho_v(\mathbf{u}_v - \mathbf{v})\cdot\mathbf{n} = \rho(\mathbf{u}-\mathbf{v})\cdot\mathbf{n}, \tag{3.11}$$

from which

$$\mathbf{u}\cdot\mathbf{n} = \mathbf{v}\cdot\mathbf{n} + \frac{\rho_v}{\rho}(\mathbf{u}_v - \mathbf{v})\cdot\mathbf{n} \simeq \mathbf{v}\cdot\mathbf{n}, \tag{3.12}$$

in view of the smallness of ρ_v/ρ. Upon using this approximation, the equation of state for the vapor and the Clausius-Clapeyron relation Eq. (3.10) can be written as

$$\left(c_p + \frac{L^2}{\mathscr{R}T_s^2} - \frac{2L}{T_s}\right)\frac{dT_s}{dt} = \frac{1}{\rho_v V}\oint (k\nabla T\cdot\mathbf{n} - \rho_v L\mathbf{u}\cdot\mathbf{n})\,dS\,, \tag{3.13}$$

with c_p the liquid heat capacity at constant pressure. The term $\oint \mathbf{u}\cdot\mathbf{n}\,dS$ represents the rate of change of the vapor volume.

3.3 Level Set Method

In this work the level set method is used to represent the liquid/vapor interface. The level set method was introduced by Osher and Sethian in 1988 as a powerful and elegant way of computing the motion of interfaces [36]. The method is based on representing the interface by a smooth function $\phi(\mathbf{x})$, called the level set function. The vapor phase is the region where $\phi < 0$ and the liquid phase the region where $\phi > 0$. The interface is captured implicitly by the level set function as its zero level set, $\phi = 0$. To aid numerical treatment, ϕ typically is chosen to be a signed distance function, i.e a function that gives the shortest distance from a point $\mathbf{x}$ in the domain to the interface

$$d(\mathbf{x}) = \mathrm{S}(\phi(\mathbf{x}))\min(|\mathbf{x}-\mathbf{x}_\Gamma|) \quad \text{for all} \quad \mathbf{x}_\Gamma \in \Gamma\,, \tag{3.14}$$

where $\mathrm{S}(\phi)$ is the sign of the level set function defined as in Eq. (3.17), $\mathbf{x}$ a generic point in the domain and $\mathbf{x}_\Gamma$ a point on the interface. An illustration of a signed distance function is shown in figure 3.1. The figure shows the signed distance function for a circle (2D) with radius $R = 1$. The left part shows the actual level set function, ϕ. The right part shows several different level sets including the zero level set that represents the actual interface.

From this representation of the interface the normal vector to the interface and the curvature may be computed from

$$\mathbf{n} = \frac{\nabla\phi}{|\nabla\phi|} \quad \kappa = -\nabla\cdot\mathbf{n}\,.$$

The motion of the interface due to its advection by the liquid velocity field is governed by the level set advection equation

$$\frac{\partial\phi}{\partial t} + \mathbf{u}\cdot\nabla\phi = 0\,. \tag{3.15}$$

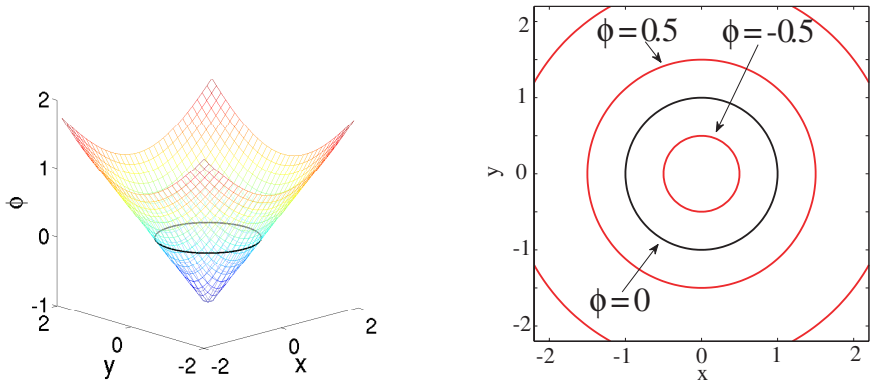

(a) level set function (b) level set contours

Figure 3.1: Example of a signed distance function for a circle in 2D with radius $R = 1$. The left part shows the level set function initialized as a signed distance function by means of $\phi(x,y) = \sqrt{x^2+y^2} - R$. The right part shows several level sets of ϕ. The black curve is the actual interface, represented by the level set $\phi = 0$. The other levels ($\phi = -0.5$ and $\phi = 0.5$ are concentric circles with radii $d+R$ where d is the distance to the interface

The numerical treatment of this equation is known to suffer from numerical diffusion, causing the interface to shrink in an unphysical manner. Additionally, when solving Eq. (3.15) the level set function may lose its signed distance character and develop large gradients near the interface, which is something to be avoided. Therefore, after solving Eq. (3.15), ϕ needs to be corrected so that it remains a signed distance function. This needs to be done without moving the interface. This procedure of maintaining the level set function as a signed distance function is called *reinitialization*. Several methods exist for reinitializing the level set function [37–39]. The approach used in this work was introduced in [38] and is based on solving the following PDE, called the reinitialization equation, to steady state

$$\begin{aligned} \frac{\partial \phi}{\partial \tau} + \mathrm{S}(\phi^0)\,(|\nabla \phi| - 1) &= 0 \\ \phi(x,0) &= \phi^0, \end{aligned} \tag{3.16}$$

where τ is an artificial time and ϕ^0 is the level set function that results from solving Eq. (3.15). The sign function is defined as

$$\mathrm{S}(\phi^0) = \begin{cases} 1 & \text{if } \phi^0 > 0 \\ 0 & \text{if } \phi^0 = 0 \\ -1 & \text{if } \phi^0 < 0. \end{cases} \tag{3.17}$$

In numerical computations the sign function is smeared out over a few grid cells to avoid numerical instabilities, but it must still satisfy $S(\phi^0) = 0$ for $\phi^0 = 0$.

Using the definition of the normal to the interface (Eq. (3.15) we can rewrite Eq. (3.16) as

$$\frac{\partial \phi}{\partial \tau} + \mathbf{w} \cdot \nabla \phi = S(\phi), \tag{3.18}$$

where $\mathbf{w} = S(\phi^0)\frac{\nabla \phi}{|\nabla \phi|} = S(\phi^0)\,\mathbf{n}$ and $\mathbf{n}$ is the unit normal to the interface. This equation, which is a scalar convection equation, shows that information is propagating from the interface outwards into the domain. Thus, when reinitializing the level set function by solving Eq. (3.16) the signed distance character is retrieved starting from the interface. As a consequence, Eq. (3.16) need not be solved to steady state, since the signed distance character is only required in a small region around the interface. Instead, a few iterations suffice, which is advantageous regarding computation times.

4
Numerical Method

4.1 Introduction

The numerical method used for the simulations described in this thesis is based on a finite difference discretization of the governing equations put forth in chapter 3. We solve the equations in cylindrical form and assume axial symmetry. The equations are discretized on a staggered grid, see figure 4.1, where scalars such as the pressure, temperature and level set function are defined at the cell centers (circles). The radial velocity components are defined at the vertical cell edges while the axial components are defined at the horizontal cell edges (arrows). The grids used in this work are uniform in both the radial and axial directions, i.e. $h = \Delta r = \Delta z$, with h the grid spacing. For the remainder of this work a cell center is denoted by the indices (i, j). The radial velocity component of a cell labeled with indices (i, j) is located at cell edge $(i+1/2, j)$ and the axial component at cell edge $(i, j+1/2)$.

The spatial discretization of the level set advection and reinitialization equations is done using high order methods of the (W)ENO type [36, 76–81]. Such methods are crucial for accurately solving the level set equations and for minimizing the mass loss that affects the level set method. The loss of mass is further decreased by means of a simple modification of the WENO method described in [40].

The Navier-Stokes equations for the liquid are solved using a projection method [82] that is first-order accurate in time and second-order in space. The pressure field

needs to be calculated subject to Dirichlet conditions at the liquid/vapor interface. The same holds for the energy equation. For this purpose we use the method developed in [83] for solving the Poisson equation with Dirichlet conditions imposed on an irregular boundary.

A straightforward spatial discretization of the momentum equations at grid points adjacent to the interface would involve irregular discretization stencils. Using such stencils is quite involved due to the (possibly) irregular shape of the interface. Also imposing the interface conditions is not a trivial matter. The use of irregular stencils can be avoided by extrapolating the liquid velocity into the vapor region using the known velocity field values in the liquid that lie close to the interface. As remarked in [44] and [84], the liquid velocity field should respect the divergence free condition also around the interface. Otherwise the interface is advected by a velocity field that is not mass conserving, leading to inaccurate interface transport. In [44] such an extrapolation method was developed for the Euler equations, i.e. for inviscid flow. We used the concept of this method and extended it to viscous flows by combining it with the ideas from [85] in order to impose the zero shear stress constraint (Eq. (3.4)) on the interface.

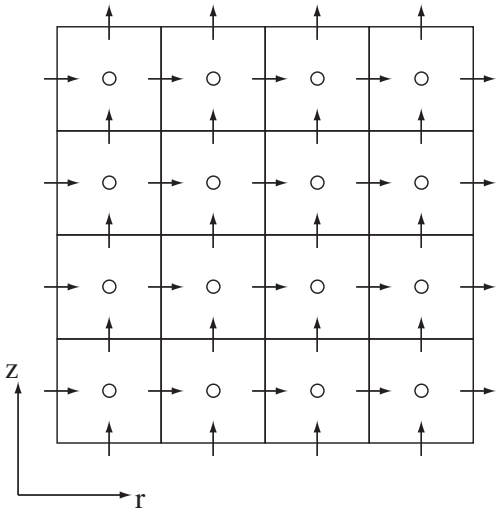

Figure 4.1: Section of the computational grid illustrating the staggered grid arrangement. $\circ$:p , $\rightarrow$: u_r , $\uparrow$: u_z. Cell centers are denoted with indices (i,j), vertical cell edges with (i+1/2,j) and horizontal cell edges with (i,j+1/2)

4.2 Level Set Equations

The accurate numerical treatment of the problems of interest in this work is a demanding task. Therefore, for clarity, we first explain a low-order procedure and describe later the actual choices made for the discretization of the equations.

4.2.1 Temporal discretization

Advection equation

The vapor/liquid interface is captured implicitly by the level set function ϕ and is advected by the liquid velocity field described by Eq. (3.15). Assuming we have a divergence free velocity field at time step n and $n-1$ we update the advection equation in time using an Adam-Bashforth scheme

$$\frac{\phi^{n+1}-\phi^n}{\Delta t} = -\frac{3}{2}(\mathbf{u}\cdot\nabla\phi)^n + \frac{1}{2}(\mathbf{u}\cdot\nabla\phi)^{n-1}. \tag{4.1}$$

Using linear interpolation we define the velocity at the cell centers as

$$\begin{aligned}(u_r)_{i,j} &= \frac{(u_r)_{i+1/2,j}+(u_r)_{i-1/2,j}}{2}\\ (u_z)_{i,j} &= \frac{(u_z)_{i,j+1/2}+(u_z)_{i,j-1/2}}{2}.\end{aligned} \tag{4.2}$$

Reinitialization equation

For the time integration of the reinitialization equation (Eq. (3.16)) we use a third order Runge-Kutta scheme that is put forth in [78]. The scheme can be written as a linear combination of Euler integration steps. If we write the spatial term as

$$L\phi^{(k)} = S(\phi^0)\left[|\nabla\phi^{(k)}|-1\right], \tag{4.3}$$

the time marching algorithm can be written as:

$$\phi^{(1)} = \phi^n - \Delta t L\phi^n, \tag{4.4}$$

$$\phi^{(2)} = \frac{3}{4}\phi^n + \frac{1}{4}\phi^{(1)} - \frac{1}{4}\Delta t L\phi^{(1)}, \tag{4.5}$$

$$\phi^{n+1} = \frac{1}{3}\phi^n + \frac{2}{3}\phi^{(2)} - \frac{2}{3}\Delta t L\phi^{(2)}. \tag{4.6}$$

4.2.2 Low-order spatial discretization

Advection equation

For the spatial discretization of the level set advection equation we need to compute the spatial derivatives of ϕ. These derivatives may be approximated by central differences which are second order accurate. However, it is well known that central discretization can produce oscillations in the solution because central differencing does not reflect the direction of transport. Therefore one should use information that comes from the upstream direction. Thus we first calculate left- and right-sided derivatives, and then choose one of them by examining the direction of the flow. First-order accurate approximations for these derivatives in the radial direction are

$$\left(\frac{\partial\phi}{\partial r}\right)^{-} = \frac{\phi_{i,j}-\phi_{i-1,j}}{\Delta r}, \quad \left(\frac{\partial\phi}{\partial r}\right)^{+} = \frac{\phi_{i+1,j}-\phi_{i,j}}{\Delta r}. \tag{4.7}$$

The upwinding can be written as

$$\frac{\partial\phi}{\partial r} = \begin{cases} \left(\frac{\partial\phi}{\partial r}\right)^{+} & \text{if } u_r \le 0 \\ \left(\frac{\partial\phi}{\partial r}\right)^{-} & \text{if } u_r > 0\,. \end{cases} \tag{4.8}$$

The axial direction would be treated similarly. As shown below, this first-order discretization is not sufficiently accurate. A better approximation will be described later.

Reinitialization equation

The spatial part of the reinitialization equation can be written in terms of the operator $L\phi$ defined in (4.3). The sign function $S(\phi^0)$ is smeared over a few grid cells for numerical stability and is defined as

$$S(\phi^0) = \frac{\phi^0}{\sqrt{(\phi^0)^2+\Delta r^2}}, \tag{4.9}$$

For grid cell (i,j) Eq. (4.3) is then discretized as

$$(L\phi_{i,j}) = \begin{cases} \mathrm{S}(\phi^0_{i,j})\left(\sqrt{\max(a_+^2,b_-^2)+\max(c_+^2,d_-^2)}-1\right) & \text{if } \phi^0_{i,j} > 0 \\ \mathrm{S}(\phi^0_{i,j})\left(\sqrt{\max(a_-^2,b_+^2)+\max(c_-^2,d_+^2)}-1\right) & \text{if } \phi^0_{i,j} \le 0\,, \end{cases} \tag{4.10}$$

with

$$\begin{aligned} a &= (\phi_{i,j}-\phi_{i-1,j})/\Delta r \quad b = (\phi_{i+1,j}-\phi_{i,j})/\Delta r \\ c &= (\phi_{i,j}-\phi_{i,j-1})/\Delta z \quad d = (\phi_{i,j+1}-\phi_{i,j})/\Delta z\,, \end{aligned}$$

and $a_+ = \max(a,0)$ and $a_- = \min(a,0)$ and similarly for $b_\pm$. A clear discussion about Eq. (4.10) can be found in [86].

The spatial derivatives used in these expressions for the discretization of the level set equations are first-order accurate. Using these low-order approximations results in a loss of mass due to their diffusive nature. To illustrate this consider the following example. We initialize ϕ^0 as a signed distance function for a circle with radius $R = 1$ in a 2D domain $[-2,2] \times [-2,2]$

$$\phi^0(x,y) = \sqrt{x^2+y^2} - 1\,. \tag{4.11}$$

As ϕ^0 already is a signed distance function, applying the reinitialization algorithm to it should not move the interface. Figure 4.3(a) shows the result of this experiment, where the spatial derivatives were approximated with the first order expressions. The figure shows zero level sets of ϕ for various iteration steps of the reinitialization equation. Clearly mass (or area) is not conserved by using these low order approximations. Furthermore, the mass loss increases with the number of iterations. Thus, in actual computations, where typically many iterations of the reinitialization equation are performed, this clearly is a matter of great concern. As the mass loss effect is stronger when the interface is not resolved adequately, we deliberately used a very coarse grid of $\Delta r = 0.2$ and time step $\Delta\tau = 0.5\Delta r$ for illustration purposes. For this reason the initial interface ($N = 0$) already does not look very smooth.

The mass loss effect can be decreased by increasing the grid resolution, but this is not always a practical option in actual computations. A better way of reducing the error is to use higher-order methods for approximating the spatial derivatives. These methods will be discussed next.

4.2.3 Higher order schemes for the spatial derivatives

The approximation of the spatial derivatives can be improved upon by using the ideas introduced first in [76] of Essentially Non-Oscillatory schemes. Originally these schemes were developed for the integration of systems of conservation laws. In [78] and [79] the numerical implementation of these schemes was simplified and later Osher and Sethian extended the ideas to equations of the type used in the level set formulation in [36]. We will briefly discuss these schemes. For a more detailed discussion see the above references.

Essentially Non-Oscillatory (ENO) scheme

The idea of the higher order schemes is to find the smoothest possible polynomial interpolation to a discretized function f. This polynomial is then differentiated and

evaluated at the location where the spatial derivative is required. The key feature is that the discretization stencil is not fixed but adaptive instead. Nodes are added to the stencil in the direction where the data varies the least. In this way one avoids interpolation in the regions where the function undergoes large variations or potential discontinuities, which would render the interpolation inaccurate.

Newton's divided difference interpolation is used for the construction of the approximating polynomials. In this formulation the polynomial for $f(r)$ is written as

$$\begin{aligned} f(r) &= D^0 f + D^1 f(r-r_i) + D^2 f(r-r_i)(r-r_{i+1}) + \\ &\quad + D^3 f(r-r_i)(r-r_{i+1})(r-r_{i+2})\,. \end{aligned} \tag{4.12}$$

The coefficients are the divided differences which are defined as
zeroth divided differences

$$D_i^0 f = f_i\,, \tag{4.13}$$

first divided differences

$$D_{i+1/2}^1 f = \frac{D_{i+1}^0 f - D_i^0 f}{\Delta r} = \frac{f_{i+1}-f_i}{\Delta r}\,, \tag{4.14}$$

second divided differences

$$D_i^2 f = \frac{D_{i+1/2}^1 f - D_{i-1/2}^1 f}{2\Delta r} = \frac{f_{i+1}-2f_i+f_{i-1}}{2\Delta r^2}\,, \tag{4.15}$$

third divided differences

$$D_{i+1/2}^3 f = \frac{D_{i+1}^2 f - D_i^2 f}{3\Delta r} = \frac{f_{i+2}-3f_{i+1}+3f_i-f_{i-1}}{6\Delta r^3}\,. \tag{4.16}$$

Upon differentiating Eq. (4.12) with respect to r one gets

$$\begin{aligned} f'(r) &= D^1 f + D^2 f\left[(r-r_i)+(r-r_{i+1})\right] + D^3 f\left[(r-r_{i+1})(r-r_{i+2})\right. \\ &\quad \left. + (r-r_i)(r-r_{i+2}) + (r-r_i)(r-r_{i+1})\right]\,, \end{aligned} \tag{4.17}$$

where it is noted that the constant term has vanished.

The original form of the Newton divided difference interpolation adds nodes in only one direction, i.e. the stencil that is used for the construction of the polynomial is fixed. In the ENO scheme however one chooses to add the node in the direction where the data varies the least. The nodes that make up the stencil are therefore not a priori known, but selected one at a time. As the divided differences are a measure of the variation in the data, the choice of adding a particular node to the stencil is made

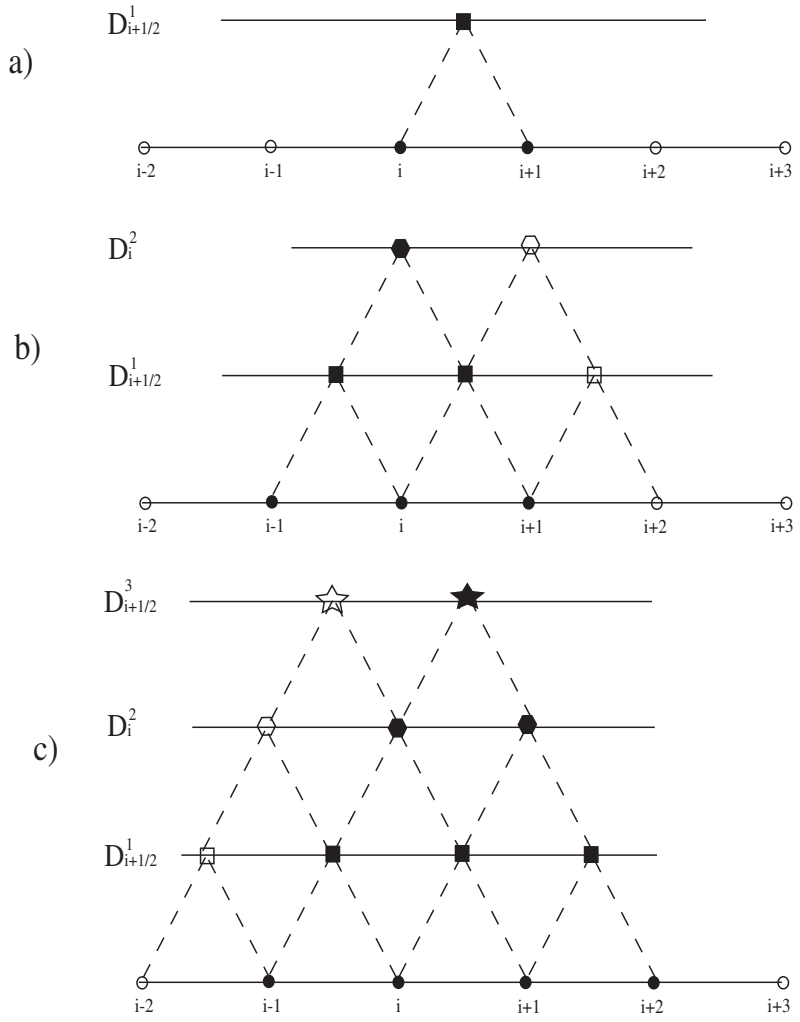

Figure 4.2: Selecting the nodes that are used for constructing the approximating polynomial for the right sided first-order derivative of a function f. Nodes are added to the stencil one at a time. (a) The first order contribution to the polynomial involves nodes i and i+1. (b) For the second order contribution, two second divided differences are computed. The one with the smallest absolute magnitude is chosen. The node that is used for this second divided difference is added to the stencil. Here we suppose node i-1 is selected. (c) For the third order contribution, the procedure is similar, with the exception that the third divided differences are used.

by comparing the magnitude of the divided differences and choosing the one that is smallest, reflecting the smallest variation. To illustrate consider figure 4.2. A possible route for constructing the stencil used for computing the right sided derivative of f is shown. For determining the right sided derivative at node i, $(f_r^+)_i$, we define $k = i$. The first term is simply taken as

$$\left(D^1_{k+1/2} f\right), \tag{4.18}$$

which is the first order approximation that we had before. The nodes used for the first order approximation are shown in part (a) of figure 4.2. To get the quadratic and cubic contributions nodes are now added to the stencil. Since up to this point the nodes with index i and $i+1$ have been used, there are two possibilities of adding a node, namely the one on the right $i+2$ and the one on the left $i-1$, see part (b) of figure 4.2. The strategy, as was said above, is to add the node that results in the least variation of the data. This is done by comparing the second divided differences at nodes k and $k+1$. If $|D^2_k f| \leq |D^2_{k+1} f|$ we set $c = D^2_k f$ and $k^\star = k-1$. Otherwise we set $c = D^2_{k+1} f$ and $k^\star = k$. The second term of Eq. (4.17) is then defined as

$$c\left[(r_i - r_k) + (r_i - r_{k+1})\right], \tag{4.19}$$

which, using $r_i - r_k = (i-k)\Delta r$ and $r_i - r_{k+1} = (i-(k+1))\Delta r$, can be written as

$$c(2(i-k)-1)\Delta r. \tag{4.20}$$

The $k^\star$ is defined so that the correct nodes are selected for computing the third term. Suppose the node on the left (f_{i-1}) is added to the stencil, as shown in part (b) of figure 4.2. We continue the procedure in order to determine the cubic contribution. Again there are two possibilities for adding a node. As the stencil so far is composed of nodes i, $i+1$ and $i-1$ either the node on the left $i-2$, or one on the right $i+2$ will be added. The choice is made once more by comparing the variations in the data and the node giving the smoothest divided difference is chosen. For the third term, the third divided differences are compared. Thus, if $|D^3_{k^\star+1/2} f| \leq |D^3_{k^\star+3/2} f|$ we set $c^\star = D^3_{k^\star+1/2} f$, otherwise $c^\star = D^3_{k^\star+3/2} f$. The third term of Eq. (4.17) is

$$c^\star\left[(r_i - r_{k^\star+1})(r_i - r_{k^\star+2}) + (r_i - r_{k^\star})(r_i - r_{k^\star+2}) + (r_i - r_{k^\star})(r_i - r_{k^\star+1})\right], \tag{4.21}$$

which, using expressions of the form $r_i - r^\star_k = (i-k^\star)\Delta r$, can be written as

$$c^\star(3(i-k^\star)^2 - 6(i-k^\star) + 2)\Delta r^2. \tag{4.22}$$

This completes the approximation of the right sided derivative. Approximating the left sided derivative, $(f_r^-)_i$, follows exactly the same procedure, except that one starts with $k = i-1$.

Weighted Essentially Non-Oscillatory (WENO) method

The algorithm explained in the previous section results in three possible stencils for the approximation of the first derivative. In the neighborhood of large variations or discontinuities in the data choosing the stencil that is smoothest is a good approach. On the other hand in regions where the data is smooth, all three candidate stencils contain valuable information and can be combined to obtain a higher-order approximation to the derivative. The Weighted Essentially Non-Oscillatory (WENO) method does exactly this. Instead of choosing the smoothest stencil, the WENO method assigns weight factors, based on some measure of smoothness, to the candidate stencils and expresses the derivative as a convex combination of them. The weights are defined such that in smooth regions high accuracy is obtained by using all three candidates while in regions near discontinuities very small weights are assigned to the stencils that contain the discontinuity, thus essentially reducing to the ENO scheme. We will briefly go through the algorithm of computing a one sided derivative with the WENO method. For a more in depth treatment see [80].

Consider the computation of the left sided derivative of some quantity f in the radial direction, $(f_r^-)_i$, at grid node i. The three possible ENO approximations for the left sided derivative use the the data at nodes $\{f_{i-3},\, f_{i-2},\, f_{i-1},\, f_i,\, f_{i+1},\, f_{i+2}\}$. Defining the first divided differences as

$$v_1 = \frac{f_{i-2} - f_{i-3}}{\Delta r}, \quad v_2 = \frac{f_{i-1} - f_{i-2}}{\Delta r}, \quad v_3 = \frac{f_i - f_{i-1}}{\Delta r},$$
$$v_4 = \frac{f_{i+1} - f_i}{\Delta r}, \quad v_5 = \frac{f_{i+2} - f_{i+1}}{\Delta r}, \tag{4.23}$$

the three candidate ENO approximations to the first derivative can be written as

$$f_r^{(1)} = \frac{v_1}{3} - \frac{7v_2}{6} + \frac{11v_3}{6}, \quad f_r^{(2)} = -\frac{v_2}{6} + \frac{5v_3}{6} + \frac{v_4}{3},$$
$$f_r^{(3)} = \frac{v_3}{3} + \frac{5v_4}{6} - \frac{v_5}{6}. \tag{4.24}$$

The WENO approximation to $(f_r^-)_i$ is a convex combination of these candidates:

$$f_r = \sum_{k=1}^{3} w_k f_r^{(k)}, \tag{4.25}$$

with w_k the weight factors satisfying $0 \le w_k \le 1$ and $\sum_{k=1}^{3} w_j = 1$ for consistency and stability. In smooth regions, the weights can be chosen in such a way as to achieve a fifth-order approximation to the first derivative. Such optimal weights, denoted by

C_k, are $C_1 = 0.1$, $C_2 = 0.6$ and $C_3 = 0.3$. In non-smooth regions however the weight assigned to the candidate with the smoothest stencil should be close to unity while the others are assigned very low weights, thus reducing to the ENO scheme. In order to switch between these two limits the weights must be computed adaptively. For this purpose, it is pointed out in [81] that the optimal fifth order accurate approximation is still obtained in smooth regions when setting

$$w_k = C_k + \mathcal{O}(\Delta r^2)\,. \tag{4.26}$$

Weights are then defined by

$$w_k = \frac{a_k}{\sum_{k=1}^{3} a_k}\,, \quad a_k = \frac{C_k}{(S_k+\varepsilon)^2}\,. \tag{4.27}$$

It is observed that the sum of the weights add to 1 as required. In order to avoid division by zero a small number, ε, is introduced, typically taken in the range 10^{-5} to 10^{-7}. S_j are indicators of the smoothness for the three stencils. In [81] a measure of the smoothness is introduced that satisfies (4.26), so that optimal accuracy is obtained in smooth regions. The smoothness of a stencil is estimated by the sum of the L_2 norms of all the derivatives of the interpolating polynomial on that stencil integrated over a grid cell:

$$S_k = \sum_{l=1}^{2} \int_{r_{i-1/2}}^{r_{i+i/2}} \Delta r^{2l-1} \left(\frac{d^l f^{(k)}}{dr^l} \right)^2 dr\,, \tag{4.28}$$

where the Δr^{2l-1} is incorporated to remove grid dependent factors. Writing out Eq. (4.28) for the three candidate stencils gives

$$\begin{aligned}
S_1 &= \frac{13}{12}(v_1 - 2v_2 + v_3)^2 + \frac{1}{4}(v_1 - 4v_2 + 3v_3)^2\,,\\
S_2 &= \frac{13}{12}(v_2 - 2v_3 + v_4)^2 + \frac{1}{4}(v_2 - v_4)^2\,,\\
S_3 &= \frac{13}{12}(v_3 - 2v_4 + v_5)^2 + \frac{1}{4}(3v_3 - 4v_4 + v_5)^2\,.
\end{aligned} \tag{4.29}$$

In smooth regions the S_k will all be small resulting in weights that will be close to the optimal weights, thereby achieving maximum accuracy. On the other hand, if the data are not smooth on one of the candidate stencils the smoothness indicator for that stencil will be large resulting in a very small weight. In effect, that stencil is given limited influence and thus the ENO properties are recovered.

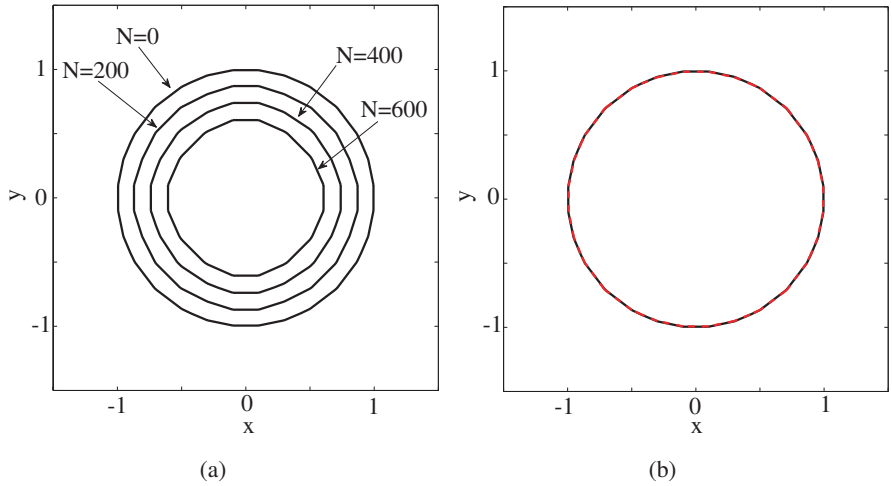

Figure 4.3: Performing 600 iterations of the reinitialization equation, Eq. (3.16) with the initial condition already a signed distance function, given by Eq. (4.11). (a) Using the first order approximations (Eq. (4.7)) to the spatial derivatives of the level set function. (b) Using the high order accurate WENO scheme for the approximation of the spatial derivatives.

The approximation of the right sided derivative follows the same procedure except that the data $\{f_{i-2}, f_{i-1}, f_i, f_{i+1}, f_{i+2}, f_{i+3}\}$ are used and the first divided difference table is

$$v_1 = \frac{f_{i+3} - f_{i+2}}{\Delta r} \quad v_2 = \frac{f_{i+2} - f_{i+1}}{\Delta r} \quad v_3 = \frac{f_{i+1} - f_i}{\Delta r}$$
$$v_4 = \frac{f_i - f_{i-1}}{\Delta r} \quad v_5 = \frac{f_{i-1} - f_{i-2}}{\Delta r}. \tag{4.30}$$

To illustrate the improvement of the WENO method over the simple first order scheme, consider again the level set function initialized as a signed distance function by means of Eq. (4.11). Figure 4.3(b) shows the results after 600 iterations of the reinitialization equation using the same grid and time step, but now with the WENO scheme for the gradient approximation. The black curve is the zero level set of the initial signed distance function ϕ^0. The red dashed curve is the result of the WENO method after 600 iterations. Despite the clear improvement of the WENO scheme over the first order scheme, there still is a loss of mass albeit at a much lower rate (see figure 4.5(a) where 6000 iterations are performed using the WENO scheme). Much of the work concerning the level set method has been focussed on ever decreasing the mass loss. Various methods have been proposed, such as a hybrid particle level set

method [41] where the authors seed particles around the interface and advect them in a Lagrangian fashion by the flow. These particles are used to detect any mass loss and correct the level set when this happens. Sussman and Fatemi [42] proposed a modification of the reinitialization equation by imposing the constraint that the total area must be preserved. Russo and Smereka in [40] proposed a very elegant and simple modification of the approximation of the gradients that virtually removes the mass loss when solving the reinitialization equation. We have implemented this method, termed the "subcell fix", and will discuss it next.

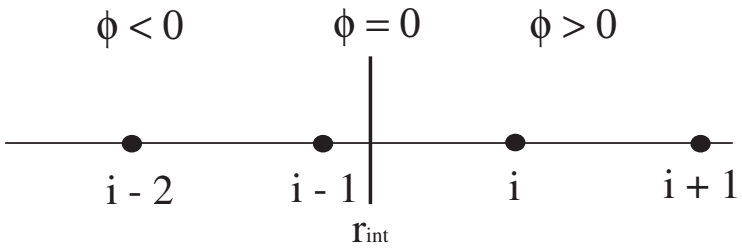

Figure 4.4: Illustration of the nodes used in approximating the spatial derivative of the level set function for a node adjacent to the interface. Information from across the interface is used in this approximation, which violates the flow of information.

4.2.4 "Subcell fix"

Although the WENO scheme is supposed to be fifth order accurate, when used in the reinitialization equation the accuracy has been shown to be of second order [87]. The reason for this low accuracy was found by Russo and Smereka in [40]. Recall that the reinitialization equation is a hyperbolic equation where the characteristics propagate outwards from the interface in the normal direction (Eq. (3.18)). For solving this equation upwind methods are used to respect the direction of propagation of information. Near the interface however the discretization of the derivatives is not truly upwind because information from across the interface is used. This is illustrated in figure 4.4. Let us consider for simplicity a 1D situation and assume that the derivatives are computed with the first-order scheme. Suppose we wish to update ϕ_i. Then we need to compute the left and right sided derivatives

$$a = \frac{\phi_i - \phi_{i-1}}{\Delta r}, \qquad b = \frac{\phi_{i+1} - \phi_i}{\Delta r}. \tag{4.31}$$

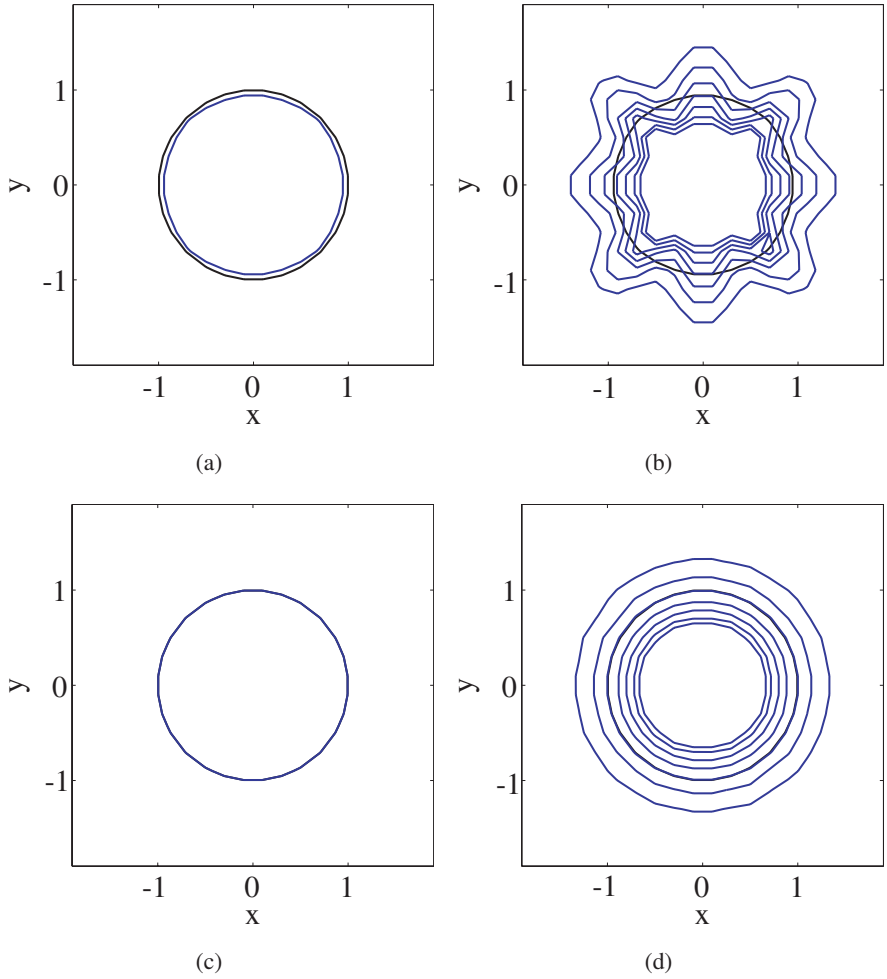

Figure 4.5: Performing 6000 iterations of the reinitialization equation with the initial condition already a signed distance function ,given by Eq. (4.11). (a) Initial (black) and final (blue) zero level set using WENO scheme. Mass loss is small but still noticeable after many iterations. (b) Several isocontours of the curvature field computed after completing 6000 iteration using the WENO scheme. The reinitialized level set function becomes noisy and oscillations develop. (c) Initial (black) and final (blue) zero level set using the ”subcell fix”. The mass loss is practically zero. (d) Several isocontours of the curvature field after reinitialization using the ”subcell fix”. The curvature remains smooth, facilitating the implementation of surface tension effects.

As $\phi_i > 0$ (see the figure) if both $a > 0$ and $b > 0$, the left sided derivative, a, is going to be selected for updating ϕ_i according to equation (4.10). Therefore, the value of the level set function ϕ_i^{n+1} will come to depend on the value ϕ_{i-1}^n which is on the other side of the interface. This situation violates the fact that information should propagate from the interface outward. As a consequence of this violation the zero level set will move slightly during reinitialization which results in loss of mass and noise in the level set function. Consequently also the curvature computation, which requires the computation of second order derivatives of ϕ, becomes noisy. The solution put forth by Russo and Smereka is a simple modification of the derivative approximation so that the flow along characteristics is respected. For the case discussed, the left sided derivative is approximated using the fact that $\phi = 0$ on the interface. Then one can write

$$a = \frac{\phi_i}{r_i - r_{\text{int}}}, \tag{4.32}$$

where the location of the interface, r_{int} is determined from a third order interpolation of ϕ. This idea can be extended to the ENO method, which was done in [88] where a fourth order accurate scheme was obtained. The one-sided derivatives are computed with the WENO method as explained above for nodes that do not lie immediately next to the interface. For nodes that do lie next to the interface, a third order ENO scheme is applied, where the location of the interface (calculated using a cubic interpolation of the initial level set function) is taken into account. Thus the interface becomes part of the stencil and consequently the stencil is non-uniform which has to be taken into account. This method is implemented in this work also. The superior performance of this "subcell fix" is illustrated in figure 4.5 where again the level set function is initialized by means of Eq. (4.11). In order to show the significant mass loss due to using the WENO method, this time 6000 iterations of the reinitialization are performed. The computation is performed on a very coarse grid for illustration purposes. Figures 4.5(a) and 4.5(c) show the initial and final zero level set curves for the WENO method and the "subcell fix" method respectively. The simple modification of the subcell method has decreased the mass loss effect dramatically. The level sets in the case of the "subcell" fix cannot even be distinguished from each other. Another improved feature is the amount of noise in the level set function after reinitialization. This can be seen clearly from the isocontours of the curvature field. The curvature iscontours for a circle should be concentric circles. After many iterations using the WENO method however the curvature isocontours develop oscillations, shown in figure 4.5(b). This would be disastrous for the implementation of surface tension effects. The subcell fix method however remains practically free of noise even after many iterations. The curvature isocontours remain smooth concentric circles, shown in figure 4.5(d).

4.3 Momentum Equations

4.3.1 Projection method

The equations of motion for the fluid (eqns 3.1 and 3.2) are integrated in time using a projection method [82]. The convective and viscous terms are treated in an explicit fashion and the time integration is carried out with a first order Euler method. In the projection method an intermediate velocity field, $\mathbf{u}^\star$ is introduced such that $\mathbf{u}^{n+1} - \mathbf{u}^n = \mathbf{u}^{n+1} - \mathbf{u}^\star + \mathbf{u}^\star - \mathbf{u}^n$. In this way the momentum equations are split in two parts and their solution is found in two steps. The first one is a predictor step where the intermediate velocity field is found by ignoring the pressure gradient term:

$$\frac{\mathbf{u}^\star - \mathbf{u}^n}{\Delta t} = -(\mathbf{u}\cdot\nabla\mathbf{u})^n + \frac{1}{\rho}(\nabla\cdot\mathbf{D})^n \,. \tag{4.33}$$

In the second step, the projection, the pressure gradient is added to find the velocity field at the new time step:

$$\frac{\mathbf{u}^{n+1} - \mathbf{u}^\star}{\Delta t} = -\frac{\nabla p^{n+1}}{\rho} \,. \tag{4.34}$$

An equation for the pressure field is arrived at by applying the divergence operator on both sides of the equation, and requiring that $\nabla\cdot\mathbf{u}^{n+1} = 0$:

$$\frac{1}{\rho}\nabla^2 p^{n+1} = \frac{\nabla\cdot\mathbf{u}^\star}{\Delta t} \,, \tag{4.35}$$

where the density is taken out because it is constant throughout the liquid.

Thus, to summarize, the projection method consists of

- computing an intermediate velocity field by integrating the momentum equation ignoring the pressure gradient contribution.
- solving Eq. (4.35) to find the pressure field.
- correcting the intermediate velocity field using the pressure gradients.

4.3.2 Time step

Due to the explicit treatment of the convective and viscous terms the integration method is stable only if all relevant velocity scales are resolved. Each physical process in the momentum equations involves its own time scale. The convection time scale is the time it takes to advect the fluid across one grid cell:

$$T_{conv} = \frac{\Delta r}{|u_r|_{\max}} + \frac{\Delta z}{|u_z|_{\max}} \,. \tag{4.36}$$

The time scale for the viscous term is the diffusion time over one grid cell:

$$T_{visc} = \frac{\rho}{\mu}\left(\frac{\Delta r^2}{2} + \frac{\Delta z^2}{2}\right). \tag{4.37}$$

The last physical process to resolve is surface tension. The time scale set by surface tension is the time it takes the fastest capillary wave to travel a distance of one grid cell [89]

$$T_{surf} = \left(\frac{\rho \Delta r^2}{\sigma \kappa}\right), \tag{4.38}$$

where κ is the local curvature. In order to resolve all time scales the time step is chosen as

$$\Delta t = \frac{\varepsilon}{T_{conv} + T_{visc} + T_{surf}}, \tag{4.39}$$

with $\varepsilon < 1$.

In the following sections we will discuss the spatial discretization in more detail.

4.3.3 Navier-Stokes

Assuming axial symmetry, the Navier-Stokes equations in cylindrical coordinates are

$$\frac{\partial u_r}{\partial t} + u_r\frac{\partial u_r}{\partial r} + u_z\frac{\partial u_r}{\partial z} = \frac{\mu}{\rho}\left[\frac{1}{r}\frac{\partial}{\partial r}\left(r\frac{\partial u_r}{\partial r}\right) + \frac{\partial^2 u_r}{\partial r^2} - \frac{u_r}{r^2}\right] - \frac{1}{\rho}\frac{\partial p}{\partial r}, \tag{4.40a}$$

$$\frac{\partial u_z}{\partial t} + u_r\frac{\partial u_z}{\partial r} + u_z\frac{\partial u_z}{\partial z} = \frac{\mu}{\rho}\left[\frac{1}{r}\frac{\partial}{\partial r}\left(r\frac{\partial u_z}{\partial r}\right) + \frac{\partial^2 u_z}{\partial z^2}\right] - \frac{1}{\rho}\frac{\partial p}{\partial z}. \tag{4.40b}$$

The difficulty with Eqs. (4.40a) and (4.40b) are the terms containing $1/r$. These terms result in a singularity at the axis of symmetry, where $r = 0$. In order to resolve this problem the following transformation is made [90]

$$q_r = r u_r. \tag{4.41}$$

The fact that $q_r = 0$ on the axis of symmetry alleviates the singularity. Using this transformation together with the following expressions derived from them

$$\frac{\partial u_r}{\partial r} = \frac{1}{r}\frac{\partial q_r}{\partial r} - \frac{q_r}{r^2}, \quad \frac{\partial u_r}{\partial z} = \frac{1}{r}\frac{\partial q_r}{\partial z},$$

$$\frac{\partial^2 u_r}{\partial z^2} = \frac{1}{r}\frac{\partial^2 q_r}{\partial z^2}, \quad \frac{\partial u_r}{\partial t} = \frac{1}{r}\frac{\partial q_r}{\partial t},$$

one may re-write the momentum equations in terms of these new variables as

$$\frac{\partial q_r}{\partial t}+\frac{q_r}{r}\frac{\partial q_r}{\partial r}-\frac{q_r^2}{r^2}+u_z\frac{\partial q_r}{\partial z}=\frac{\mu}{\rho}\left[r\frac{\partial}{\partial r}\left(\frac{1}{r}\frac{\partial q_r}{\partial r}\right)+\frac{\partial^2 q_r}{\partial z^2}\right]-\frac{r}{\rho}\frac{\partial p}{\partial r}, \tag{4.42a}$$

$$\frac{\partial u_z}{\partial t}+\frac{q_r}{r}\frac{\partial u_z}{\partial r}+u_z\frac{\partial u_z}{\partial z}=\frac{\mu}{\rho}\left[\frac{1}{r}\frac{\partial}{\partial r}\left(r\frac{\partial u_z}{\partial r}\right)+\frac{\partial^2 u_z}{\partial z^2}\right]-\frac{\partial p}{\partial z}. \tag{4.42b}$$

The continuity equation after the transformation becomes

$$\frac{1}{r}\frac{\partial q_r}{\partial r}+\frac{\partial u_z}{\partial z}=0. \tag{4.43}$$

4.3.4 Spatial discretization

Convective and viscous terms

Consider a generic grid cell with indices (i,j). The convection term for the radial velocity component is defined at the right vertical cell edge, $(i+1/2,j)$

$$\left(\frac{q_r}{r}\frac{\partial q_r}{\partial r}-\frac{q_r^2}{r^2}+u_z\frac{\partial q_r}{\partial z}\right)_{i+1/2,j}. \tag{4.44}$$

We have already seen that first-order accurate expressions for the gradients are diffusive. The velocity gradients are therefore computed with the ENO scheme explained in section 4.2.3. For the term $u_z\dfrac{\partial q_r}{\partial z}$ the axial velocity component, u_z must be defined at the right vertical cell edge. This is done by averaging

$$u^z_{i+1/2,j}=\frac{1}{4}\left[u^z_{i,j+1/2}+u^z_{i+1,j+1/2}+u^z_{i,j-1/2}+u^z_{i+1,j-1/2}\right]. \tag{4.45}$$

where we used a superscript to indicate the velocity component in order to avoid too many subscripts on each term. We do this throughout this work in case there can be no confusion about the meaning. The second term in Eq. (4.44), which does not contain any derivative, is simply evaluated at the right vertical cell edge. The convective term for the axial velocity component is treated similarly.

The viscous terms are discretized using standard second order central differencing. Thus the two terms of the viscous part in the momentum equation for q_r become

$$\begin{aligned} r\frac{\partial}{\partial r}\left(\frac{1}{r}\frac{\partial q_r}{\partial r}\right)_{i+1/2,j} &= \frac{r_{i+1/2}}{\Delta r}\left[\left(\frac{q^r_{i+3/2,j}-q^r_{i+1/2,j}}{r_{i+1}\Delta r}\right)-\left(\frac{q^r_{i+1/2,j}-q^r_{i-1/2,j}}{r_i\Delta r}\right)\right] \\ \left(\frac{\partial^2 q_r}{\partial z^2}\right)_{i+1/2,j} &= \left(\frac{q^r_{i+1/2,j+1}-2q^r_{i+1/2,j}+q^r_{i+1/2,j-1}}{\Delta z^2}\right). \end{aligned} \tag{4.46}$$

Boundary Conditions

Since, due to the use of a staggered grid, q_r is located on the axis of symmetry (see figure 4.6), we directly impose $q_r = 0$ there. The axial velocity component on the other hand is not defined on the axis. In order to impose the symmetry condition $\frac{\partial u_z}{\partial r} = 0$ a ghost cell is introduced on the left side of the axis. The condition then is imposed by setting $u_1^z = u_2^z$. Part (b) of figure 4.6 shows the situation at the right boundary of the computational domain. We consider two possibilities, no slip conditions and open boundaries. For the first case both velocity components are zero on the boundary. As q_r is located on the boundary, $q_r = 0$ is imposed directly. For the axial component we again introduce a ghost cell and impose

$$q_{Nr+1}^z = -q_{Nr}^z\,, \tag{4.47}$$

so that $u_{Nr+1/2}^z = (u_{Nr}^z + u_{Nr+1}^z)/2 = 0$. The case of an open boundary is more difficult because in reality the flow continues beyond the computational domain boundaries.

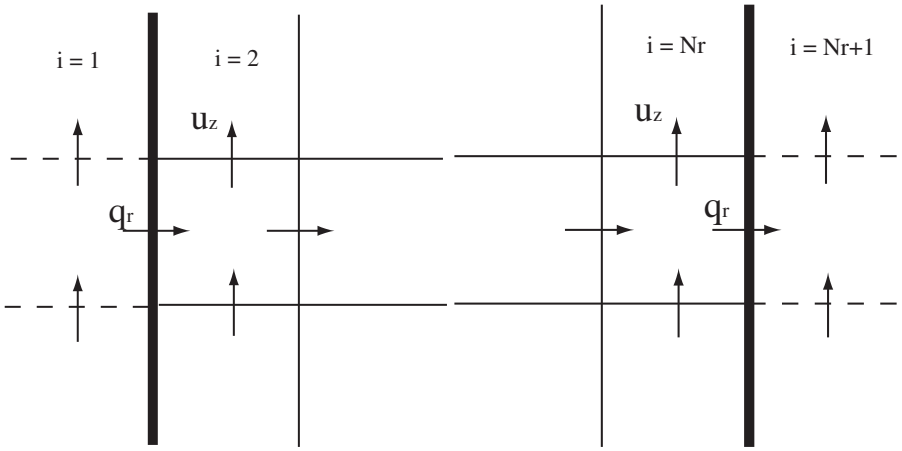

(a) axis (b) solid wall/open boundary

Figure 4.6: Implementation of the velocity boundary conditions. (a): On the axis of symmetry $q_r = 0$ is imposed directly since it is defined there due to the staggered grid. $\frac{\partial u_z}{\partial r} = 0$ is imposed by setting $u_1^z = u_2^z$. (b) Grid cell at the right boundary of the computational domain. The boundary may be a solid boundary, in which case both velocity components are zero. Thus for the radial velocity we set $q_r = 0$ directly, while for the axial velocity component we set $u_{Nr+1}^z = -u_{Nr}^z$ so that $u_z = 0$ on the boundary. In case of an open boundary the flow is kept as smooth as possible by imposing a zero normal gradient of the velocity.

Ideally in such a case the size of the domain is chosen large enough so that the domain of interest is not affected by the presence of the boundaries. This however is not always possible in view of the increase in computational cost. Many different boundary conditions have been proposed in the literature [91]. The basic approach is to keep the velocity field as smooth as possible near the boundaries. A popular choice for achieving this is to impose a zero velocity gradient normal to the boundary. Thus considering the right domain boundary we impose $\frac{\partial q_r}{\partial r} = 0$ and $\frac{\partial u_z}{\partial r} = 0$ as

$$q^r_{Nr+1/2,j} = q^r_{Nr-1/2} \quad , \quad u^z_{Nr+1} = u^z_{Nr} \,. \tag{4.48}$$

Pressure Poisson Equation with Dirichlet Condition

The pressure Poisson equation, Eq. (4.35) needs to be solved subject to a specified pressure at the interface. The method developed in [83] is used for this purpose. The standard discretization using a 5-point stencil for the Laplacian in cylindrical coordinates is

$$\begin{aligned} \left(\nabla^2 p\right)_{i,j} &= \frac{1}{r_{i,j}\Delta r^2}\left[r_{i+1/2,j}\left(p_{i+1,j}-p_{i,j}\right) - r_{i-1/2,j}\left(p_{i,j}-p_{i-1,j}\right)\right] \\ &\quad + \frac{1}{\Delta z^2}\left[\left(p_{i,j+1}-p_{i,j}\right) - \left(p_{i,j}-p_{i,j-1}\right)\right]. \end{aligned} \tag{4.49}$$

This discretization is valid when the interface does not cut any of the grid cells making up the discretization stencil. When this happens however a Dirichlet condition on the pressure needs to be imposed on the interface given by Eq. (3.5). Consider for example the situation depicted in figure 4.7 where the interface exists between nodes (i,j) and $(i-1,j)$. Suppose node (i,j) belongs to the liquid phase so that the interface pressure is given by p_s computed by means of Eq. (3.5). The pressure condition is imposed by constructing a ghost pressure p^{Ghost} at $(i-1,j)$ using linear extrapolation

$$p^{\text{Ghost}}_{i-1,j} = p_{i,j} - \frac{p_{i,j}-p_s}{\theta\Delta r}\Delta r = \frac{p_{i,j}(\theta-1)+p_s}{\theta}, \tag{4.50}$$

where θ gives the distance from node (i,j) to the interface in terms of the grid size Δr. Inserting this expression into Eq. (4.49) results in

$$\begin{aligned} \left(\nabla^2 p\right)_{i,j} &= \frac{1}{r_{i,j}\Delta r^2}\left[r_{i+1/2,j}\left(p_{i+1,j}-p_{i,j}\right) - r_{i-1/2,j}\frac{p_{i,j}-p_s}{\theta}\right] + \\ &\quad \frac{1}{\Delta z^2}\left[\left(p_{i,j+1}-p_{i,j}\right) - \left(p_{i,j}-p_{i,j-1}\right)\right]. \end{aligned} \tag{4.51}$$

The term containing the interface pressure p_s is known and therefore taken to the

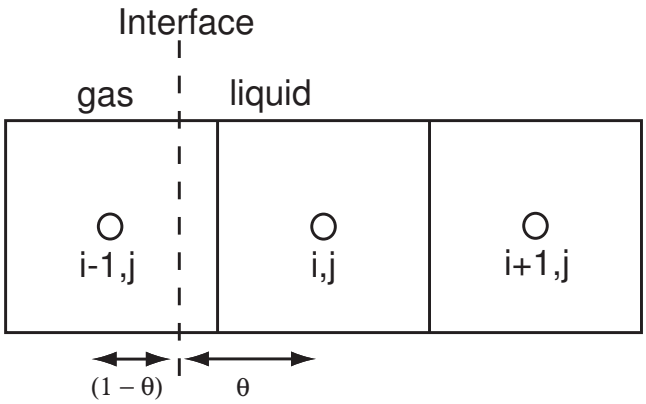

Figure 4.7: Interface between nodes (i, j) and $(i-1, j)$. θ denotes the distance from node (i,j) to the interface in terms of the grid spacing and ranges from zero to one.

right hand side of Eq. (4.35). A matrix is constructed by applying this equation to all grid cells. Each application constructs one row of the matrix. The resulting matrix is symmetric and can be efficiently solved by means standard methods. We use the conjugate gradient method which is an iterative method. To avoid numerical instabilities for θ close to zero a lower bound is set on it. We experimented with various bounds and found that satisfactory results are obtained when the interface is moved to the closest node in case $\theta < 0.01$.

Having solved for the pressure field the pressure gradient is used for the correction step of the projection method. Consider figure 4.7 again. For correcting the radial velocity component at $(i+1/2, j)$, the pressure gradient in the radial direction is computed as

$$\left(\frac{\partial p}{\partial r}\right)_{i+1/2,j} = \frac{p_{i+1,j} - p_{i,j}}{\Delta r}. \tag{4.52}$$

For correcting the radial velocity component located at $(i-1/2, j)$, which also belongs to the liquid region, the fact that the interface lies between points (i, j) and $(i-1, j)$ changes the computation of the pressure gradient. For this point the explicit value of the pressure at the interface, p_s, and the distance from the point to the interface, θ, are used in the approximation. Thus, the gradient is computed as

$$\left(\frac{\partial p}{\partial r}\right)_{i-1/2,j} = \frac{p_{i,j} - p_s}{\theta \Delta r}. \tag{4.53}$$

4.3.5 Velocity Extrapolation

The governing equations are solved on a fixed grid only in the liquid region. The discretization of the advection and viscous terms for nodes adjacent to the interface would involve irregular stencils. However, their use can be avoided by extrapolating the liquid velocity field far enough into the vapor region that the advection and viscous terms are adequately resolved as well as enabling the update of the level set function by means of Eq. (4.1). The velocity extrapolation can be carried out in various ways. Most methods however neglect the incompressibility constraint which, as noted by [84] and [44], is a rather important property for an accurate update of the interface. In [44] a method is proposed for the velocity extrapolation imposing the incompressibility constraint in the context of inviscid flow. Here we extend this method for viscous flow by imposing the zero tangential viscous stress condition on the interface using a Lagrange multiplier approach due to Popinet and Zaleski [85].

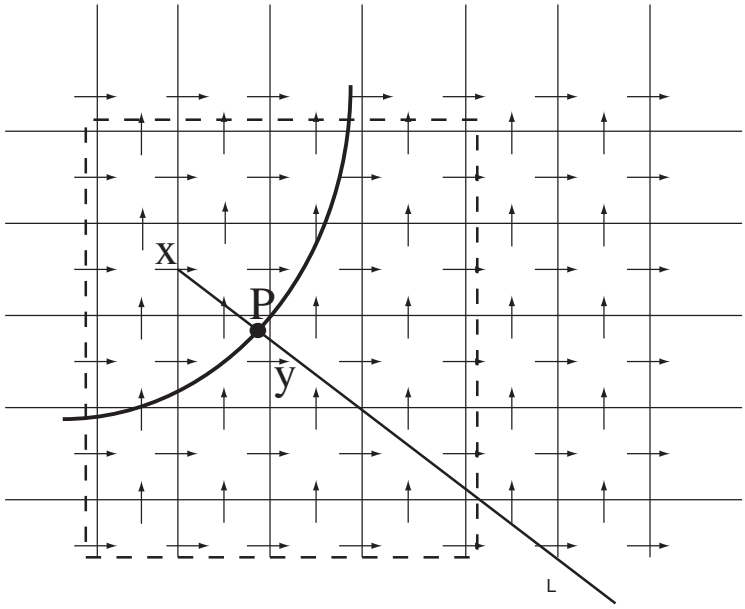

Figure 4.8: Selection of velocity components to be used for the linear least squares extrapolation of the velocity to the vapor region. The velocity component marked with X is where a value needs to be computed. A line is drawn that goes through X and is normal to the interface. The valid node closest to the intersection of the line with the interface, point P, is searched for and a stencil of 5x5 cells is constructed around this node. All valid nodes within this stencil are used in the least squares fit.

The extrapolation procedure consists of three steps. First the liquid velocity field is extrapolated linearly into the vapor by means of the least squares method. Then, a ghost pressure in the extrapolation region is found by solving a Poisson equation with the divergence of the linearly extrapolated velocity as the source term. Finally, the gradient of the ghost pressure is used to correct the extrapolated velocity so that it satisfies the divergence free constraint.

Consider a grid cell in the vapor where the velocity components are not computed through the momentum equations. We label the radial velocity component of this cell with X in figure 4.8. For the extrapolation of the velocity we need to select velocity components in the liquid that can be used to find a linear approximation to the velocity field. These components are selected by computing the coordinates of point P that lies on the interface and is closest to X. The location of P is found by using the interface normal vector at X computed from the level set function and the fact that the distance between X and P is given by the absolute value of the level set function at X due to the signed distance property. The coordinates of P can then be computed using

$$r_P = r_X + |\phi_X| \cos\beta \quad z_P = z_X + |\phi_X| \sin\beta\,, \tag{4.54}$$

where β is the angle between the normal vector and the radial axis. The radial component that lies in the liquid and is closest to P is then found by searching in a small neighborhood around P. This component is labeled by Y in the figure. Once this component has been found, a search is performed in a square region of size 5×5 cells centered at Y* (dashed square in the figure). All radial and axial velocity components within this square that are computed from the momentum equations are selected as the region for the velocity field approximation. We approximate the velocity field in this region as

$$\mathbf{u} = \mathbf{A} \cdot \mathbf{x} + \mathbf{u}_P \tag{4.55}$$

where

$$\mathbf{A} = \begin{pmatrix} \frac{\partial u_r}{\partial r} & \frac{\partial u_r}{\partial z} \\ \frac{\partial u_z}{\partial r} & \frac{\partial u_z}{\partial z} \end{pmatrix} \tag{4.56}$$

and

$$\mathbf{x} = (r - r_P, z - z_P,)^T \quad , \quad \mathbf{u}_P = (u_{r,P}, u_{z,P})\,. \tag{4.57}$$

The problem therefore is to find the matrix $\mathbf{A}$ and vector $\mathbf{u}_P$ so that the distance between the surface given by Eq. (4.55) and the liquid velocity components within the dashed region is minimal. This amounts to minimizing

*The choice of centering the square domain on the radial coordinate is arbitrary, it works just as well by centering it on the axial component

$$\mathscr{L}_0 = \sum_{k_1=1}^{N} \left(\frac{\partial u_r}{\partial r}(r-r_P) + \frac{\partial u_r}{\partial z}(z-z_P) + u_{r,P} - u_r(k_1) \right)^2 + \sum_{k_2=1}^{M} \left(\frac{\partial u_z}{\partial r}(r-r_P) + \frac{\partial u_z}{\partial z}(z-z_P) + u_{z,P} - u_z(k_2) \right)^2 \quad (4.58)$$

where N and M are the number of valid radial and axial velocity components within the 5×5 stencil and $u_r(k_1)$ and $u_z(k_2)$ are the valid radial and axial velocity components. The extrapolated velocity field should satisfy the zero tangential stress condition on the interface, Eq. (3.4). This constraint can be written in terms of the spatial derivatives of the velocity components as

$$Q = 2n_r t_r \frac{\partial u_r}{\partial r} + (n_r t_z + n_z t_r) \left(\frac{\partial u_r}{\partial z} + \frac{\partial u_z}{\partial r} \right) + 2n_z t_z \frac{\partial u_z}{\partial z} = 0\,, \quad (4.59)$$

where n_r, t_r are the radial components of the normal and tangent unit vector respectively, and n_z,t_z the axial components. The constraint can be added to Eq. (4.58) to get

$$\mathscr{L} = \mathscr{L}_0 + \lambda Q\,, \quad (4.60)$$

where λ is a Lagrange multiplier. Minimizing $\mathscr{L}$ gives 7 equations for the 7 unknowns $\frac{\partial u_r}{\partial r}$,$\frac{\partial u_r}{\partial z}$,$\frac{\partial u_z}{\partial r}$,$\frac{\partial u_z}{\partial z}$, $u_{r,P}$,$u_{z,P}$ and λ. Once the unknowns are solved for, the velocity field can be evaluated at the position of extrapolation. The extrapolation is done in a region satisfying $-K\Delta r < \phi < 0$ with K typically taken equal to 5.

The extrapolated velocity field obtained in this way is not divergence free. To make it so a projection method is used. A ghost pressure field (p^{Ghost}) for the extrapolated velocity in the vapor region can be obtained by solving

$$\nabla^2 p^{\text{Ghost}} = \nabla \cdot \mathbf{u}^{\text{extrap}}\,, \quad (4.61)$$

where $\mathbf{u}^{\text{extrap}}$ denotes the extrapolated velocity field which does not satisfy the incompressibility constraint. The equation is solved for the nodes at which the velocity has been extrapolated. Homogeneous Dirichlet conditions are imposed at $\phi = -K\Delta r$. In case $\phi > -K\Delta r$ throughout the vapor region, homogeneous Dirichlet conditions are imposed at the local minimum of the level set function, i.e. at cells satisfying ($\phi_{i,j} \leq \phi_{i\pm1,j}$ and $\phi_{i,j} \leq \phi_{i,j\pm1}$). At cell edges with a valid velocity component, i.e. one that is computed from the momentum equations homogeneous Neumann condition is imposed, since these need not be corrected. The extrapolated velocity field is then corrected as

$$\mathbf{u}^{\text{extrap,divfree}} = \mathbf{u}^{\text{extrap}} - \nabla p^{\text{Ghost}}\,, \quad (4.62)$$

with $\mathbf{u}^{\text{extrap,divfree}}$ the extrapolated velocity field that is corrected to satisfy incompressibility.

4.4 Energy Equation

4.4.1 General considerations concerning domain size and grid resolution

In the situations of present concern the entire flow is critically dependent on the phase change taking place at the vapor liquid interface which, in turn, hinges on the accurate evaluation of the temperature gradient. On uniform grids, as we use here, this can result in time consuming computations very quickly. However, the problems under consideration involve temperature fields that vary significantly only in the neighborhood of the bubble and are largely uniform throughout the rest of the domain. Therefore it is a waste of resources to solve for the temperature field in the whole domain. Instead, the energy equation is solved on a finer grid in part of the computational domain. Since velocity gradients are much smaller than temperature gradients, we simply interpolate the velocity field on the finer grid rather than solving the momentum equations on it.

Essentially then we use two domains, the complete domain on which the mass and momentum equations are solved, called the momentum domain, and a fraction of the complete domain on which the energy equation is solved, called the energy domain. The size of the energy domain depends on the type of problem. The only requirement is that the boundaries of the energy domain be sufficiently far away from the region where the temperature field varies significantly. Of course one may not know how to satisfy this condition a priori. In order to determine the needed size, we perform low resolution simulations to get an impression of the dynamics and determine the needed domain sizes from this.

Solving the energy equation on a smaller domain allows us to properly resolve the thermal boundary layer. As we are saving resources by using a small thermal domain, we may use a higher resolution for it and thus resolve the thermal boundary layer. An illustration of this approach is given in figure 4.9. Here we show the momentum (black lines) and thermal (red lines) grids used for simulating the collapse of a vapor bubble (black curve) due to condensation. The momentum domain extends to 10 times the bubble radius. The thermal domain however extends to only 1.25 times the bubble radius. Furthermore, the resolution of the thermal domain shown here is 4 time higher than that used for the momentum domain. We implemented a refinement of 2, 4, 8 and 16 times with respect to the momentum grid resolution.

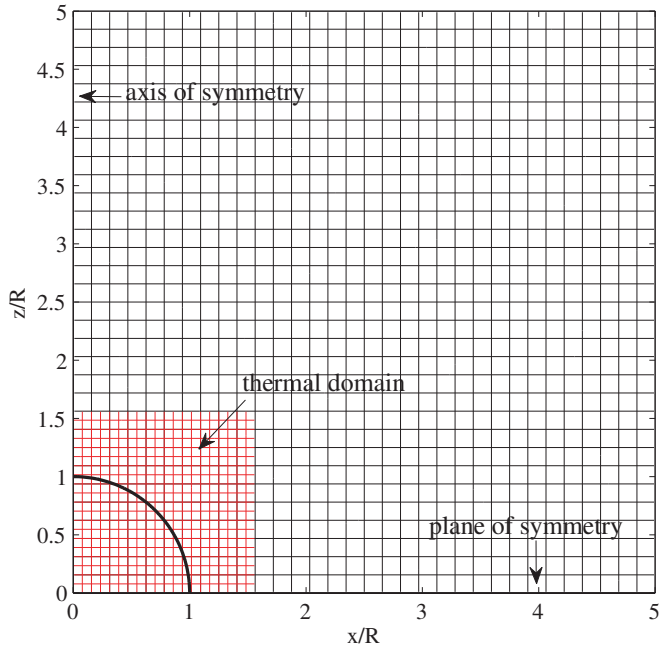

Figure 4.9: illustration of the thermal grid used for the simulation of a condensing vapor bubble. Only 1 in 8 grid lines is shown for clarity. The thermal domain can be taken very small due to a very thin thermal boundary layer. Hence the thermal resolution can be high without significantly increasing the computation times needed.

4.4.2 Spatial discretization

The spatial discretization of the convective and diffusive terms of the energy equation are treated with the same methods as used for the momentum equations. Thus, the convective term is approximated with the ENO method from section 4.2.3. The temperature must be solved subject to a known temperature at the interface. For this purpose the same discretization that was used in solving the pressure Poisson equation is used for the thermal diffusion term.

The only difference is the fact that the energy is solved on the energy domain which has a different resolution than the momentum domain. Therefore, for the discretization of the energy equation the velocity components and the level set function need to be calculated on the thermal grid. This is carried out by linear interpolation

from the momentum grid to the thermal grid.

4.4.3 Temporal discretization

The convection term is treated explicitly. As the thermal grid spacing is smaller than the momentum grid spacing, the convective time scale, Eq. (4.36), is computed using the thermal grid size Δr_{therm}.

An explicit treatment of the diffusion term would impose a time step restriction proportional to Δr_{therm}^2. Such a restriction would be too severe in view of the refined thermal grid. Therefore the diffusion term is treated implicitly.

The time integration is carried out with the first order Euler method and can be written as

$$\frac{T^{n+1}-T^n}{\Delta t} + (\mathbf{u}\cdot\nabla T)^n = \alpha\left(\nabla^2 T^{n+1}\right), \tag{4.63}$$

which after rearrangement becomes

$$T^{n+1} - \Delta t\,\alpha\left(\nabla^2 T^{n+1}\right) = T_n - \Delta t\,(\mathbf{u}\cdot\nabla T)^n. \tag{4.64}$$

This system of equations is solved by means of the conjugate gradient method.

4.4.4 Temperature field extrapolation

As the interface is moving it will inevitably cross over grid points. When this happens the grid point changes character. This is illustrated in figure 4.10 where the black dot belongs to the vapor at time step n and at time step $n+1$ it belongs to the liquid. Solving Eq. (4.64) requires valid values for the temperature and the advective term at time step n. In order to construct valid values, the temperature field is extrapolated linearly in the normal direction. For this purpose, first the temperature gradients normal to the interface on the liquid side, $(\nabla T_N) = \nabla T \cdot \mathbf{n}$, are computed in the neighborhood of the interface. These gradients are then extrapolated into the vapor region in the direction normal to the interface in a constant fashion. This is done using a method based on solving a PDE similar to the Level Set reinitialization equation [92]. We use this method because of its similarity with the reinitialization equation so that the same methods can be used for the integration. Temperature values for grid points in the vapor phase close to the interface may then be defined using the interface temperature, T_s, and the extrapolated normal gradients as $T^n_{i,j} = T^n_s + \phi^n_{i,j}(\nabla T_N)^n_{i,j}$ in view of the fact that the level set function is maintained as a signed distance function close to the interface and thus gives the smallest distance to it.

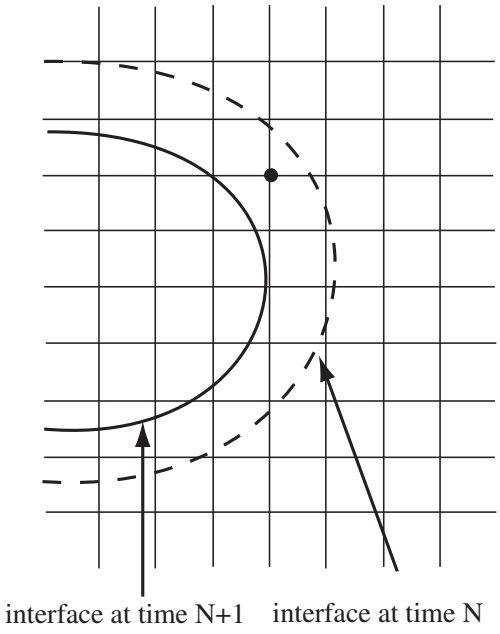

Figure 4.10: Illustration of the interface crossing over a node. At time t^n the black dot lies in the vapor region, while at time t^{n+1} it lies in the liquid region. In order to evaluate the right hand side of Eq. (4.64) a valid value for the temperature at time step n at the black dot must be constructed through extrapolation in the direction normal to the interface.

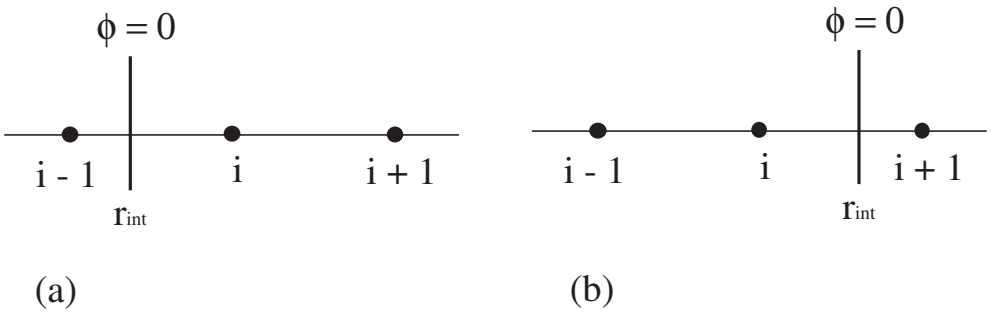

Figure 4.11: Illustration of the values used for approximating the thermal gradients in the liquid. (a): Gradient is approximated by Eq. (4.65). (b): Gradient is approximated by Eq. (4.66).

4.4.5 Computing the temperature gradient normal to the interface

The thermal energy flux through the liquid/vapor interface is needed for computing the change in vapor temperature, Eq. (3.13), as well as for the temperature field extrapolation described above. In order to resolve the phase change effects it is crucial that the temperature gradients be approximated accurately. As the temperature gradients at the interface may be large when the thermal boundary layer is thin we use the nodes closest to the interface for computing the gradient. Consider the approximation of the temperature derivative in the radial direction at node i, $\left(\frac{\partial T}{\partial r}\right)_i$, assuming this node lies in the liquid. If the nodes T_{i-1}, T_i and T_{i+1} all lie in the liquid, then the derivative is computed using T_i and either T_{i-1} or T_{i+1} depending on which lies closer to the interface, determined from the value of the level set function at those nodes. If the interface lies between T_i and T_{i-1}, see part (a) of figure 4.11, the derivative is computed using T_i and the surface temperature as

$$\left(\frac{\partial T}{\partial r}\right)_i = \frac{T_i - T_s}{r_i - r_{\text{int}}}, \tag{4.65}$$

where r_{int} is the radial coordinate of the interface location. In case the distance between the interface and node i is less than $0.01\Delta r$, T_{i+1} is used instead of T_i in order to avoid numerical instabilities. The same procedure is applied in case the interface lies between T_i and T_{i+1}, part (b) of figure 4.11. For this case the derivative is computed as

$$\left(\frac{\partial T}{\partial r}\right)_i = \frac{T_s - T_i}{r_{\text{int}} - r_i}. \tag{4.66}$$

Again, if the interface lies too close to node i, we use T_{i-1} instead of T_i.

The axial derivatives are computed in the same manner. Having computed both the radial and axial temperature derivatives, they may be multiplied by the appropriate normal vector components for computing the interface heat flux.

4.5 Summary of the numerical method

Now that all the components of the numerical method have been discussed a summary is in order. Step by step the computation proceeds as follows:

1. Advance the liquid/vapor interface by means of Eq. (3.15).
2. Reinitialize the level set function by iterating Eq. (3.16).
3. Compute the thermal gradient normal to the interface and extrapolate into the vapor region.

4. Extrapolate temperature field linearly into the vapor region in order to define valid values at nodes that may change their character at the next time step.

5. Compute the new surface temperature by means of Eq. (3.13), and from this the new vapor pressure by means of Eq. (3.7), serving as boundary condition for the interface.

6. Solve the energy equation, Eq. (3.3).

7. Solve the momentum equation by means of the projection method.

8. Extrapolate the new velocity field into the vapor region, using the method that enforces the interface stress condition and incompressibility.

9. Go back to step 1.

5 Validation

5.1 Introduction

For the purpose of validating the numerical method of chapter 4 we perform simulations of various bubble dynamics phenomena. For the validation of the mass and momentum equations we consider bubbles that perform damped volume oscillations. Such a bubble is described well by the Rayleigh-Plesset equation. The simulation results are compared with the direct integration of this equation. The order of accuracy, both temporal and spatial, are determined from this example. The dynamics of this oscillating bubble depend strongly on the conditions at the interface. The damping of the oscillation amplitude for instance is strongly dependent on the pressure jump at the interface due to the normal component of the viscous stress. This case is therefore a good test for the calculation of the pressure field and the velocity extrapolation.

The coupling between the thermal and momentum equations is illustrated by simulations of the collapse of a vapor bubble in a subcooled liquid. We show that grid independence is reached upon the refinement of the thermal grid.

5.2 Computational setup

Since in these simulations we consider a bubble in an unbounded liquid, we use symmetry about the equatorial plane $z = 0$ to decrease the size of the computational

domain by a factor of two. A schematic of the computational domain is shown in figure 5.1. The figure shows the interface of a bubble centered at the origin. A few grid lines are shown for illustration purposes.

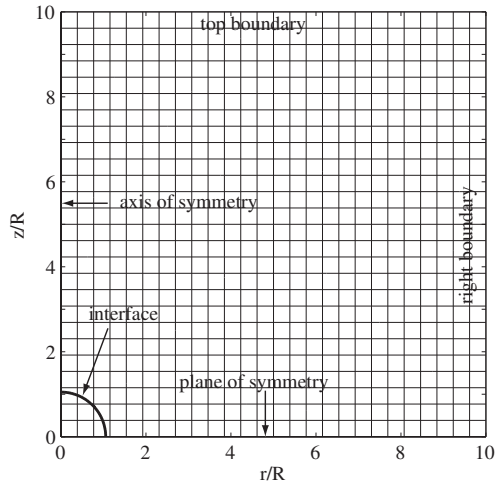

Figure 5.1: Schematic of the computational domain used for the simulations of this chapter. The interface for a unit radius bubble is shown, together with a few grid lines and the domain boundaries.

At the symmetry boundaries symmetry conditions are imposed:

$$\begin{aligned} q_r = 0\,, \quad \frac{\partial u_z}{\partial r} = 0 \qquad & \text{at} \quad r = 0\,, \\ u_z = 0\,, \quad \frac{\partial q_r}{\partial z} = 0 \qquad & \text{at} \quad z = 0\,. \end{aligned} \tag{5.1}$$

On the right and top boundaries the liquid is allowed to enter and exit the domain with zero normal velocity gradients by means of Eq. (4.48). A constant pressure p_∞ is imposed on these boundaries.

Due to the numerical implementation of these boundary conditions the bubble dynamics may be influenced by the presence of the boundaries. This is a feature that arises irrespective of the computational method used. To minimize this influence the domain boundaries should be placed far away from the bubble interface. However, the grids used in the simulations are uniform, thus using a large domain while still resolving the bubble adequately requires long computation times. It is therefore a matter of finding a compromise with regard to required accuracy versus runtime.

Furthermore, it is observed that the computational domain has a cylindrical symmetry, while the physical problems that we consider are spherically symmetric. Close to the bubble this geometric dissimilarity does not affect the structure of the flow field noticeably. Near the boundaries on the other hand it may have a large effect depending on the flow field. For this reason also the size of the computational domain must be large enough so that the influence of this geometric dissimilarity on the bubble dynamics is minimized.

The governing equations are non-dimensionalized in terms of the bubble initial (or equilibrium) radius R_0, a velocity scale V and a time scale $t^\star$.These scales depend on the specific problem at hand. Nondimensional numbers are then derived that characterize the problem

$$Re = \frac{\rho R_0 V}{\mu}, \quad We = \frac{\rho R_0 V^2}{\sigma}, \quad Pe = \frac{R_0 V}{\alpha}. \tag{5.2}$$

5.3 Static bubble – spurious currents

A static spherical bubble placed in an unbounded liquid should remain at rest, assuming gravity is negligible. This situation has been simulated in order to study the so-called spurious currents that are a well-known problem in simulations of this type [21, 93]. The origin of these currents lies in the difficulty of calculating the curvature and the interface pressure jump with sufficient accuracy and are therefore a stringent test of the numerical method.

The bubble is initialized with a radius $R_0 = 10\,\mu$m. The pressure at infinity, p_∞, is taken to be atmospheric. The pressure difference across the interface is given by the Laplace pressure, $\Delta p = 2\sigma/R_0$, with $\sigma = 0.073$ N/m, the surface tension of water. The velocity scale is taken as $V = \sqrt{\Delta p/\rho} = \sqrt{2\sigma/R_0\rho}$. The simulation was carried out on a computational domain where the boundaries were located at a distance $4R_0$ from the origin using a relatively coarse grid of 32×32 cells.

The pressure field is shown in 5.2. The pressure p_B inside the bubble has been set to $p_g = p_\infty + 2\sigma/R_0$ and not calculated. The pressure in the liquid is solved by imposing at the interface the value p_g decreased by the surface tension and viscous contributions according to Eq. (3.5). Note that in the calculation the curvature is not prescribed to be $2/R_0$ but is calculated by the algorithm. The figure also shows the velocity field that is generated around the bubble and its extrapolation into the vapor phase. The maximum of this non-physical velocity field over the course of the simulation can be seen in figure 5.3. We show the results of two simulations. One was done with the velocity field extrapolation as explained in chapter 4, i.e. with the incompressibility constraint satisfied, and the “subcell fix” for the reinitialization

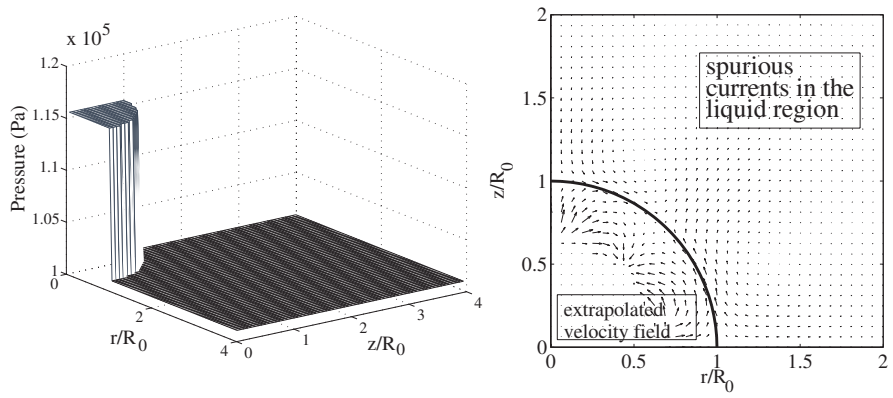

Figure 5.2: The figure on the left illustrates the sharp solution of the pressure field for a bubble with $R = 10\ \mu$m in an unbounded liquid. The pressure at infinity is imposed at atmospheric, the vapor pressure is given by the Laplace pressure due to surface tension. On the right the non-physical velocity field induced by the discretization is shown. The magnitude of these spurious currents are small compared to the velocity scale of the problem and will therefore not affect the solution of the simulations

equation. The other is omitting the projection correction to the extrapolated velocity, and the standard WENO method for the reinitialization. The magnitude of the non-physical velocity currents is of the order of 10^{-3} and slightly smaller with the divergence-free extrapolation method. While the effect is thus small in both cases, more important is perhaps that, with the divergence -free extrapolation the magnitude of the spurious currents does not grow in time so that their effect remains limited. For the linear extrapolation, though comparable in magnitude, there is a slight increase with time that seems to persist. These results are comparable with those in the literature [21, 94] where they have been accepted as sufficiently accurate. We can conclude that spurious currents are not a matter of great concern in our simulations.

5.4 Radial bubble dynamics - volume oscillations

The radial dynamics of a bubble in an unbounded liquid are governed by the Rayleigh-Plesset equation

$$R\frac{\mathrm{d}^2R}{\mathrm{d}t^2}+\frac{3}{2}\left(\frac{\mathrm{d}R}{\mathrm{d}t}\right)^2=\frac{1}{\rho}\left[p_g-p_\infty-\frac{2\sigma}{R}-\frac{4\mu}{R}\frac{\mathrm{d}R}{\mathrm{d}t}\right], \tag{5.3}$$

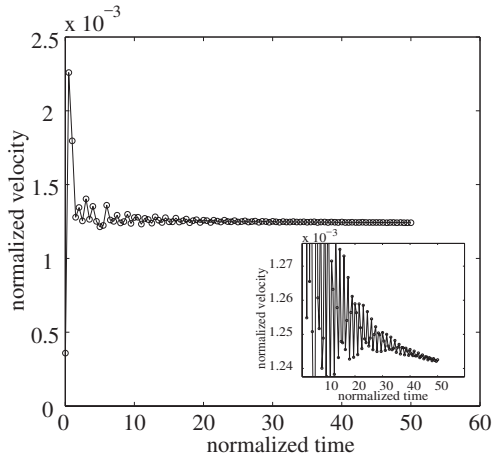

(a)

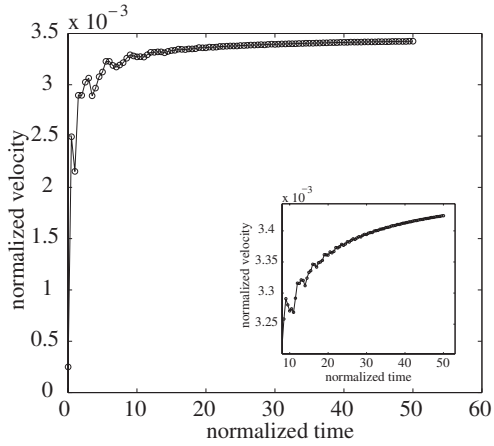

(b)

Figure 5.3: Maximum velocity magnitude as a function of time. The inserts are close up views. (a) Velocity extrapolation satisfying incompressibility, and subcell method for reinitialization of level set function. (b) Linear velocity extrapolation and standard WENO for reinitialization.

where R is the instantaneous bubble radius, p_∞ the ambient pressure and p_g the bubble internal pressure. For validation purposes it suffices to compute the gas pressure from a simple model. We use the relation for an adiabatic perfect gas

$$p_g = p_{eq}\left(\frac{V_{eq}}{V}\right)^{\gamma}, \tag{5.4}$$

in which the quantities with subscripts are the values at the equilibrium state, V is the instantaneous volume and $\gamma = 1.4$ the adiabatic index. For the purpose of validating the code we simulate a gas bubble with equilibrium radius R_{eq} = 23.75 μm. The bubble is initialized with a radius $R_{t=0} = 25$ μm so that it is slightly over-expanded with respect to its equilibrium radius causing it to oscillate. The oscillations are damped by viscosity.

Scales for this problem are defined as R_{eq}, velocity scale $\sqrt{\frac{p_\infty}{\rho}}$ and time scale $t^\star = R_{eq}/V$. For the liquid we take the physical properties of water: density $\rho = 10^3$ kg/m^3, viscosity $\mu = 10^{-3}$ kg/(ms) and surface tension $\sigma = 0.073$ N/m. With these parameters the nondimensional numbers characterizing the problem are $Re = 238$ and $We = 33$.

The velocity field around a spherical bubble with radius R and velocity $\dot{R}$ in an infinite medium in cylindrical coordinates is

$$u_r = \dot{R}\left(\frac{R}{r}\right)^2 \sin\theta, \quad u_z = \dot{R}\left(\frac{R}{r}\right)^2 \cos\theta\,. \tag{5.5}$$

In view of the comments made concerning the effect of a finite-size computational domain and the dissimilar symmetries of the physical problem and computational domain we performed the simulation on a domain with a size of 10 bubble radii.

The oscillation frequency of the bubble depends on the amount of inertia in the system. Therefore, instead of using Eq. (5.3) we use a modified Rayleigh-Plesset equation which imposes p_∞ not at infinity but at a distance S from the bubble center. By taking S to be the radius of a sphere with the same volume as our computational domain, the amount of inertia in our simulation is approximately the same as in the physical system. This allows a better comparison. The modified Rayleigh-Plesset equation is [95]

$$\frac{S-R}{S}\left\{R\frac{\mathrm{d}^2R}{\mathrm{d}t^2} + \left[2 - \frac{\left(S^2+R^2\right)(S+R)}{2S^3}\right]\left(\frac{\mathrm{d}R}{\mathrm{d}t}\right)^2\right\} = \frac{1}{\rho}\left[p_g - P_S - \frac{2\sigma}{R} - \frac{4\mu}{R}\frac{\mathrm{d}R}{\mathrm{d}t}\right]. \tag{5.6}$$

To illustrate the effect of the finite domain size on the oscillation dynamics of the bubble we plot in figure 5.4 the solution of Eqs. (5.3) and (5.6) as the black and red

curve respectively. The value of S in Eq. (5.6) is chosen such that the volume of the spherical shell is approximately the same as the volume of the computational domain used for carrying out the simulations. It can be seen that the oscillation frequency is noticeably affected, the bubble in the bounded liquid oscillates faster due to the smaller liquid inertia. It is therefore clear that this effect must be taken into account in analyzing the simulation results.

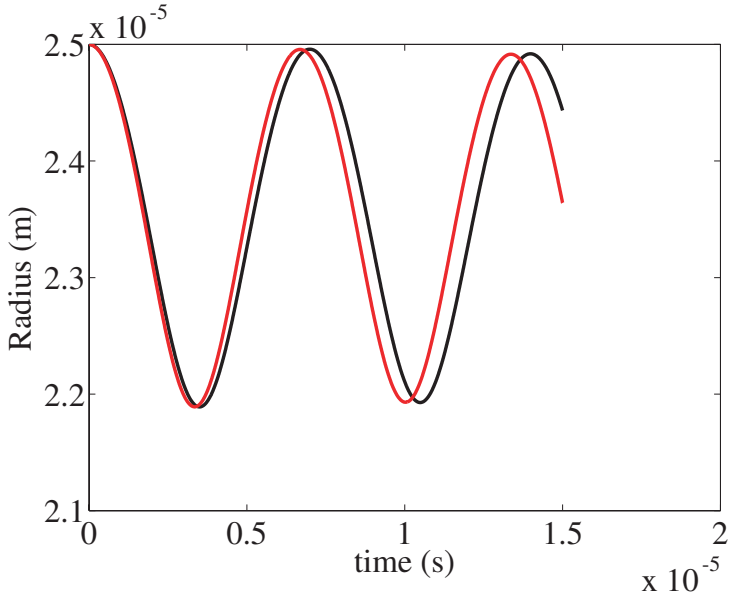

Figure 5.4: Illustration of the effect of a finite domain on the oscillations of a bubble. The black curve is the result of assuming an unbounded liquid, described by Eq. (5.3), whereas the red curve is the result of solving Eq. (5.6) where S is chosen such that the volume is approximately equal to the volume of the computation domain used for carrying out the simulation.

A comparison between the analytic and numerical isocontours of the velocity magnitude at an arbitrary time is shown in figure 5.5(a). The red curves are the analytic expressions, Eq. (5.5). The computed isovelocity contours, at the same time, are shown by the blue curves. The effect of the mismatch in geometry is now clearly visible. For distances up to 5 bubble radii the isocontours coincide nicely. For larger distances the cylindrical shape of the domain is starting to be felt as shown by the non-circular shape of the blue isocontours. However, as the magnitude of the velocity field is inversely proportional to the squared distance to the bubble interface,

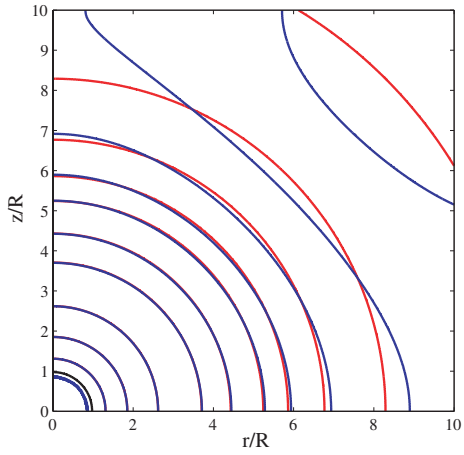

(a)

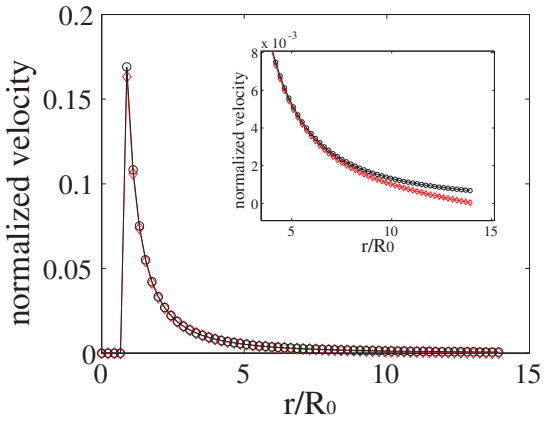

(b)

Figure 5.5: (a) Isocontours of the velocity field, both analytic expression (red curves) and simulation result (blue curves). The black curve is the bubble interface. The mismatch between computation domain geometry and the physical spherical symmetry starts to be noticeable at approximately 5 bubble radii. (b) The analytical (black) and simulation (red) velocity magnitude along the diagonal of the computational domain at $t^\star = 2.25$. The inset is a close up at the top right corner of the domain. The discrepancy due to the dissimilar geometries is less than 1% of the interface velocity.

the velocity magnitude near the domain boundaries is very small and thus the effect is not severe. This is shown in figure 5.5(b) where the velocity along the diagonal of the computational domain is plotted. Near the boundaries the discrepancy in analytic and computational result for the velocity is less than one percent. For this reason we conclude that our method is able to reproduce the prediction of the Rayleigh-Plesset equation with sufficient accuracy.

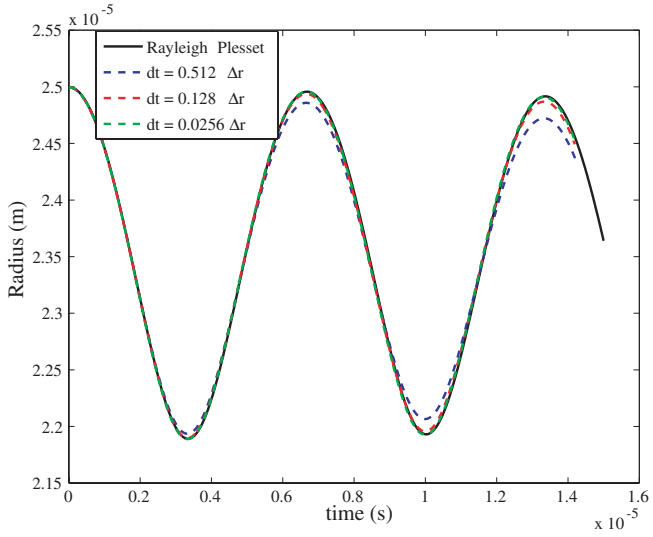

Figure 5.6: Results for the bubble radius as a function in time. The domain used in these simulation was 10 times the equilibrium bubble radius. The number of grid points used was $[256 \times 256]$. The results are shown for various constant time step sizes

5.4.1 Temporal and spatial convergence

We start by determining the temporal accuracy of the numerical method. For this purpose we perform several simulations of the same oscillating bubble problem of the previous section with the same spatial resolution but varying time steps. We used here a grid of $[256 \times 256]$ cells so that the grid spacing is $\Delta r/R_{eq} = 0.039$. The time step is varied from $0.0256\Delta r/R_{eq}$ to $0.512\Delta r/R_{eq}$. The results for the bubble radius as a function of time are shown in figure 5.6 together with the result of the direct integration of Eq. (5.6). Clearly the time step has a large influence on the results,

which may have been expected as the time integration of the governing equations is done with the first-order Euler scheme.

In order to determine the scaling of the error with the time step we consider the norms

$$L_1 = \frac{\sum |f^r - f|}{\sum |f^r|}, \quad L_2 = \frac{\left(\sum |f^r - f|^2\right)^{1/2}}{\left(\sum |f^r|^2\right)^{1/2}}, \tag{5.7}$$

in which f denotes the quantity for which the error is calculated and the superscript r denotes the reference value. The summation is done over all grid points that lie in the liquid region, i.e. all points that satisfy $\phi > 0$. For f we take the pressure, the radial and the axial velocity components. In order to isolate the effect of the time step, it is not possible to use as reference values the analytic solution as the contribution of the nodes far from the bubble where the solution is affected by the dissimilar geometries would end up overwhelming the error. Rather, we use the results obtained with the smallest time step. Figure 5.7 shows the L_2 norm for the pressure on a log-log plot the slope of which gives the order of the method. These values were calculated at a non-dimensional time $t^\star = 6$. The temporal convergence rate is close to 1 as expected.

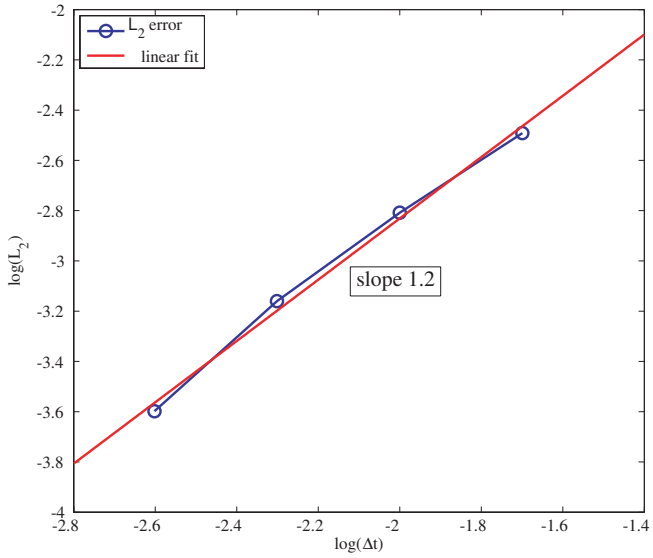

Figure 5.7: L_2 error norm for the pressure field. The slope, giving the order of the time integration is 1.2 as expected from a first order Euler method.

	Δt_1	Δt_2	Δt_3	Δt_4	order
Pressure					
L_1	1.402e-4	3.847e-4	8.648e-4	1.794e-3	1.23
L_2	2.523e-4	6.919e-4	1.555e-3	3.224e-3	1.23
radial velocity component					
L_1	9.566e-3	2.644e-2	5.937e-2	1.206e-1	1.22
L_2	1.147e-3	3.162e-3	7.092e-3	1.441e-2	1.21
axial velocity component					
L_1	9.629e-3	2.653e-2	5.947e-2	1.208e-1	1.21
L_2	1.151e-3	3.166e-3	7.103e-3	1.443e-2	1.21

Table 5.1: L_1 and L_2 norms for the pressure, radial and axial velocity components

The L_1 and L_2 norms for the pressure and both velocity components are listed in table 5.1

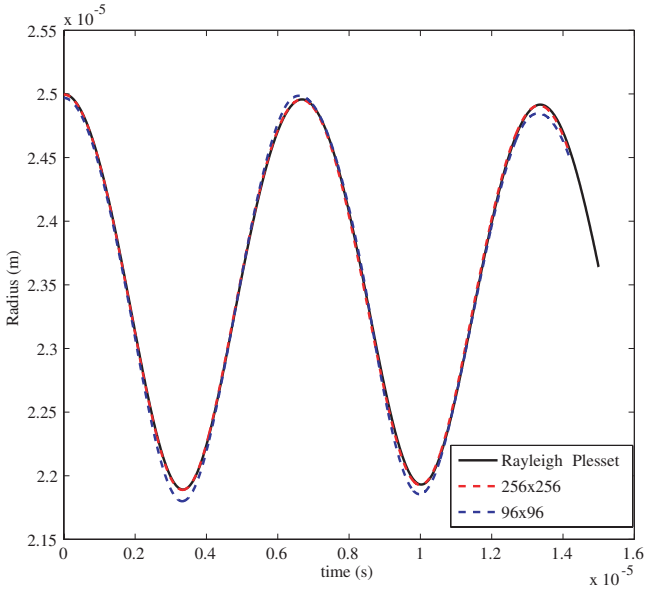

Figure 5.8: Radius as a function of time for a grid of $[96 \times 96]$ (blue dashed line) and $[256 \times 256]$ (red dashed line). Both simulations were done with the same fixed time step. The black solid line is the result of the modified Rayleigh-Plesset equation, Eq. (5.6)

Next the spatial convergence rate is determined. For this purpose simulations have been carried out with various grid resolutions. The time step was the same for all simulations, $0.0256\Delta r^{highres}/R_{eq}$ with $\Delta r^{highres} = 0.039$ the highest resolution used. The spatial convergence rate is determined by taking the results of the simulation done at the highest resolution as a reference. The errors are calculated by means of bilinear interpolation between grids. Figure 5.8 shows the results for the bubble radius as a function of time for 2 grid resolutions. The lowest resolution ($\Delta r/R_{eq} = 0.104$) and a high resolution ($\Delta r/R_{eq} = 0.039$), for which the results have converged, are compared to the Rayleigh-Plesset solution. Figure 5.9 shows the error norms as a function of grid size on a log-log scale for the radial velocity component. The slope of this line give the order of accuracy of the method. As expected the spatial discretization is very close to second order.

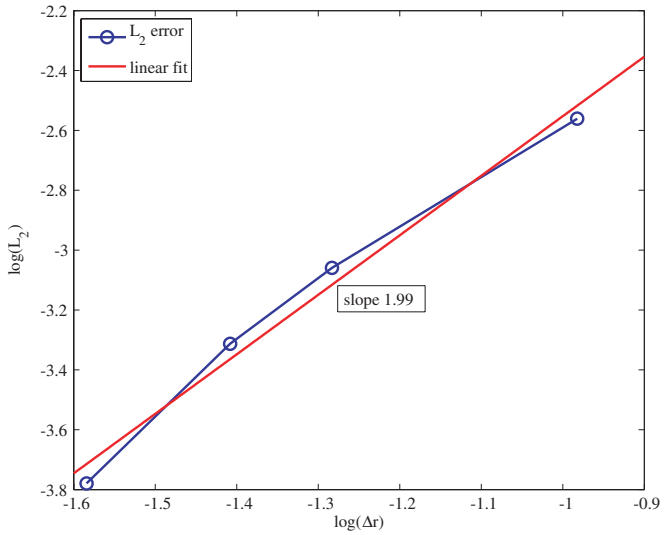

Figure 5.9: L_2 error norm for the radial velocity component as a function of grid size. The red line is a linear fit. The slope is very close to 2.

In the present algorithm the interface velocity is calculated by interpolating the liquid velocity between the value at the node closest to the interface and the extrapolated value in the bubble. Thus, a comparison of the bubble surface velocity serves as a good test of the accuracy of the extrapolation. Figure 5.10 compares the numerical velocity at the bubble surface with the analytic one as given by Eq. (5.5) evaluated

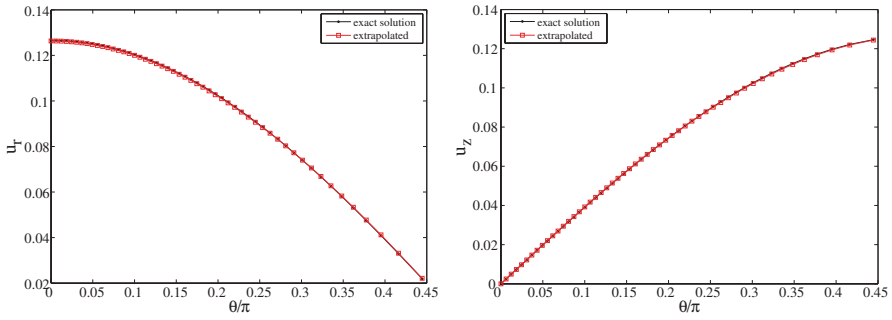

(a) (b)

Figure 5.10: (a) radial velocity component along the interface (b) axial velocity component along the interface

for $r = R$ at a non-dimensional time $t^\star = 2.25$, at which the radius and velocity are $R = 1.012$ and $\dot{R} = 0.127$. The comparison is excellent.

5.5 Collapsing vapor bubble in a subcooled liquid

In order to test the coupling between the thermal and mechanical parts of the numerical method we consider the collapse of a spherical vapor bubble in an unbounded subcooled liquid. Far away from the bubble the pressure is atmospheric. The liquid temperature is uniform throughout the liquid and is just below the saturation temperature. Since the vapor temperature initially is the same as the liquid temperature, the vapor pressure given by Eq. (3.7) is lower than atmospheric causing the bubble to collapse. From a numerical point of view this is an extremely challenging problem for several reasons. First of all, because of the strong interdependency of the thermal and momentum fields, accurate thermal gradients are crucial for calculating the fluid flow correctly. Therefore, the energy equation needs to be solved on a grid with very high resolution. Furthermore, the initial condition of a uniform temperature field proves very hard, if not impossible, to deal with because a boundary layer develops starting from zero thickness which is unresolvable. One can see this considering Eq. (3.13). Initially the term within the integral containing the thermal gradient is zero because the temperature field is uniform, i.e. there is no energy conduction taking place. The term containing the latent heat however is positive since the bubble is collapsing. It follows then that the bubble surface temperature will increase. As this happens in the numerical treatment, in the very early stages of the computations the

temperature field becomes discontinuous because the thermal conduction has not had time to create a boundary layer that can be resolved on the numerical grid. Therefore, in this stage of the simulation the thermal gradients depend on the grid resolution and thus give different results for every grid size.

The problem can be circumvented by starting from a temperature field that already has a boundary layer that can be resolved. This is the approach we take here. The situation that we simulate is as follows. The initial bubble radius is 1 mm, the initial vapor temperature is 373.15 K. The liquid subcooling is 3.35 K. The temperature field is initialized with an exponentially decaying distribution near the bubble

$$T(r,z,0) = T_\infty + \Delta T \exp\left(-\frac{|\mathbf{x}| - R_0}{\delta}\right), \tag{5.8}$$

with ΔT the initial subcooling, $\delta = 0.025 R_0$ the width of the boundary layer and $|\mathbf{x}| - R_0$ the distance between a point in the computational domain the initial bubble radius. The physical properties of the liquid are that of water at atmospheric pressure and 373.15 K: $\rho = 955.1$ kg/m^3, $\mu = 2.67 \times 10^{-4}$ kg/ms, $k = 0.68$ W/m, $\alpha = 1.69 \times 10^{-7}$ m^2/s, $L = 2257 \times 10^3$ J/kg and $\sigma = 0.059$ N/m. The computational domain on which the momentum equations are solved extends to 5 times the bubble initial radius, with a grid spacing of $\Delta r/R_0 = 0.039$. The domain for the thermal equation can be taken much smaller as the temperature varies only in the close neighborhood of the bubble. Thus we take a domain that extends to only 1.5 times the initial bubble radius. The grid spacing for the thermal equation is varied with values

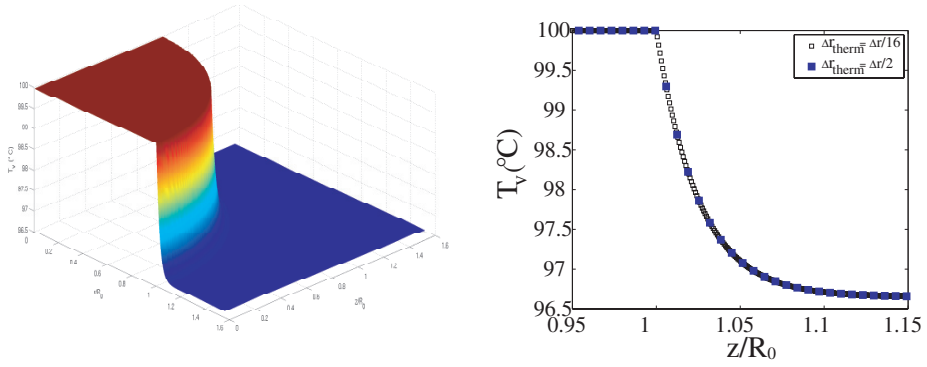

Figure 5.11: (left) Initial temperature field showing the thin boundary layer. (right) close up view of the initial temperature field on the axis of symmetry in the neighborhood of the liquid-vapor interface. The boundary layer is well resolved on all thermal grid resolutions.

of $\frac{1}{2}\Delta r/R_0, \frac{1}{4}\Delta r/R_0, \frac{1}{8}\Delta r/R_0$ and $\frac{1}{16}\Delta r/R_0$. The initial temperature field is shown in figure 5.11. The figure on the right shows the temperature variation along the axis of symmetry in the region of the interface for the coarsest and finest thermal grids. The thermal boundary layer is relatively thick so even on the coarsest thermal grid it contains several points. On the finest grid it is well resolved considering the number of points inside the boundary layer.

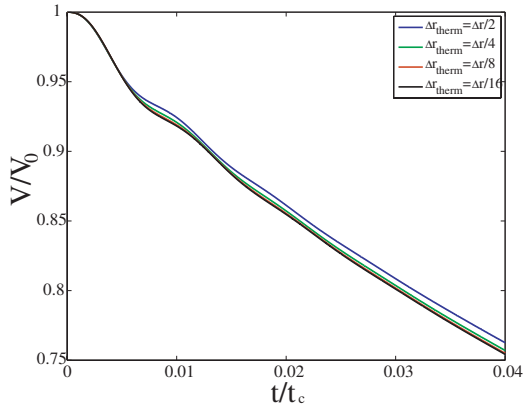

(a)

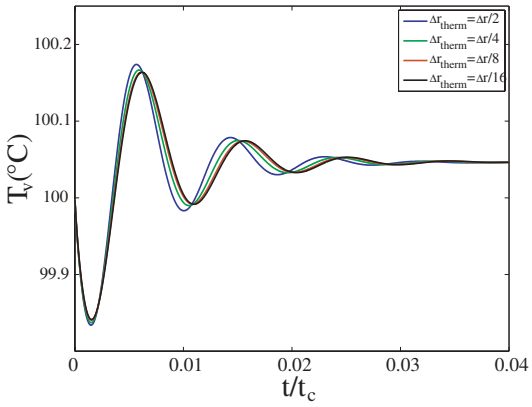

(b)

Figure 5.12: (a) Normalized bubble volume, showing small "wiggles" due to competing inertial and thermal effects. (b) Bubble surface temperature.

The results for the bubble volume and vapor temperature during the early stages of collapse are shown in figure 5.12. The results are normalized with a time scale which is a crude estimate of the collapse time of a stationary spherical vapor bubble due to Florschuetz and Chao [96]. They derived the time scale by balancing the rate at which latent heat is liberated at the bubble surface with the rate at which it can be conducted away through the thermal boundary. In this it is assumed that the bubble surface temperature remains fixed at the saturation temperature at ambient pressure p_∞. The collapse time is then estimated as

$$t_c = \frac{\pi}{4Ja^2}\frac{R^2(0)}{\alpha}, \tag{5.9}$$

with the Jakob number defined as

$$Ja = \frac{\rho c_p(T_{\text{sat}} - T_\infty)}{L\rho_v}, \tag{5.10}$$

with ρ and c_p the liquid density and specific heat and L the latent heat of phase change. With the parameters as stated earlier the collapse time is $t_c = 46$ ms. It can be seen from figure 5.12 that the results of the thermal grid spacing of $\Delta r/8$ and $\Delta r/16$ lie very close to each other and so we consider the results of the latter as grid independent.

The volume shows some wiggles in the very early stages of collapse, due to competing effects of phase change and inertia, which will be explained later. During the collapse the bubble stays spherical. Figure 5.13 shows the bubble interface together with isocontours of the temperature field at four instances during the collapse. Between $t/t_c = 0.6$ and $t/t_c = 1$ the temperature field loses its spherical symmetry. This is due to the fact that the spherical shape is inherently unstable during collapse compounded by the beginning of an under-resolution due to the shrinking of the bubble. The only remedy for this would be to increase the grid resolution but, as the interesting dynamics has already occurred by this time, we did not pursue this.

In [97] and [73] computations of the same system are reported. Their computations were based on a spherical model and a boundary fitted code respectively. They showed that the bubble undergoes a rebound in the early stages, i.e. there is a short period where the bubble actually grows. The reason for this is that, because the vapor pressure is smaller than the ambient, initially the bubble collapses relatively fast. During this period of fast collapse the latent heat released due to condensation cannot be carried away through the thermal boundary layer and raises the surface temperature by such an amount that the vapor pressure becomes high enough to bring the collapse to a halt and initiate a short period of rebound. The fact that this effect is not captured in our simulation is due to the initial condition of the vapor temperature

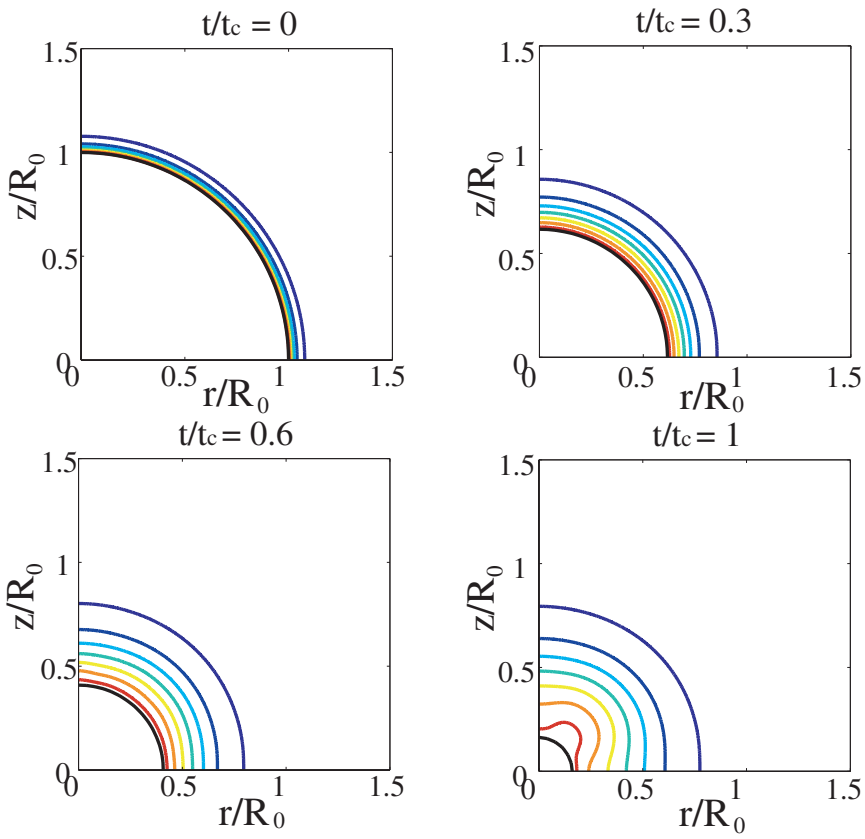

Figure 5.13: Temperature field and bubble interface at four instants during the bubble collapse. Colors: isocontours of the temperature field varying from $T_\infty = 96.65\,°\mathrm{C}$ to $100\,°\mathrm{C}$. Black curve: vapor/liquid interface.

which gives it the same pressure as the ambient pressure. Thus, the initial collapse is much weaker than in [97] and [73]. This is reflected by the small variation in vapor temperature in figure 5.12(b). As the collapse proceeds slowly, there is ample time to carry away the energy released by the condensation. Consequently, the vapor temperature does not increase much and no rebound is seen.

Capturing the rebound in the early stages of the collapse provides a stringent test of the accuracy of the present phase change and heat transport calculation. In order to test whether our code can predict this feature we performed a simulation with the same parameters as the previous case except for the initial temperature field.

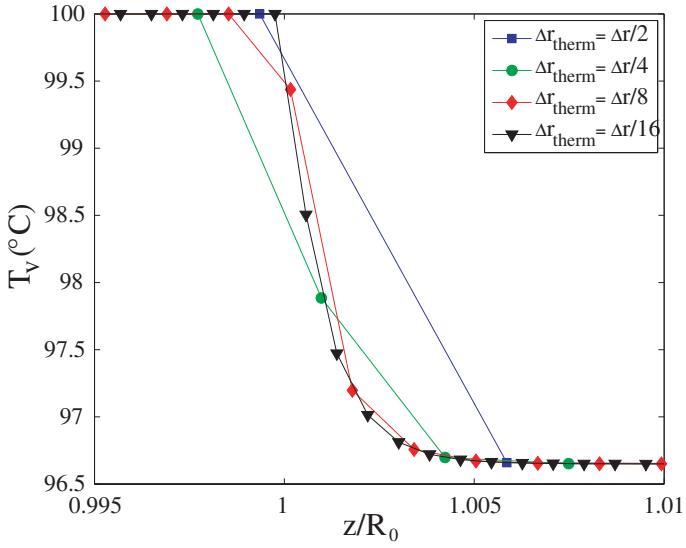

Figure 5.14: close up view of the initial temperature field on the axis of symmetry in the neighborhood of the liquid-vapor interface. The initial boundary layer is very thin and therefore difficult to resolve well. For this case, only the largest refinement is able to resolve the boundary layer adequately.

For this simulation we decreased the width of the thermal boundary layer to 0.1% of the initial bubble radius. The simulation was performed on the same domain but a higher resolution was used. The momentum grid resolution was $\Delta r/R_0 = 0.013$, the thermal grid resolution was again $\frac{1}{2}\Delta r/R_0, \frac{1}{4}\Delta r/R_0, \frac{1}{8}\Delta r/R_0$ and $\frac{1}{16}\Delta r/R_0$. The initial temperature field along the axis of symmetry for these different thermal grid resolutions is shown in figure 5.14. It is clear from this figure that the initial boundary layer is not resolved as well as it was in the previous simulation. The lowest thermal grid resolution has no temperature values inside the boundary layer. Even for the highest thermal resolution the boundary layer contains approximately 5 points which is not that many, but enough to see the rebound. The bubble volume and vapor temperature during the early stages are shown in figure 5.15 for all four resolutions. The large temperature gradients that exist initially cause the interface temperature to decrease due to large conductive heat loss. This results in a much faster collapse than in the previous simulation. The latent heat released due to the fast condensation raises the interface temperature and with it the pressure. This increase is large enough for the flow to stop and reverse direction for a short duration as indicated by the rebound

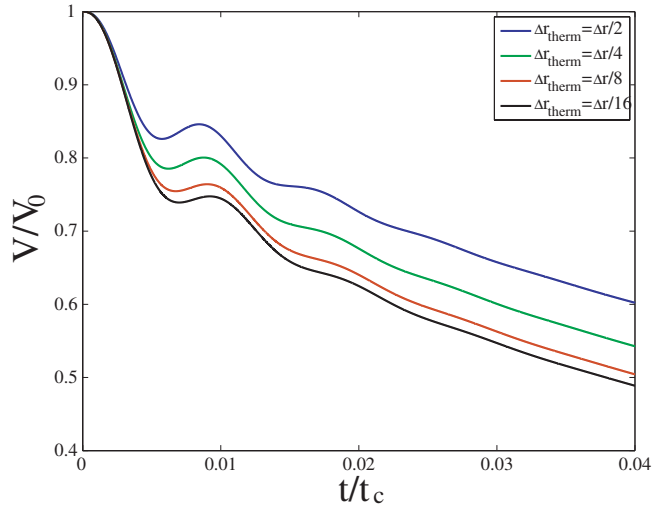

(a)

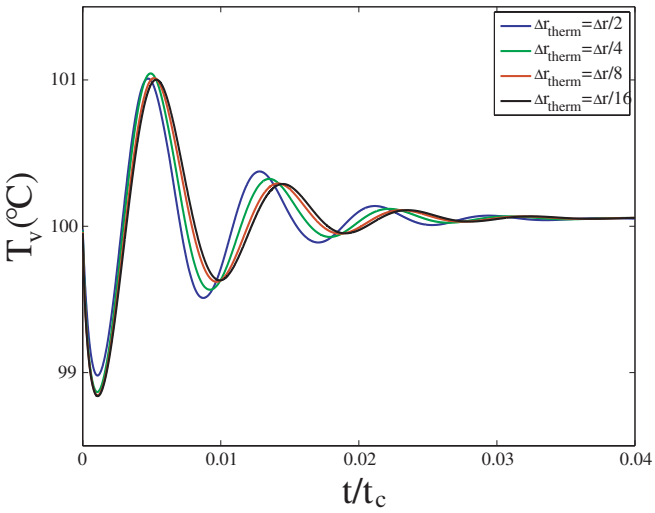

(b)

Figure 5.15: (a) Normalized bubble volume, the rebound is captured, although grid independence has not been reached yet. (b) Bubble surface temperature.

in bubble volume. Even though complete grid independence has not been reached, it is clear that the difference between successive resolutions decreases. The qualitative behavior of the volume and vapor temperature as functions of time is comparable to those of [73].

5.6 Conclusions

We have simulated various test problems in order to validate the numerical method of chapter 4. Simulations concerning a stationary spherical bubble illustrated the sharp treatment of the interface. Spurious velocity currents are generated at the interface due to the discretization. However, the divergence-free velocity extrapolation decreases their magnitude. Furthermore, the magnitude of these currents was seen to remain bounded when using this velocity extrapolation. Therefore, the effect of such currents on computations concerning long time behavior of bubble motion may be expected to be limited.

The accuracy of the solution of the mass/momentum equations was demonstrated by computing the damped volume oscillations performed by a bubble. These oscillations are described by the Rayleigh-Plesset equation. Good agreement was achieved between the full integration of the Navier-Stokes equations and the direct integration of the Rayleigh-Plesset equation. A modified equation, reflecting the finite amount of inertia was used for a better comparison. Subsequently the temporal and spatial orders of convergence were determined from this test problem. The method is as expected first-order accurate in time and second-order accurate in space.

The coupling of thermo-mechanical effects was studied through the collapse of a vapor bubble situated in a subcooled liquid. This problem is a very challenging one from a numerical point of view because of the strong coupling between the thermal and inertial effects, and the existence of an extremely thin thermal boundary layer. We were able to achieve grid independence in case the thermal boundary layer was well resolved. The dynamics of the vapor bubble in this case however did not show a rebound as predicted by the spherical model of [97]. Simulation of the same system with a thinner thermal boundary layer of the initial temperature field however showed the rebound effect although complete grid independence was not achieved with the resolutions that were used.

6

Vapor bubble dynamics in a tube

6.1 Introduction

In chapter 2 we described simplified models for vapor bubble growth and collapse in a micro-tube. The model developed included some thermal effects and an assumed temperature distribution and good quantitative agreement with the experimental data was obtained. It was shown that the maximum size that the bubble attains is strongly dependent on the initial temperature distribution in the liquid which is unknown. The overall trend of the dynamics however proved to be rather robust with respect to the initial conditions of the system. Even though the model was able to reproduce the observed bubble size as a function of time, it is limited in the information it provides. In this chapter we study the same problem by solving the full governing equations with the numerical method of chapter 4. The full solution not only provides the bubble size but also its shape during the whole process, as well as the temperature and flow fields. Furthermore, the simulations take surface tension effects into account and the viscous dissipation need not be modeled but follows from solving for the flow field and as such it is treated more accurately. As performing the simulations with the exact experimental parameters takes extremely long computation times, and in view of the unknown initial temperature distribution, a direct comparison between simulation and experiment is not pursued here. Instead, we concentrate on capturing the fundamental physics as manifested in the qualitative behavior, and investigate the

effects of the initial temperature distribution on the quantitative results of the bubble dynamics.

6.2 Simulation setup

The experimental setup used for the study of a vapor bubble growing and collapsing a tube was discussed in detail in chapter 2. Here we discuss the setup for the simulations that were performed for this system. A schematic can be seen in figure 6.1.

We consider a tube with length L and diameter D, filled with liquid. In the experiments a laser pulse is focussed at the midpoint of the tube heating a small liquid region to a temperature close to the critical temperature. A vapor bubble nucleates and grows rapidly. As the bubble grows the vapor pressure and temperature decrease rapidly due to the work of expansion and condensation. Including the nucleation process in the numerical simulation is not possible because it depends on non-deterministic thermodynamic fluctuations. Instead, we start the computations from a spherical bubble with a size already comparable to the tube diameter, and an assumed temperature distribution in the liquid. The choice for the initial surface liquid temperature is based on the experimental observations of chapter 2, where it

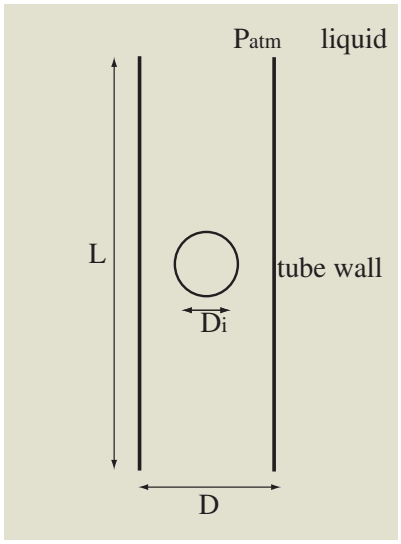

Figure 6.1: Sketch of the bubble in the micro tube situation

was seen that as the bubble has grown to a size comparable to the tube diameter the temperature had dropped to approximately 200 °C.

The tubes used in the experiments had a length of approximately 3 cm and an aspect ratio, defined as the ratio of length to diameter, in the range of $500-1000$. The bubbles however typically reached a maximum size of about $100\,\mu$m. As our numerical method solves the governing equations on uniform grids, i.e. $\Delta r = \Delta z$, performing the simulations using computational domains with the same length and aspect ratio as the experimental tubes requires extremely long computation time. In view of the fact that we are focussing on the qualitative aspects of the dynamics we perform the simulations of this system on computational domains with aspect ratio of 20

A schematic of the computational domain used for these simulations is shown in figure 6.2. The bubble is created at the midpoint of the axis of the tube which means that in addition to the axial symmetry the situation is symmetric about the tube midplane as well. We again take advantage of this in order to decrease the size of the computational domain by a factor of two. Symmetry conditions are imposed at the tube midplane. No slip conditions are imposed at the tube wall for the velocity. Furthermore, the bubble is not allowed to come into contact with the tube wall because our velocity extrapolation method requires valid liquid velocity values to work properly. Therefore, at computational nodes adjacent to the no-slip boundary the radial velocity component with which the bubble surface is advected is set to zero. As the radial velocity field near the tube wall is extremely small anyway, this restriction is of negligible influence. At the tube end the pressure is kept at the reference value, and the velocity field gradients normal to the computational boundary are set to zero in order to keep the flow field smooth.

During the whole growth and collapse process, the temperature only varies in the close neighborhood of the bubble. Thus the thermal domain can be kept relatively small compared to the momentum domain. The size of the thermal domain that is needed so that the temperature field at the top boundary remains undisturbed is determined by performing a quick, low resolution simulation to get a crude idea of the maximum bubble size attained. The temperature at the top boundary of the thermal domain is kept at a reference temperature T_∞. At the tube wall we consider two limiting cases, namely adiabatic and isothermal conditions.

To start the calculation an initial temperature distribution in the liquid needs to be provided. We initialize the temperature so that there is a thermal boundary layer in the liquid by means of a Gaussian distribution

$$T(r,z,0) = T_\infty + \Delta T \exp\left[-\left(\frac{|\mathbf{x}| - R_0}{\delta}\right]^2\right), \tag{6.1}$$

where $|\mathbf{x}| - R_0$ is the distance from the point $\mathbf{x}$ in the liquid to the bubble surface, ΔT is the temperature difference between the initial vapor temperature and T_∞ and δ is the thermal boundary layer thickness.

The governing equations are non-dimensionalized by introducing various scales for length, velocity, time and temperature. For the length scale we take the tube diameter D. A scale for the velocity is defined by means of a simple consideration in which the bubble pushes a liquid column of length L. Taking the initial overpressure as the force per unit area that pushes the liquid, an acceleration can be defined as $\Delta p/\rho L$. To define a velocity scale we multiply the acceleration by the length scale,

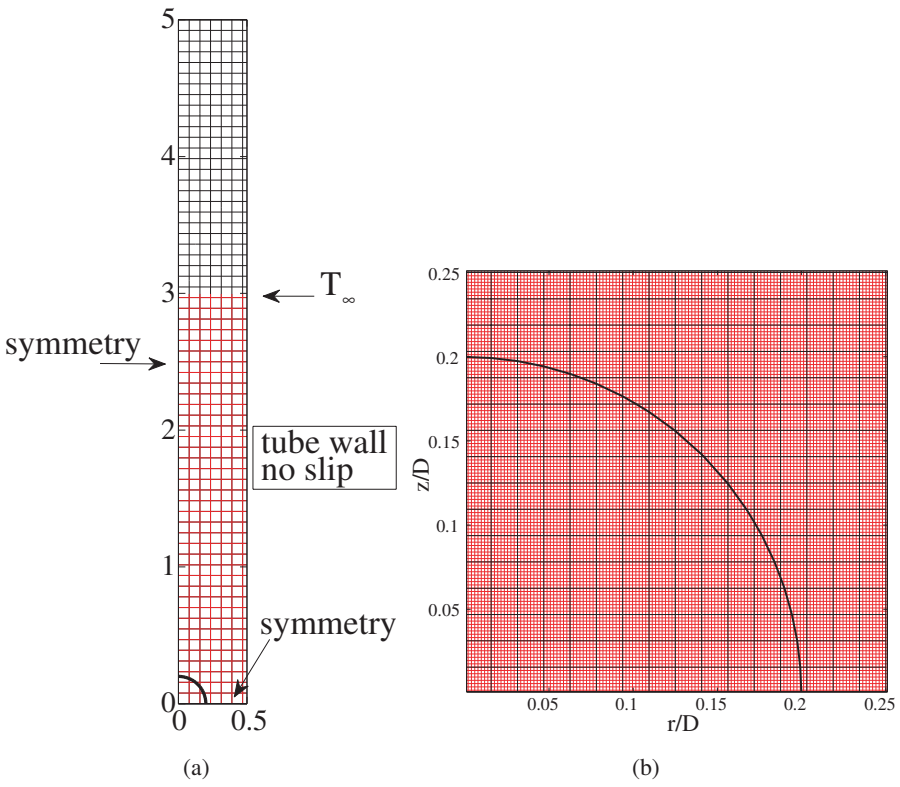

Figure 6.2: (a) Schematic of the computational domain used in the simulations. A few lines are shown of the momentum grid (black) and the thermal grid (red). The initial bubble is also shown as the black curve. (b) the actual momentum and thermal grid lines around the bubble. The thermal grid has a resolution 8 times higher than the momentum grid.

D, and take the square root:

$$V = \sqrt{\frac{\Delta p D}{\rho L}} = \sqrt{\frac{\Delta p}{\rho A}}, \tag{6.2}$$

where $A = L/D$ is the aspect ratio of the tube. A time scale is defined using the length and velocity scales:

$$t^\star = \frac{D}{V} = D\sqrt{\frac{\rho A}{\Delta p}} \tag{6.3}$$

The temperature is normalized as

$$\theta = \frac{T - T_\infty}{T_{sat}(p_\infty) - T_\infty}, \tag{6.4}$$

with $T_{sat}(p_\infty)$ the saturation temperature evaluated at the pressure at the tube ends. Using these scales Reynolds, Weber and Péclet numbers are defined in the usual way

$$Re = \frac{\rho V D}{\mu}, \qquad We = \frac{\rho V^2 D}{\sigma}, \qquad Pe = \frac{V D}{\alpha}. \tag{6.5}$$

Additionally the aspect ratio is a relevant nondimensional parameter, $A = L/D$, which as mentioned earlier is not taken the same as in experiment.

Due to the fact that the length of the tubes in the simulation is shorter than in the experiment, using the actual physical properties of water results in fairly large Re and Pe numbers. Large values of these non-dimensional numbers produce thin boundary layers, the resolution of which imposes a great burden on the computation. We therefore selected the liquid viscosity and thermal diffusivity so that the non-dimensional numbers are roughly the same as those resulting from the experimental values. The properties for the liquid were chosen as $\rho = 10^3\,\mathrm{kg/m^3}$, $\mu = 1.4 \times 10^{-3}\,\mathrm{kg/ms}$, $\sigma = 0.073\,\mathrm{N/m}$ and $\alpha = 8.5 \times 10^{-7}\,\mathrm{m^2/s}$. In addition to resulting in similar Re and Pe numbers between experiment and simulation, the Prandtl number is kept equal to that of water at saturation pressure and 100 °C, namely $Pr = 1.64$. The reference pressure at the tube end is taken to be atmospheric, $p_\infty = 101\,\mathrm{kPa}$ and the reference temperature at the top boundary of the thermal domain $T_\infty = 25\,^\circ\mathrm{C}$.

6.3 Bubble dynamics

We performed several simulations with varying parameters, all for a tube diameter of $50\,\mu\mathrm{m}$ with an aspect ratio $A = 20$. The bubble is initialized as a sphere with a diameter of $20\,\mu\mathrm{m}$.

We consider separately the limit cases of adiabatic and isothermal tube wall. The momentum grid spacing was $\Delta r/D = \Delta z/D = 0.0156$.

We define the size of the bubble as the distance from the center of the initial bubble to the intersection of the bubble wall and the axis of symmetry of the domain. The bubble velocity is calculated as the velocity of the bubble wall at the same point.

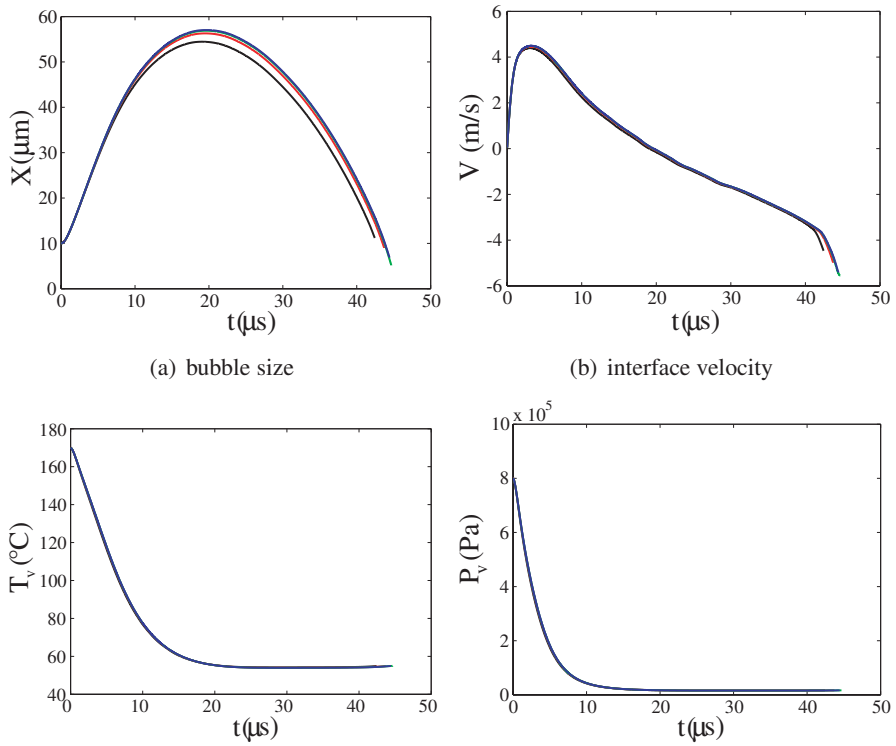

(a) bubble size (b) interface velocity

(c) vapor temperature (d) vapor pressure

Figure 6.3: Simulation results for various quantities upon refining the thermal grid. (black) $\Delta r_{therm}/\Delta r = 1/2$, (red) $\Delta r_{therm}/\Delta r = 1/4$, (green) $\Delta r_{therm}/\Delta r = 1/8$, (blue) $\Delta r_{therm}/\Delta r = 1/16$. The nondimension numbers for this simulation are $Re = 212$ and $Pe = 349.7$. Due to these moderate values the viscous and thermal boundary layers are relatively easy to resolve. Except for small variations in the bubble size the results for all thermal grid resolutions are nearly indistinguishable.

6.3.1 Reference case

We take as our reference case an initial thermal boundary layer thickness, $\delta = 0.75R_0$, with R_0 the initial bubble radius. The initial vapor temperature is 170 °C with a corresponding vapor pressure of 7.97×10^5 Pa. For this case the non-dimensional numbers are $Re = 212$, $We = 24.2$ and $Pe = 349.7$. The tube wall is treated as adiabatic.

Figure 6.3 shows the results of this simulation for the bubble size, interface velocity, vapor temperature and pressure as a function of time, for four different thermal grid resolutions. The thermal grid spacing is successively refined with $\Delta r_{therm}/\Delta r = 1/2\,1/4, 1/8, 1/16$. The corresponding results are indicated in the figure by the black, red, green and blue solid lines respectively. For this case, reaching grid independence does not require a very large refinement due to the moderate *Re* and *Pe* numbers. The results are indistinguishable apart from a small effect on the bubble size.

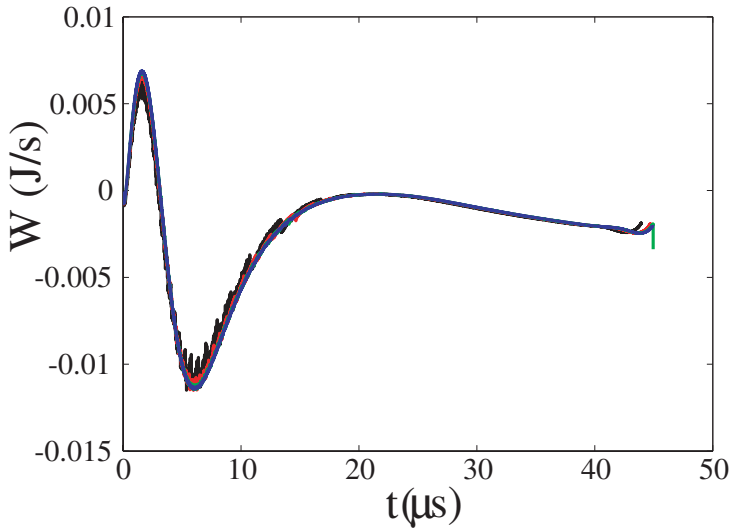

Figure 6.4: Total conductive energy flux at the interface, $\oint k\nabla T \cdot \mathbf{n}\,dS$ with S the bubble surface, is needed for determining the new vapor temperature. This particular quantity is very sensitive to the computation of the thermal gradients at the interface. Here the value of the integral is shown as a function in time for successively larger refinement of the thermal grid. black: $\Delta r_{therm}/\Delta r = 1/2$, red: $\Delta r_{therm}/\Delta r = 1/4$, green: $\Delta r_{therm}/\Delta r = 1/8$ and blue: $\Delta r_{therm}/\Delta r = 1/16$. For the low level refinement the thermal gradient computation exhibits some oscillations due to the discretization. Subsequent refinement decreases these oscillations until at the finest thermal grid no oscillations are noticeable.

The effect of the thermal grid refinement is seen more clearly from the calculation of the total heat flow into the liquid given by

$$\oint k\nabla T \cdot \mathbf{n}\, dS \tag{6.6}$$

where S is the bubble surface. this quantity depends very strongly on an accurate approximation of the thermal gradients, see figure 6.4. Due to the discretization and the moving interface there are some oscillations which decrease significantly upon refinement of the thermal grid. As the results differ only slightly upon refinement, all subsequent simulations are performed with $\Delta r_{therm} = \Delta r/2$ in order to minimize the needed computation time. The qualitative correspondence between experimental and simulation results becomes particularly clear when we plot the various quantities next to each other. The computed and measured results for the bubble size, interface velocity, vapor temperature and pressure as functions of time are shown in the left and right columns of figure 6.5, respectively. All qualitative aspects of the experimental data are reproduced by the numerical simulation. The initial bubble growth proceeds violently due to the large initial vapor pressure. The duration of this fast growth is short, however, as the vapor temperature and with it the pressure decrease quickly due to the work of expansion and condensation. After this initial phase the motion proceeds largely by inertia. The striking features, found in the experiments and also in the one dimensional model of chapter 2, namely that the bubble collapse proceeds more slowly than the growth is reproduced by the numerical method. Additionally, the fact that the vapor temperature at the final stages of the collapse phase is still far above the undisturbed liquid temperature is captured by the numerical simulation. The final vapor temperature depends on how efficiently the latent heat released by the condensation is transported through the thermal boundary layer. This will be discussed below.

The bubble lifetime resulting from the simulation is about a factor of 10 shorter than the experimental one. According to the scaling of the characteristic time shown in (6.3), this quantity is proportional to the square root of the aspect ratio, which is 27 times smaller than in the experiment. The difference between the two lifetimes is therefore in the ballpark that one could expect, once the uncertainties in the initial conditions and, in particular, the initial temperature distributions are kept in mind.

We can go further in reconciling the computational and experimental results if we use the simplified step-function pressure model of section 2.4.1 in chapter 2. In this model the bubble is approximated as a cylinder occupying the entire cross section of the tube. The growth of the bubble is initiated by applying a constant overpressure, Δp, for a certain amount of time, τ_{pulse}, after which the bubble pressure drops to the vapor pressure at the undisturbed temperature, $p_0(T = 25\,^{\circ}\mathrm{C}) \simeq 0$. In [56] this model

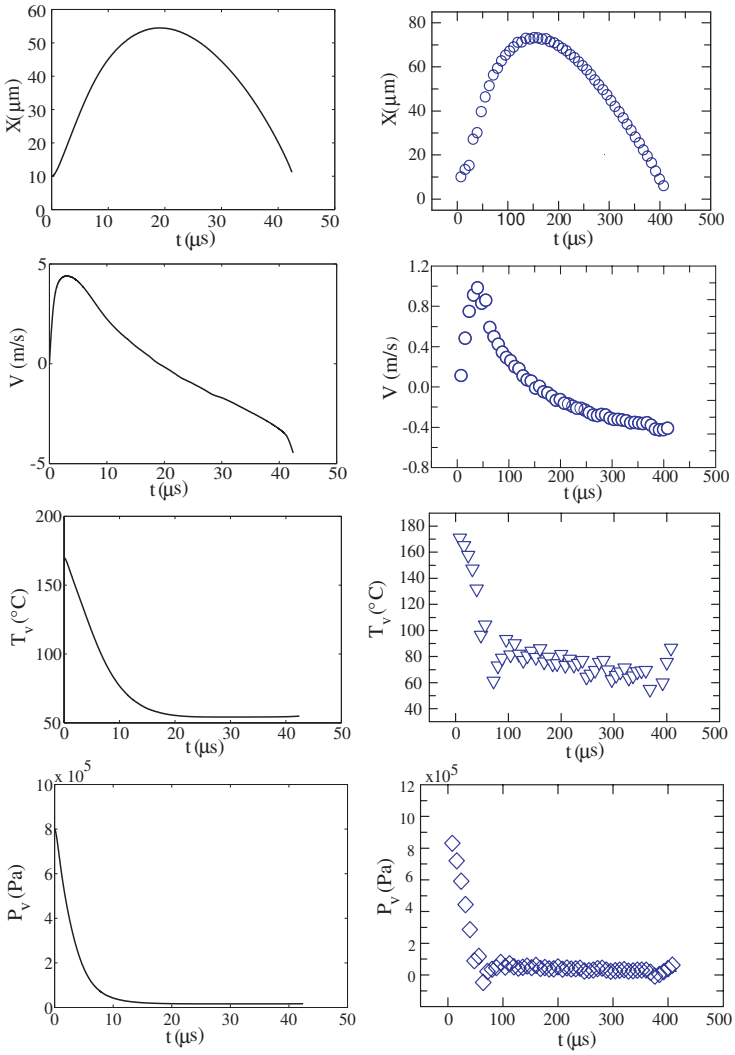

Figure 6.5: Comparison of the simulation result (left) and the experimental data (right). All qualitative features are reproduced by the numerical simulation. The rate of collapse is slower than the rate of growth. The velocity shows a sharp peak in the early stages of the growth as also seen in the experimental data. The simulation even captures the relatively high vapor temperature at the final stages of collapse. The bubble lifetime from simulation is an order of magnitude shorter than in experiment. A scaling argument for this is given in the text.

was further simplified by neglecting surface tension and viscosity and assuming the bubble surface to remain sufficiently far from the tube ends. In this way expressions can be derived for the maximum bubble volume V_{max} reached during the growth, and the bubble lifetime as

$$\frac{V_{max}}{\frac{1}{4}\pi D^2 L_{tube}} = \frac{\Delta p \tau_{pulse}}{p_\infty}\frac{V}{AD} \tag{6.7}$$

$$t_B \simeq \frac{2\Delta p \tau_{pulse}}{p_\infty - p_0}, \tag{6.8}$$

where V is the velocity scale as before. In our simulation the vapor pressure is not a step function as in this model. Therefore, in applying these expressions we equate $\Delta p \tau_{pulse}$ to the time integral of the vapor pressure, $\Delta p \tau_{pulse} = \int p_v \, dt$. With the above parameters, the estimate for the bubble lifetime is $t_B = 65.14\,\mu$s to be compared with the computed value of $45\,\mu$s. For the normalized volume there is a bigger difference, 0.194 vs. 0.071. The results of [56], who included viscous but not thermal effects, show that the (6.8) over-estimates the volume by about 50%. The remainder of the difference may be imputed to thermal effects and the way in which $\Delta p \tau_{pulse}$ is estimated. Be that as it may, the computational results are generally consistent with the simple estimates.

Figures 6.6 and 6.7 show the bubble shape, temperature field and velocity vectors at several instants during the whole process. The temperature field is shown in the meridian plane on the right of the symmetry axis and the velocity field on the one on the left. The velocity vectors are plotted every other grid cell. Figure 6.6 shows the growth phase. The initial configuration is shown in (a). The situation after $t = 0.7t^\star = 5.9\,\mu$s is shown in panel (b). The bubble has grown to a size comparable to the tube diameter and it starts to acquire a cylindrical shape with a rounded cap. As shown by the different temperature color bar, already at this early stage the vapor temperature has dropped by approximately 60 °C due to the work necessary to push the liquid and the very fast condensation of the vapor. The vapor pressure has dropped to almost atmospheric and the maximum velocity has already been reached. The rest of the motion is governed by inertia. The flow field is primarily directed in the axial direction and apart from the thin viscous boundary layer at the tube wall it is nearly uniform over the tube cross-section. In the early growth stages the thermal boundary layer is squeezed toward the wall and compressed.

Panel (c) shows the bubble at its maximum size at $t = 2.4t^\star = 20.2\,\mu$s. The bubble shape is a cylinder with a spherical cap. The part of the bubble adjacent to the tube wall is not completely straight however, but is slightly convex toward the axis of symmetry. This is due to the fact that the pressure along the tube wall varies. In the region of the spherical cap the pressure is lower than along the rest of the bubble

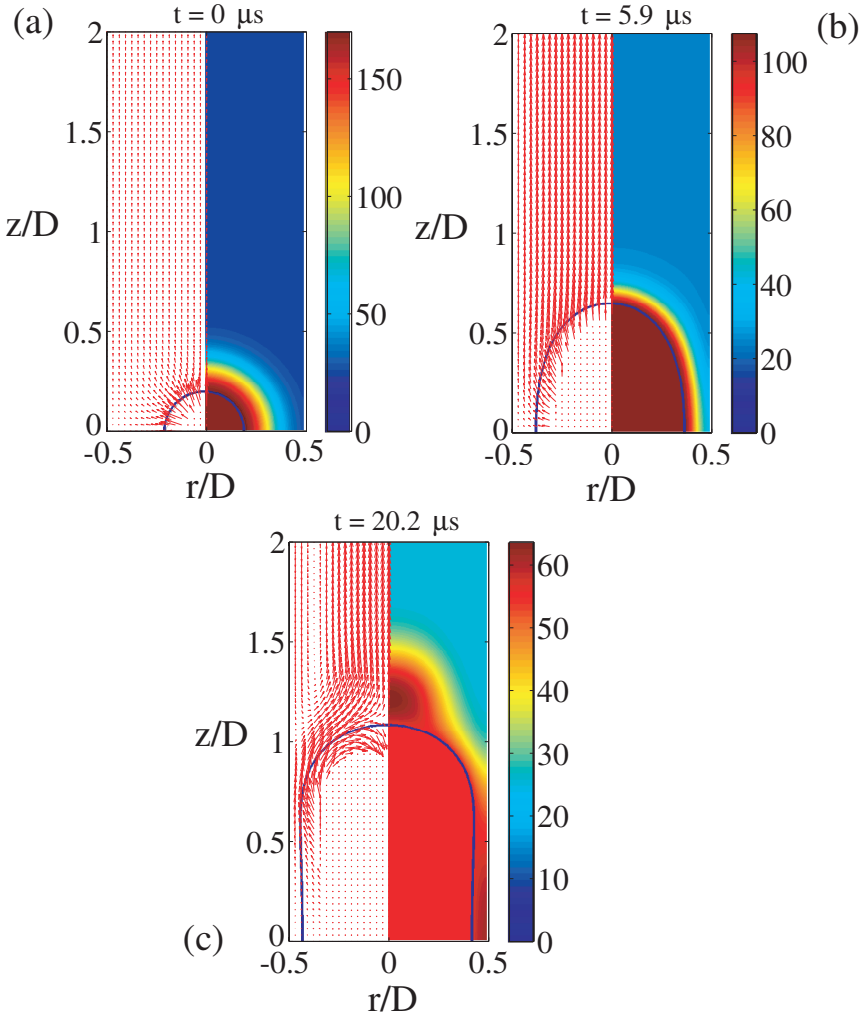

Figure 6.6: Several instants during the bubble growth. (a) Initial configuration. (b) The bubble has grown to a size comparable to the tube diameter. The vapor pressure has dropped to almost atmospheric. The rest of the motion proceeds by inertia. The liquid temperature has dropped significantly. This is mostly due to the fact that the initial energy content has been distributed over a much larger amount of mass through diffusion. (c) The bubble is at the end of its growth phase, the fluid flow is starting its reversal.

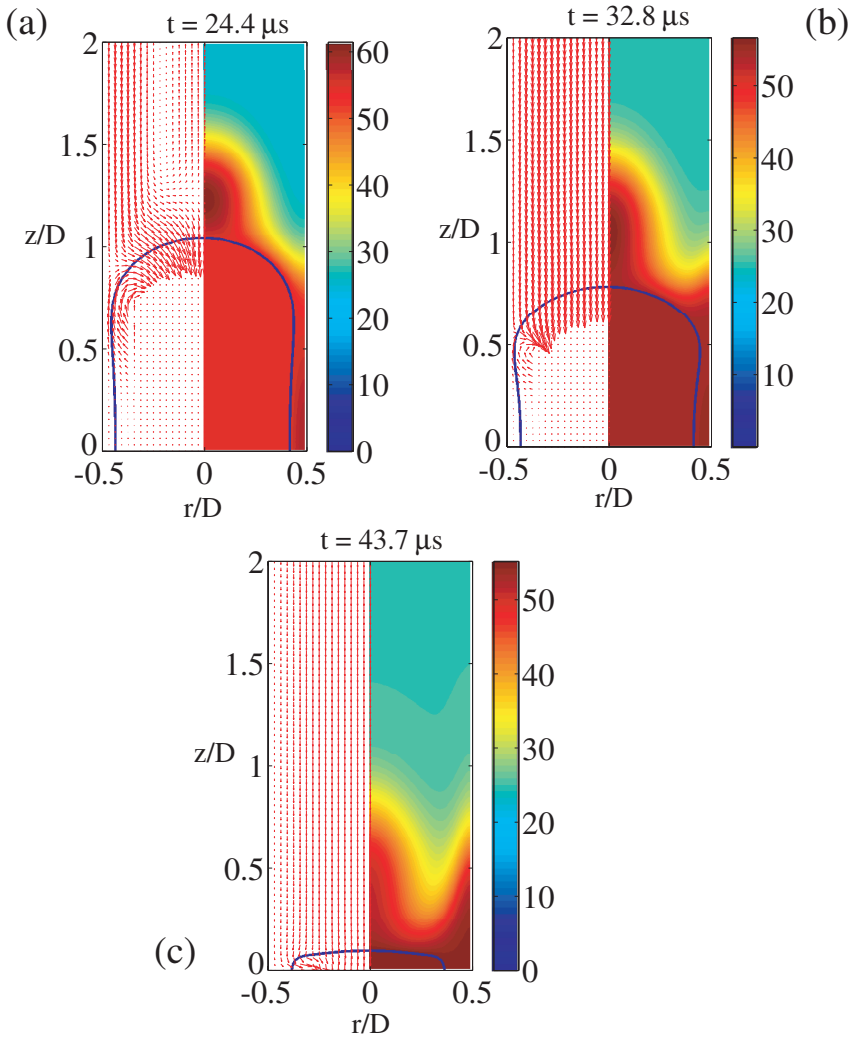

Figure 6.7: Several instants during the bubble growth and collapse. The bubble shape remains similar until the final stages. (a) The velocity field is almost completely reversed. (b) The start of a tongue of cold liquid is seen that separates the hotter fluid above the bubble and the tube wall. (c) The tongue of relatively cold liquid has grown. The bubble shape is similar to what was seen in the experiments of chapter 2

due both to the large velocity and the effect of surface tension. The velocity near the wall has already reversed while the liquid near the axis is still moving outward. This is the expected effect of the lower velocity reached by the liquid near the wall due to viscosity.

Also in panel (c) a small mass of liquid near the bubble cap hotter than the bubble by about 8 °C can be seen. This is in part a residue of the thermal energy associated with the initial Gaussian temperature distribution and in part due to the heat released by the early vapor condensation. At the time of this image, the vapor temperature has already decreased substantially and, therefore, the bubble is colder than this liquid region. It may also be noted that, due to the cylindrical geometry, the amount of liquid constituting this hot spot is actually smaller than it appears.

The collapse of the bubble is shown in figure 6.7 at times $t = 2.9t^\star = 24.4\ \mu$s, $t = 3.9t^\star = 32.8\ \mu$s and $t = 5.3t^\star = 43.7\mu$s. The bubble shape remains similar until the very late stages. The slight convexity toward the axis near the tube wall persists for most of the the whole collapse. The vapor temperature and pressure have reached their final values by now. In panel (b) one notes the beginning of a tongue of relatively cold liquid, shown by a greenish color and more evident in panel (c), that separates the warmer liquid near the axis noted before from the liquid near the wall in which the latent heat deposited has been trapped by the adiabatic wall condition.

Figure 6.8 gives a more quantitative picture of the liquid temperature by showing its distribution along the axis of symmetry at the same instants during growth (blue lines) and collapse (red lines) as in the previous figures. The region of warm fluid is clearly visible here in the blue and red lines at times $t = 20.2\ \mu$s and $t = 24.4\ \mu$s. During the collapse this region is smeared out due to diffusion and possibly some convection as seen from the red lines. One can see from this figure that the thermal domain has been chosen sufficiently large from the fact that the temperature is at the undisturbed value of $T_\infty = 25\,^\circ$C a distance of one tube diameter from the top of the thermal domain boundary. Several temperature profiles in the very early stages are shown in figure 6.9 where a temperature slightly higher than the vapor temperature can be noticed. This slight elevation actually forms a small ridge all around the bubble surface. This is the result of the initial Gaussian distribution at times such that the vapor temperature has already fallen noticeably while diffusion has not affected the liquid temperature due to the small gradients near the interface. As a confirmation of this origin we have noted that, if the initial temperature distribution is taken as a simple exponential, rather than a Gaussian, the effect disappears. The ridge persists only a very short time and quickly equilibrates with the vapor.

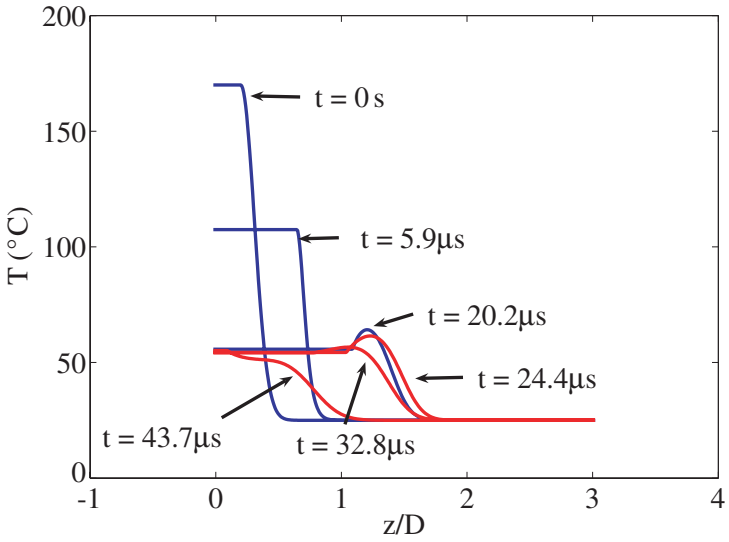

Figure 6.8: Temperature on the axis of symmetry at the same instants as figures 6.6 and 6.7. The blue lines are from the growth phase, the red lines from the collapse phase. The region with the relatively hot liquid above the bubble clearly visible.

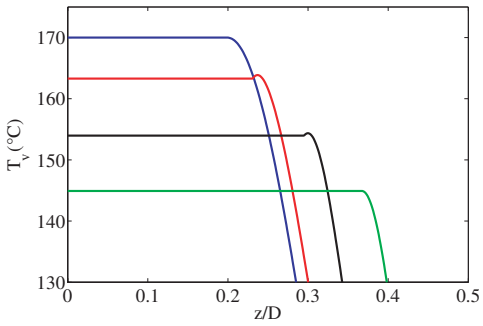

Figure 6.9: Close up view of the temperature on the axis of symmetry at the very early stages of growth. Blue: $t = 0$, red: $t = 0.84\mu$s ,black: $t = 1.68\mu$s green: $t = 2.52\mu$s. The liquid temperature very close to the interface is slightly higher than the vapor temperature. This is seen around the whole bubble forming a ridge. It quickly equilibrates again, as seen from the green line

6.3.2 Effect of the initial temperature distribution

As the initial temperature distribution is unknown, it is interesting to see how the the bubble behavior depends on the particular choice made for this quantity. The assumed Gaussian shape (Eq. (6.1)) is characterized by the surface temperature $T_\infty + \Delta T$ and thermal boundary layer thickness δ. We change both separately in order to investigate the effect they have on the overall dynamics, maintaining the adiabatic wall condition.

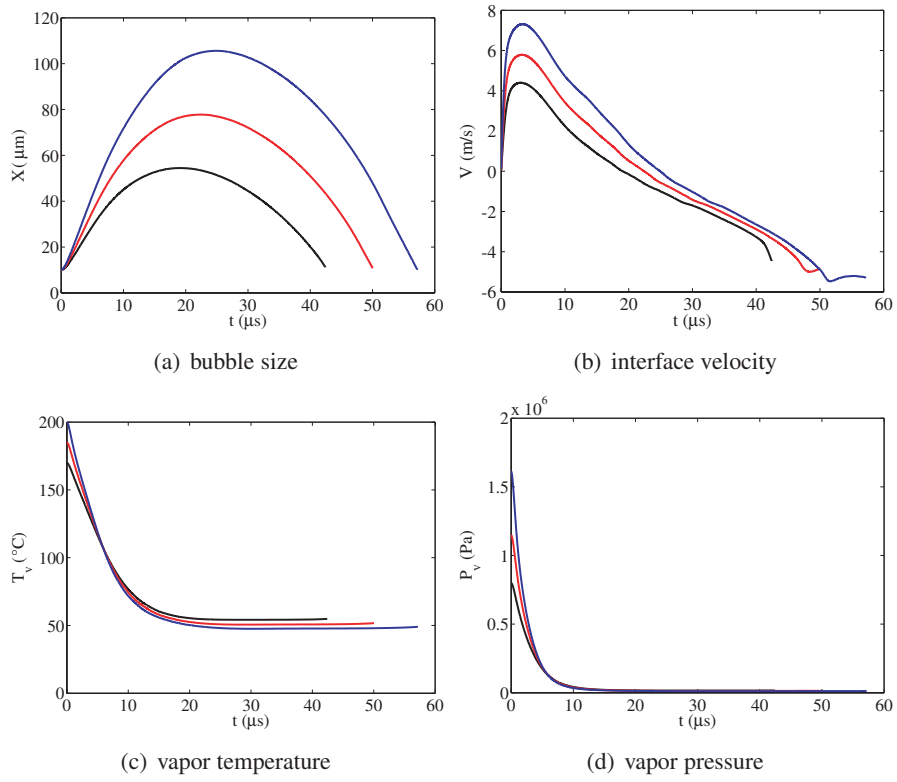

(a) bubble size (b) interface velocity

(c) vapor temperature (d) vapor pressure

Figure 6.10: simulation results for three different initial vapor temperatures, but same initial thermal boundary layer thickness, $\delta = 0.75R_0$. Black: $T_v(t=0) = 170\,^\circ$C, red: $T_v(t=0) = 185\,^\circ$C and blue: $T_v(t=0) = 200\,^\circ$C.

Varying initial vapor temperature

Starting the simulation with a higher initial vapor temperature, while keeping the initial thermal boundary layer width constant corresponds to creating the vapor bubble using an increasing laser pulse power. One therefore expects that the bubble reach a larger maximum size as the energy content of the system increases. This was already seen experimentally in figure 2.3. Two additional simulations with an initial vapor temperature of 185 °C and 200 °C respectively have been carried out, both with $\delta = 0.75R_0$. The results for the bubble size, velocity, vapor temperature and pressure versus time for these simulations, together with the previous results of $T_v(t = 0) = 170\,^{\circ}\mathrm{C}$ are shown in figure 6.10. The trend for the bubble size is the same as seen in the experimental data. The final values for the vapor temperature lie close together for the three cases even though the initial temperatures differ by as much as 30 °C. An interesting feature is the fact that, apart from the size, the bubble shapes are similar for all three cases, see figures 6.11. In [56] and [57] the growth and collapse of a bubble in a tube were also studied numerically without including the thermal aspects of the problem but assuming an impulsive initial over-pressure. In our simulation, which includes thermal effects, we find very similar bubble shapes for both the growth and collapse phases. This finding suggests that the bubble shape is determined by the fluid dynamics of the problem which is in large measure inertial after the initial pressure impulse. It is interesting to note that the bubble shape during collapse agrees with the experimental observations of chapter 2 as it remains oblate and the flow stays very nearly one dimensional or, at least, nearly parallel. The last shapes in panels (b) and (d) show oscillations most likely due to an insufficiently fine grid with attending curvature errors near the plane of symmetry.

Looking at the evolution of the bubble and the liquid temperature field for the simulation started with the highest initial temperature, shown in figure 6.12, we see the same behavior as for the reference case of figures 6.6 and 6.7, which has the lowest initial vapor temperature. The velocity field is not shown because it is similar to the one shown previously. The compression of the thermal boundary layer against the wall is seen in the center figure of the upper panel where the situation at 11.8 μs is shown. The vapor temperature at this point has dropped significantly to approximately 70 °C. The right figure of the upper panel, depicting the situation at 24.4 μs is where the bubble has attained its maximum extension and starts to collapse. Here again a region of relatively high temperature fluid is seen above. The lower panel shows the collapse process. Again, the bubble shapes and temperature field are similar to the previous ones except that the colder liquid tongue penetrates deeper. As the bubble has grown to a much larger size, during the collapse the temperature has has more time to diffuse resulting in a greater smearing. Notice that the thermal domain

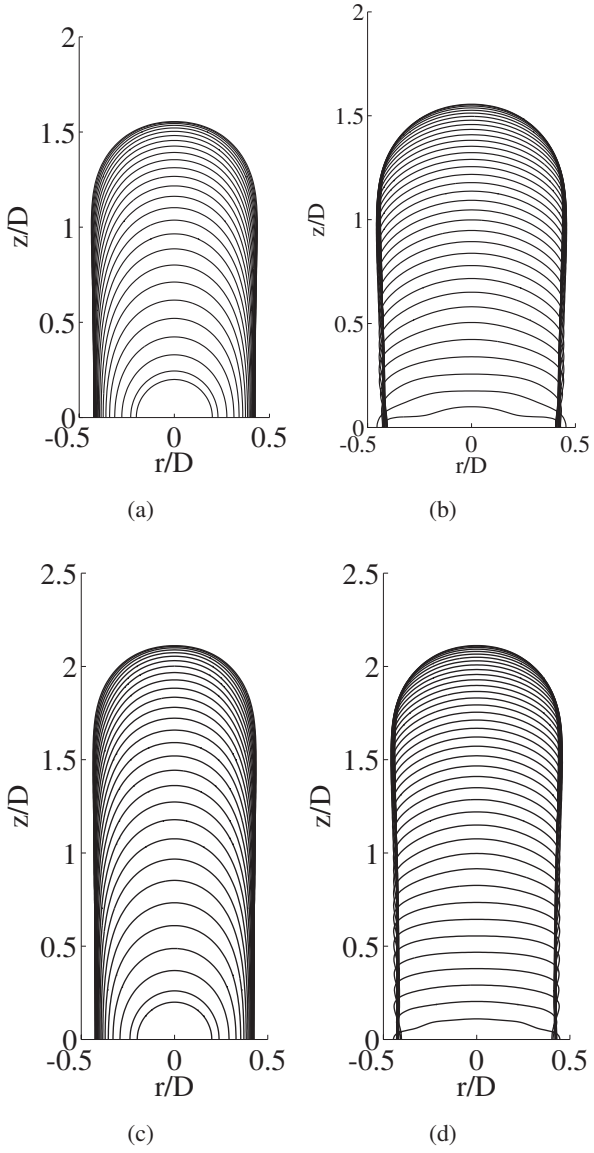

Figure 6.11: bubble shape during growth (a) and collapse (b) for initial vapor temperature of 185 °C. bubble shape during growth (c) and collapse (d) for initial vapor temperature of 200 °C.The time between successive curves is $0.1t^{\star}$ corresponding to 0.84μs.

size has been increased to four times the tube diameter in order for the temperature field to remain undisturbed near the top boundary.

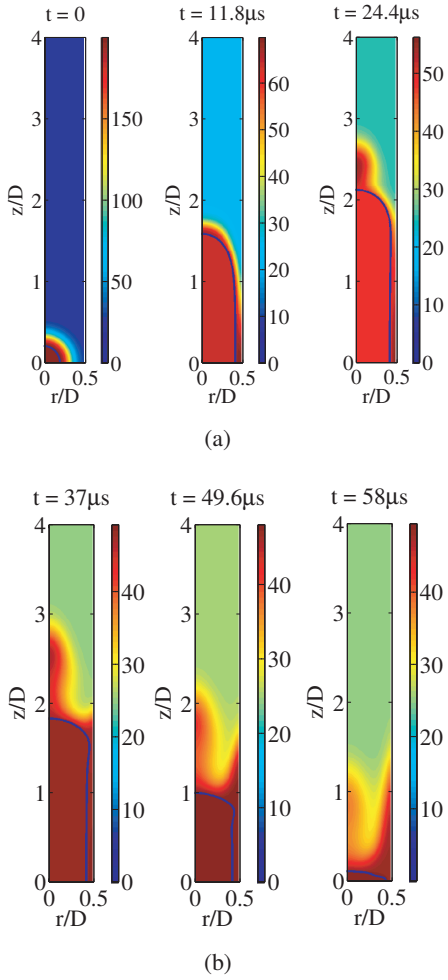

Figure 6.12: Temperature field and bubble interface for initial temperature field with $T_v(t = 0) = 200\,^{\circ}\mathrm{C}$ (a): growth phase. (b): collapse phase. The growth phase is very similar to the results from initial vapor temperature $T_v(t = 0) = 170\,^{\circ}\mathrm{C}$. At the end of the growth phase a region with high temperature fluid is located above the bubble. The collapse phase results in a more pronounced tongue of colder liquid.

Varying initial thermal boundary layer thickness

Keeping the same initial vapor temperature, but changing the initial thermal boundary layer thickness imparts a smaller initial energy to the liquid and also has a large effect on the bubble dynamics. Figure 6.13 shows the result of a simulations done with $\delta = 0.75R_0$, and $\delta = 0.375R_0$, while the initial vapor temperature was $T_v(t = 0) = 170\,^{\circ}\mathrm{C}$ as in the reference case. As expected, the maximum size reached with the thin thermal boundary layer is much smaller. The vapor temperature decreases much more quickly and with it the pressure so that the growth phase is easily stopped. This

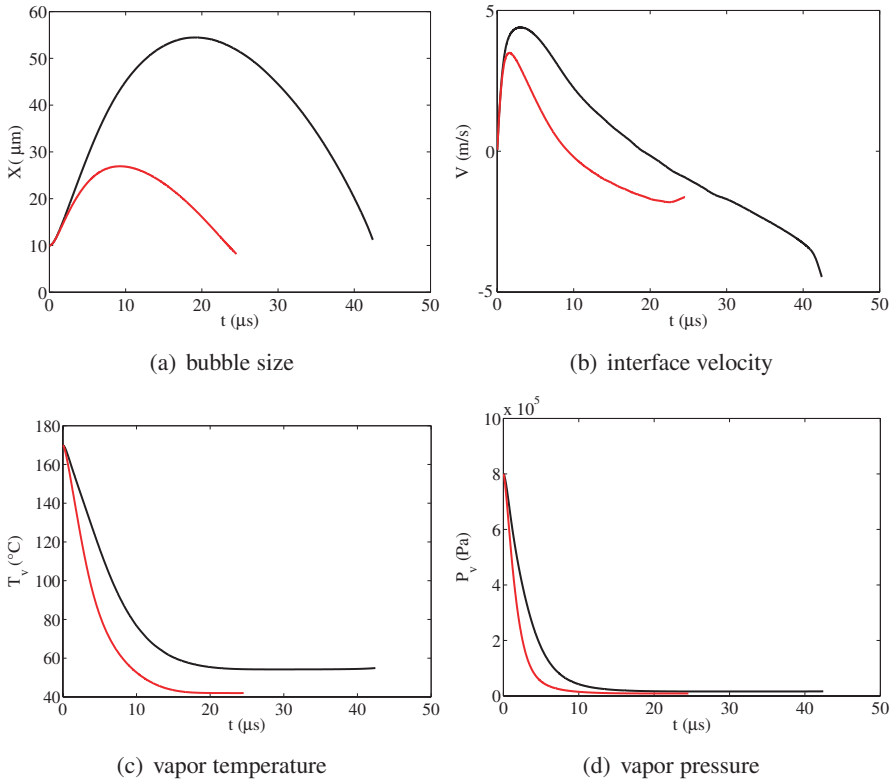

(a) bubble size (b) interface velocity

(c) vapor temperature (d) vapor pressure

Figure 6.13: The effect of varying the initial thermal boundary layer thickness. The black lines are the results for the thick initial boundary layer of $\delta = 0.75R_0$ while the red lines result from $\delta = 0.375R_0$. Clearly the bubble dynamics are sensitive to the particular choice of thermal boundary thickness. This strong dependency was also seen in the one dimensional model of chapter 2.

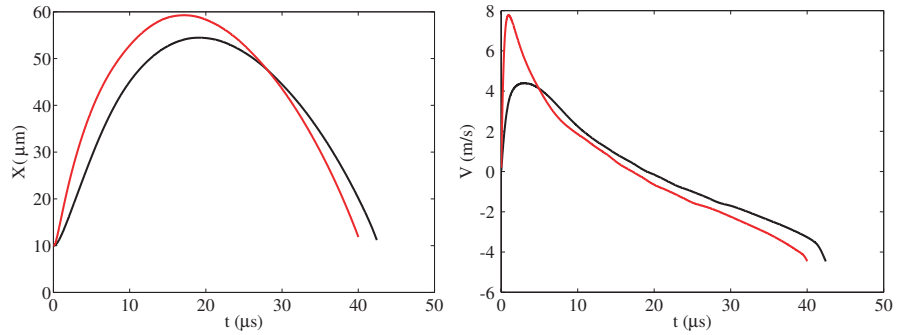

(a) bubble size

(b) interface velocity

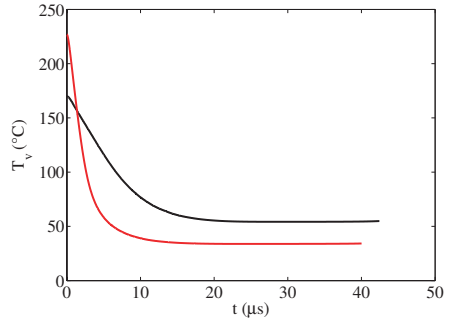

(c) vapor temperature

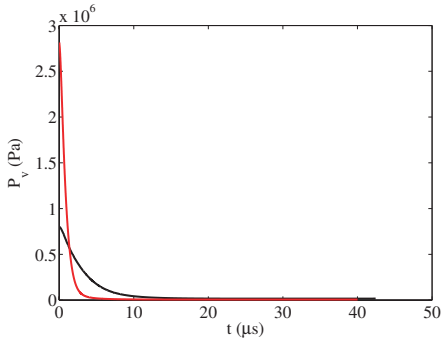

(d) vapor pressure

Figure 6.14: Results for different initial temperature distributions, but approximately equal energy content. The black lines are the results for $T_v(t=0) = 170\,^{\circ}\mathrm{C}$, $\delta = 0.75R_0$. The red lines are the results for $T_v(t=0) = 227\,^{\circ}\mathrm{C}$, $\delta = 0.22R_0$. The results for the bubble size are comparable, but the other quantities are markedly different.

strong dependency was also present in the one-dimensional model, see figure 2.8 of chapter 2. The final vapor temperature for the thin initial boundary layer is now 42 °C, which is 12 °C lower than that resulting from the thicker initial layer. Since the heated layer is much thinner, the latent heat released by the condensing vapor can be conducted away from the bubble surface more efficiently.

In order to isolate this effect we compare in figure 6.14 the results of the reference simulation with those of another one with a thinner initial layer, $\delta = 0.22R_0$, but a higher vapor temperature, $T_v(t=0) = 227\,^{\circ}\mathrm{C}$, adjusted so as to result in a comparable bubble size. In the figure the red lines are the results of this latter simulation while the black lines show the results of the previous simulation with $T_v(t=0) = 170\,^{\circ}\mathrm{C}$

and $\delta = 0.75R_0$. The maximum bubble sizes and the bubble lifetime are comparable. Nevertheless there are large differences in the other quantities. The acceleration for the thin boundary layer case is much larger in the early growth phase resulting in a peak for the velocity that is much more pronounced. The temperature and pressure decrease much faster due to the work that is done in putting the liquid column in motion. A large difference of approximately 20 °C is seen between the final vapor temperatures. The latent heat that is released due to condensation is carried away through the thin thermal boundary layer more effectively. More energy is transported into the liquid, away from the immediate neighborhood of the bubble, so that a lower temperature is reached.

Exponential initial temperature distribution

We have seen that the qualitative behavior of the system is relatively robust with respect to the choice of initial temperature condition. However, all the results shown were for simulations started from a Gaussian distribution. In order to investigate how the dynamics depend on this particular choice we have performed additional

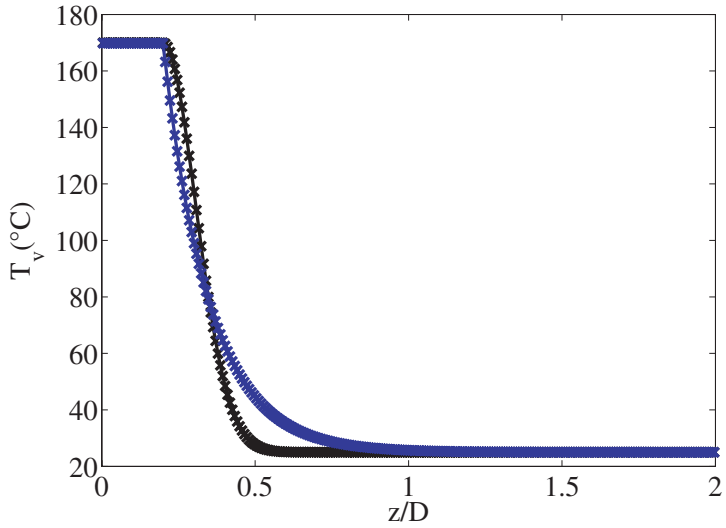

Figure 6.15: Temperature profile along the axis for the Gaussian distribution (black) and the exponential distribution (blue).

simulations with an initial temperature field given by a simple exponential:

$$T(r,z,0) = T_\infty + \Delta T \exp\left[-\left(\frac{|\mathbf{x}| - R_0}{\delta}\right)\right]. \tag{6.9}$$

Also in this case the temperature field is characterized by the initial difference between the vapor temperature and T_∞ and the thermal boundary layer thickness δ. Figure 6.15 shows both the Gaussian (black) and exponential (blue) initial temperature profile along the axis of symmetry for $T_v(t=0) = 170\,^\circ\mathrm{C}$ and $\delta = 0.75R_0$. The resulting temperature profiles differ qualitatively as the exponential function shows large gradients near the interface, facilitating heat conduction, but extends further

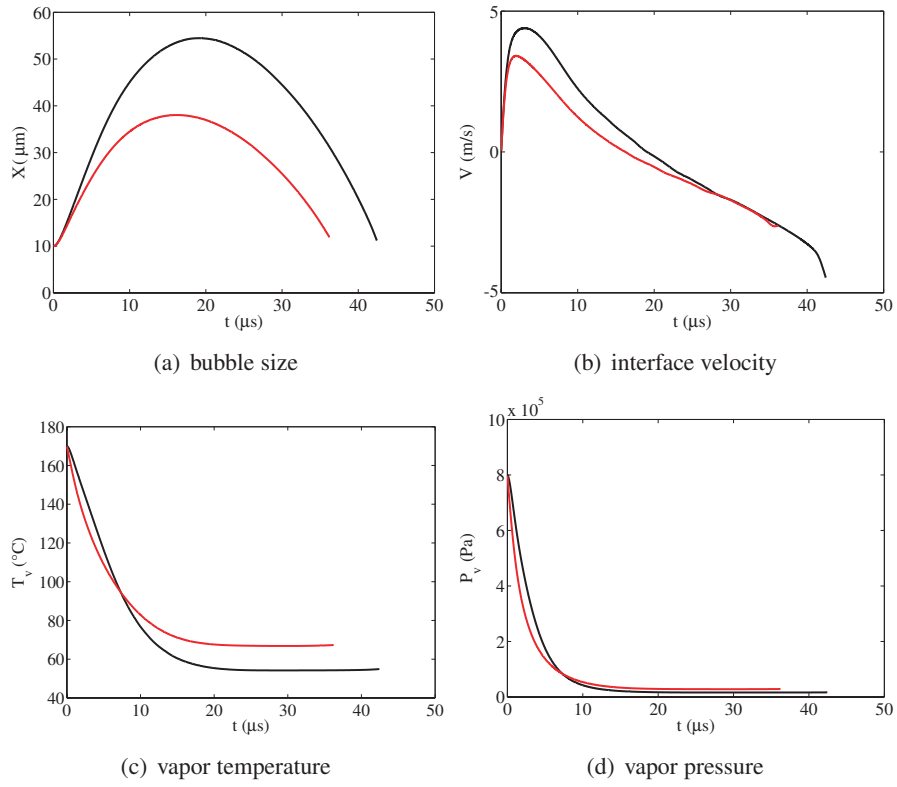

(a) bubble size (b) interface velocity

(c) vapor temperature (d) vapor pressure

Figure 6.16: Simulation results for two different type of initial liquid temperature distributions. Black: initial distribution is given by a Gaussian profile. Red: initial distribution given by an exponential profile. Both are initialized with $T_v(t=0) = 170\,^\circ\mathrm{C}$ and $\delta = 0.7R_0$, resulting in markedly different temperature fields as shown in figure 6.15.

into the liquid. Therefore it is not at all obvious a priori whether the trends of the dynamics we have seen previously will be recovered with the new initial condition.

The results of a simulation carried out with the initial liquid temperature field given by the exponential function with $T_v(t=0) = 170\,^{\circ}\mathrm{C}$ and $\delta = 0.75R_0$ are shown in figure 6.16 together with the results of the previous Gaussian distribution with the same parameters. Clearly, the choice of initial conditions affects the quantitative behavior, which was to be expected. However, the trend of the dynamics does not

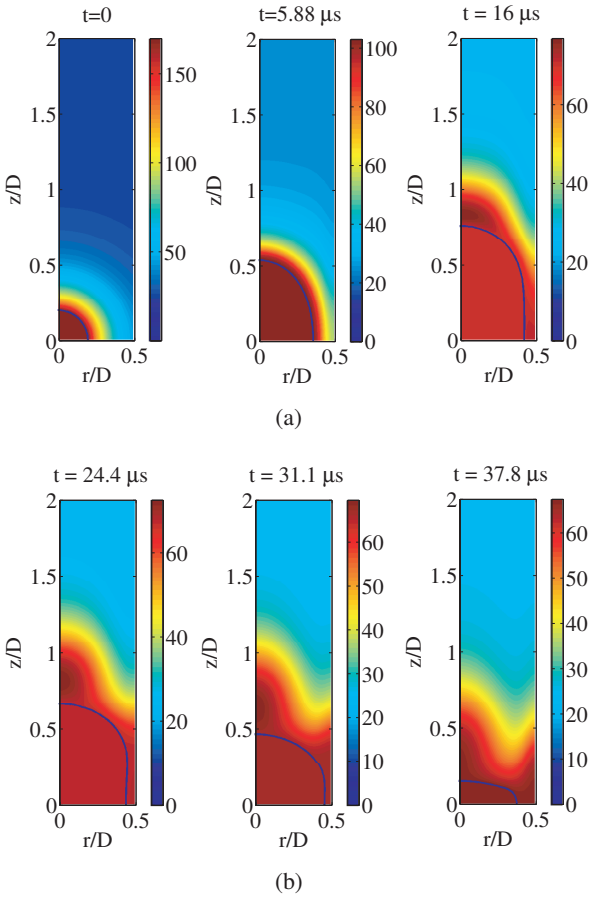

Figure 6.17: Temperature field for several instants during growth and collapse of the vapor bubble for the exponential initial condition. Both temperature field as bubble shape are qualitatively the similar to those resulting from the Gaussian initial condition.

seem to depend on the particular choice of initial condition. All qualitative aspects are present: the collapse proceeds more slowly than the growth, the interface velocity peaks early in the growth phase and the vapor temperature remains high during the final stages of collapse. The maximum bubble size for the exponential case is smaller due to the large gradients of the initial distribution that result in a faster decrease of the vapor temperature. The temperature fields during growth and collapse are shown in figure 6.17 and are seen to be very similar to the Gaussian case.

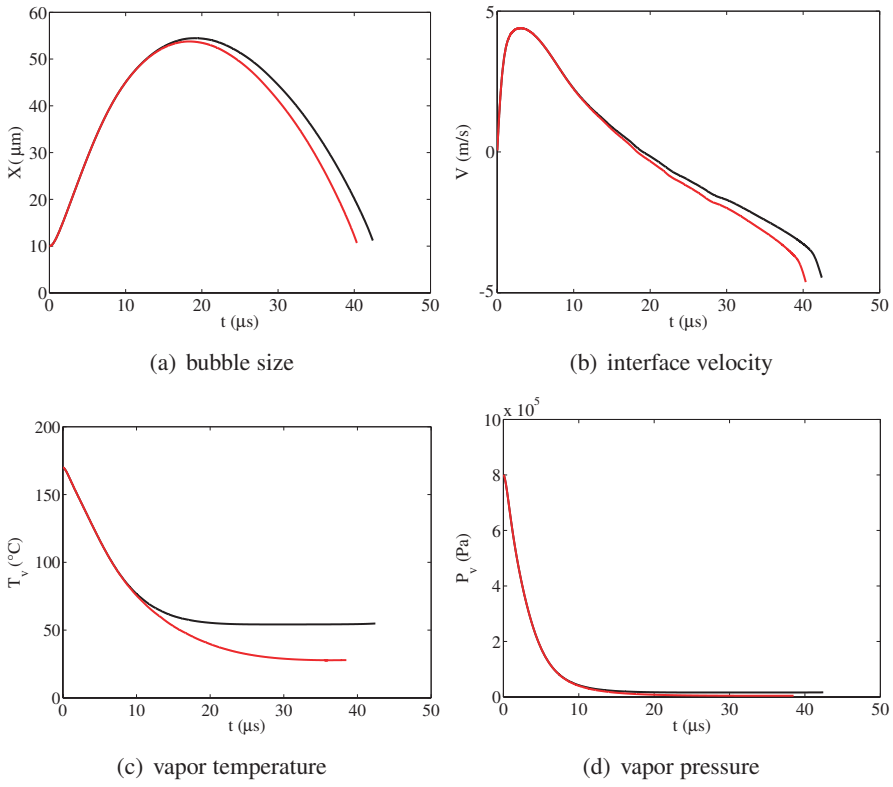

(a) bubble size (b) interface velocity

(c) vapor temperature (d) vapor pressure

Figure 6.18: (black): Adiabatic tube wall. (red) Isothermal tube wall. A large difference is seen in the final vapor temperature, due to the large loss of thermal energy through the tube wall. The dynamics however are not affected strongly, since it is largely proceeding by inertia.

6.3.3 Isothermal tube wall

All simulations shown so far have been performed with an adiabatic tube wall, preventing energy leaking from the system. The other limiting case is the isothermal condition, which we study returning to an adiabatic wall.

One would expect the bubble to reach a smaller maximum size as energy is leaking from the system. However, this is not the case. Figure 6.18 shows the results for the adiabatic condition in black and the isothermal condition in red. All other parameters are the same. The initial temperature distribution is given by $T_v(t=0) = 170\ ^\circ\mathrm{C}$ and $\delta = 0.75R_0$. The figure shows that the type of boundary condition has practically no effect on the growth phase. The reason for this is that all the work done in bringing the system in motion is expended before the bubble has reached the tube wall so that the thermal energy has had no time to diffuse out of the system. When the bubble has grown to occupy the tube a difference becomes noticeable. Due to the energy loss at the tube wall in the isothermal case the vapor temperature decreases to a lower value, thus creating a larger pressure differential in the tube that drives the collapse at a faster rate. The bubble shape, temperature and flow field during the growth and collapse for the isothermal case are shown in figures 6.19 and 6.20 respectively at the same time instants as for the adiabatic case. During the growth phase the temperature field is quite similar to that for the adiabatic condition. Panels (a) and (b) cannot even be distinguished from the adiabatic case. The difference starts to be noticeable in panel (c). At this stage there is a liquid layer between the bubble and tube wall where the thermal energy is lost due to conduction. The region of hotter liquid above the bubble, however, is also present here. The collapse phase is markedly different. All the hot fluid is located above the bubble, while the liquid at the tube wall is at a lower temperature.

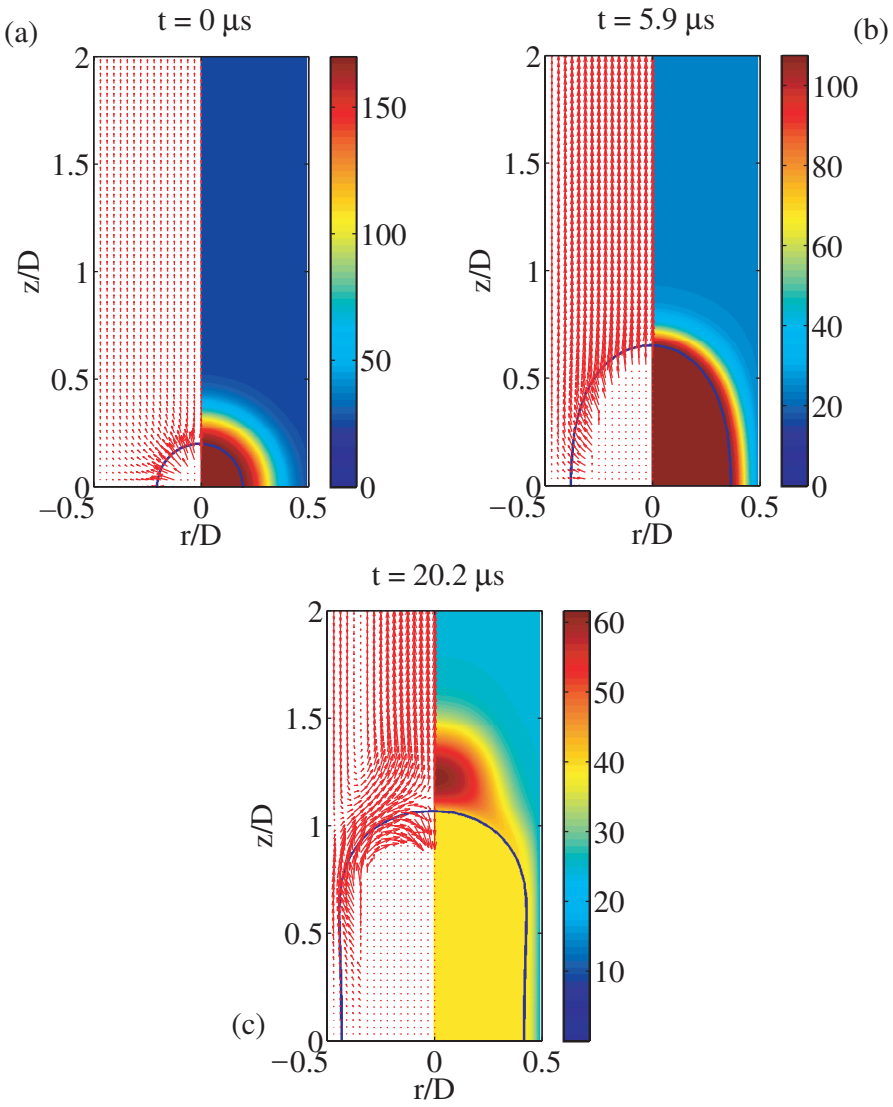

Figure 6.19: Several instants during the bubble growth. (a) Initial configuration. (b) At this stage the results are indistinguishable from the adiabatic case (figure 6.6) because the temperature at the wall has not changed noticeably. (c) Here the effect of the type of boundary is seen. The hot liquid layer that was seen between the bubble and the tube wall for the adiabatic tube is not seen here as the energy is diffused through the tube wall. This region remains therefore relatively cool.

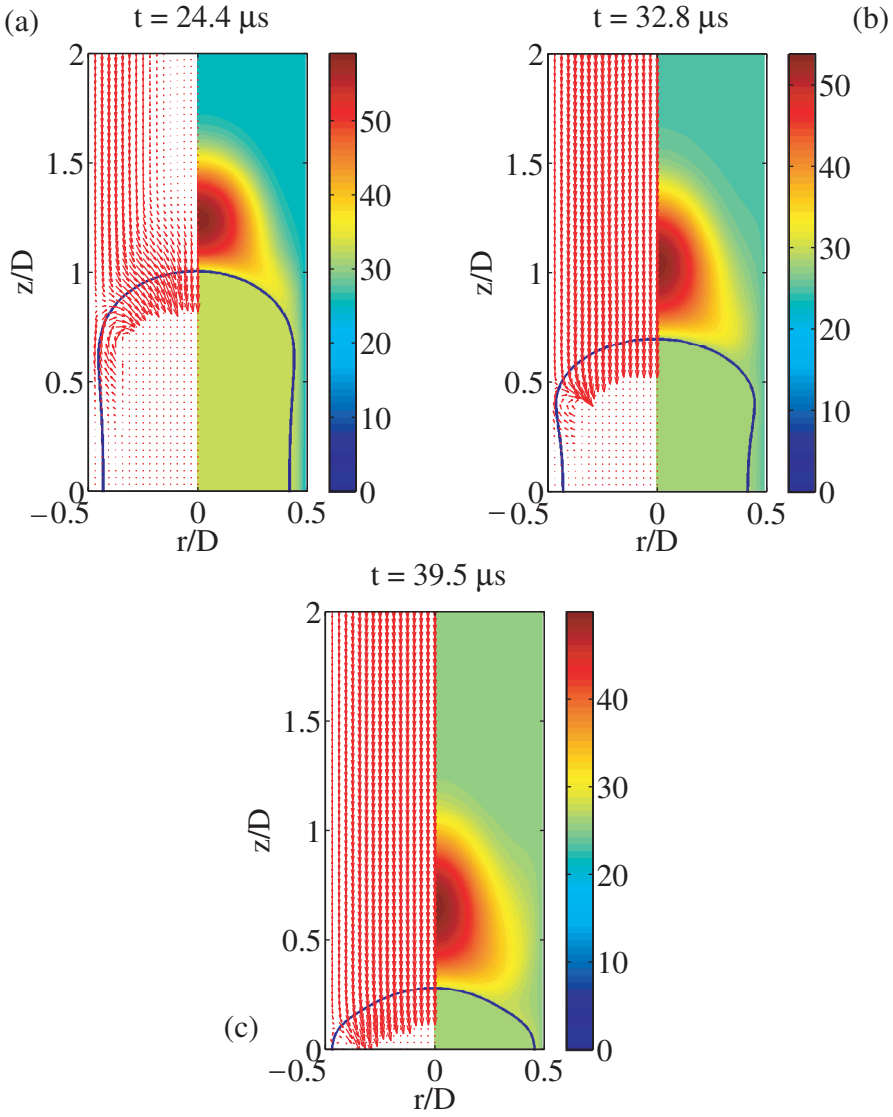

Figure 6.20: Several instants during the bubble collapse. The collapse looks markedly different from the adiabatic case. All the hotter liquid is located above the bubble. Near the tube wall there is only cooler liquid. The bubble shapes however are not affected by the change in boundary conditions.

6.4 Conclusions

We used our numerical method for the simulation of a vapor bubble growing and collapsing in a tube. Due to computation time limitations, in the simulation it was necessary to take the tube length much shorter than in the experiments of chapter 2. For this reason a direct comparison with experimental data is not made. Nevertheless the trends of the dynamics found in the experiment are reproduced by the numerical method and the predictions of the simplified scaling arguments are supported by the results. The behavior of the bubble is characterized by an initially large acceleration due to the large vapor pressure. The vapor temperature and pressure quickly decrease however because of the work done in bringing the liquid into motion. The growth proceeds from this point on essentially by inertia.

For starting a simulation an initial temperature distribution must be specified. As this is an unknown quantity we considered both Gaussian and exponential distributions and investigated the dependence of the dynamics on the particular shape of the initial temperature field. The initial vapor temperature and thermal boundary layer were varied both separately as well as simultaneously. In this way the driving force for the bubble growth was varied as well as the liquid temperature gradients at the bubble interface. We found that the thickness of the initial thermal boundary layer strongly affects the dynamics as well as the final values of the vapor temperature. The maximum bubble size that is attained as well as the final vapor temperature decrease considerably when the initial thermal boundary layer is chosen to be thin. This is due to the efficient transport of energy that is released by the bubble into the liquid through the boundary layer. The vapor temperature and with it the pressure decrease much faster as a result leaving less energy to propel the bubble growth.

7

Vapor bubble dynamics between parallel circular discs*

7.1 Introduction

In the previous chapter the vapor bubble was confined within a cylindrical micro-tube. The dynamics resulting from this confinement showed a clear asymmetry in the processes of growth and collapse of the bubble. The bubble shape however was seen to remain qualitatively the same during the whole process, namely cylindrical with spherical caps. A second type of confinement that we will consider in this chapter is that provided by two parallel discs. The dynamics of this system is fundamentally different from the tube case due to the radial flow, the large gradients of which affect the bubble shape in a qualitatively different manner. We study this system by means of a simplified theory and the numerical method of chapter 4 and we compare with experiment.

7.2 Experimental setup and results

The experimental apparatus used for the study of this case is similar to that used for the tube, figure 2.1; a schematic view is shown in figure 7.1. The bubble is

*The Experimental data presented in this chapter are entirely due to Chao Sun.

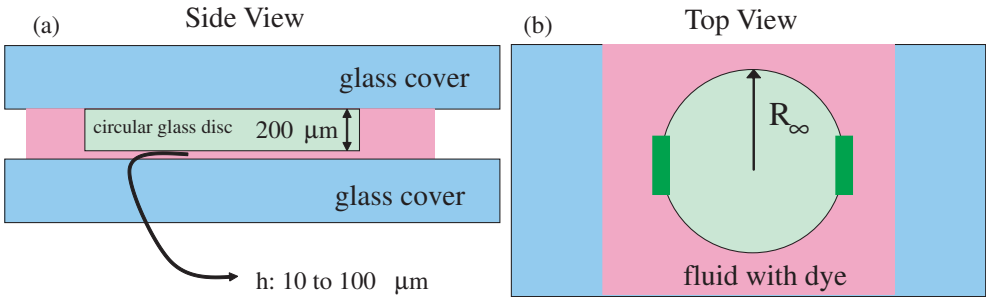

Figure 7.1: Schematic view for the setup used for the study of the vapor bubble dynamics. A circular glass disc is glued on the top glass cover in order to have a well defined region. The distance between the glass plates can be varied from $10\,\mu$m to 100μm.

generated in the thin gap between a 7.5 mm-radius glass disc (light green in the figure) attached to a rectangular glass plate, and an equal plate parallel to it. A solution of water and red food dye fills the space between the plates. The gap between the glass plate and the disc is varied between 10 and 100 μm by means of spacers. The purpose of the glass disc was to provide a well defined geometry for the experiment. It was not possible to glue a similar disc on the lower plate because the glue would hamper the transmission of light making it impossible to view the bubble as it evolves. The laser pulse energies used for this setup are the same as those used for the tube configuration, ranging from $3.48\,\mu$J to $19.54\,\mu$J.

Some representative frames taken during the evolution of the vapor bubble are shown in figures 7.2 for a distance between plates of $h = 10\,\mu$m and $h = 100\,\mu$m respectively. The top row in each figure shows the growth phase, while the bottom row shows the collapse. Both figures show a rich structure in the light intensity: bright and dark rings are clearly distinguishable, caused by multiple refractions at the vapor/liquid interfaces. The structures however are quite different for the two gap heights. For the small gap very thin bright and dark rings are seen at the bubble rim during both the growth and collapse phase. For the larger gap height the same is seen in the growth phase, though perhaps a bit less clearly because of the increased absorption of light. During the collapse however a broad dark ring is formed at the bubble rim. As these intensity structures are the result of refraction of light at the vapor-liquid interfaces, they contain information about the bubble shape. We will come back to this in the final section of this chapter. The experimental results for the bubble size, extracted from image analysis, for four gap heights and various laser pulse energies are shown in figure 7.3. The dynamics are qualitatively quite different

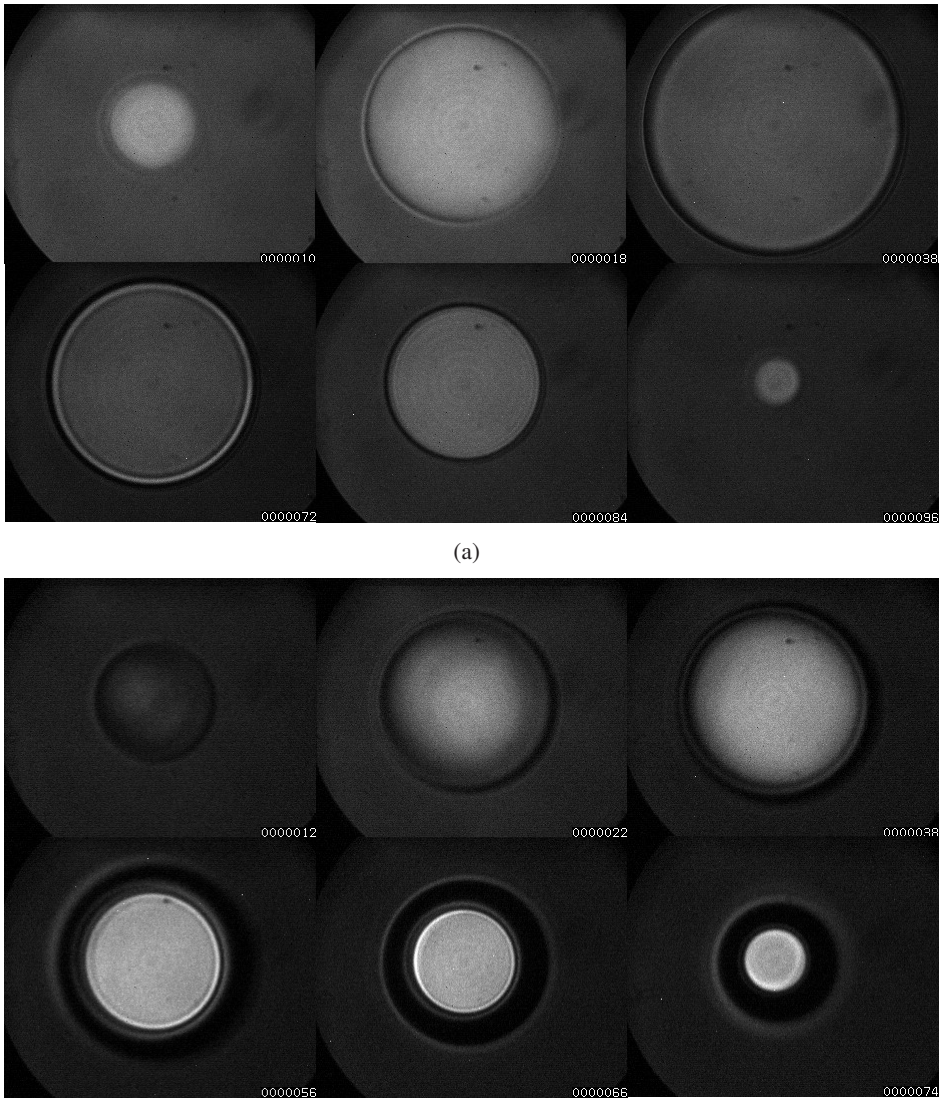

Figure 7.2: Representative frames showing the bubble growth and collapse. (a) Gap height $h = 10\,\mu$m. (b) Gap height $h = 100\,\mu$m. In each panel, the top row of frames are from the growth and the bottom row from the collapse of the bubble. The laser pulse energy for both experiments was $19.53\,\mu$J.

from the tube geometry. The marked difference between the duration of the growth and collapse phases present in the tube case is much less pronounced for the present geometry.

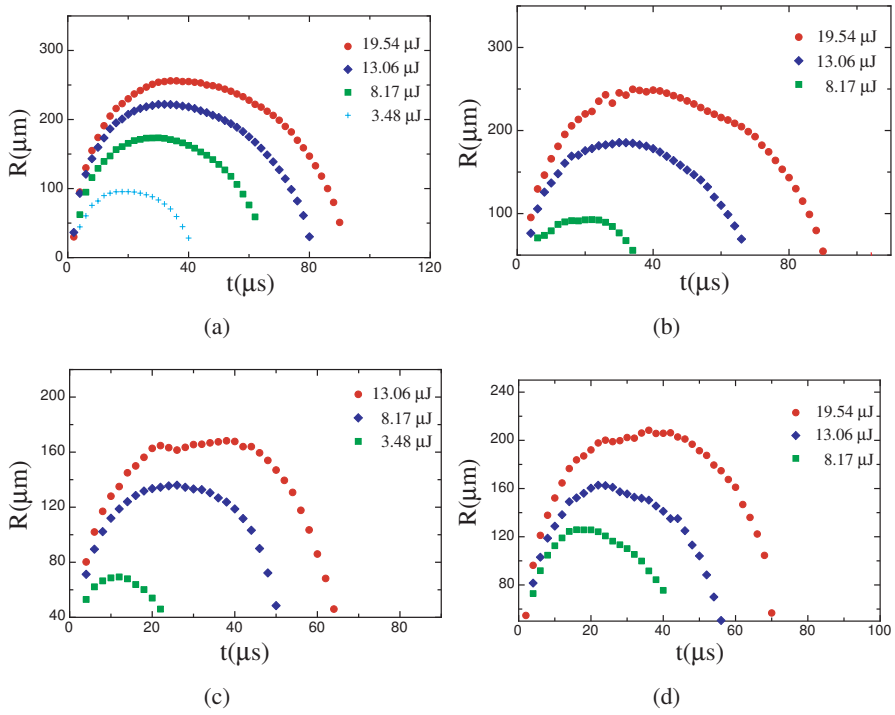

Figure 7.3: bubble radius vs time varying the laser pulse energy for four different gap heights: (a) $h = 10\,\mu$m, (b) $h = 20\,\mu$m, (c) $h = 50\,\mu$m and (d) $h = 100\,\mu$m

In the following section we study this system by developing a model in the same spirit as was done for the tube case. Subsequently, the numerical method will be used to simulate the system.

7.3 Cylindrical Rayleigh-Plesset model

7.3.1 Mechanical effects

We neglect the very first stages of the bubble growth from inception to a radius of the order of the gap height and model it as a flat cylindrical cavity, with a radius R and height h, within a fluid which extends to a distance R_∞ from the axis of symmetry.

	Energy (μJ)	$R_0(\mu\text{m})$	V_0 (m/s)
$h = 10\,\mu\text{m}$	19.54	95.40	18.97
	13.06	93.09	15.43
	8.17	62.38	19.23
	3.48	44.32	9.69
$h = 20\,\mu\text{m}$	19.54	96.59	16.69
	13.06	76.76	16.73
	8.17	49.06	10.33
$h = 50\,\mu\text{m}$	13.06	80.49	12.19
	8.17	71.32	10.34
	3.48	53.27	4.94
$h = 100\,\mu\text{m}$	19.54	96.86	12.74
	13.06	82.00	11.42
	3.48	73.19	10.50

Table 7.1: Bubble radius and velocity determined from the experimental data which serve as initial conditions for the cylindrical Rayleigh-Plesset model.

The dynamics of such a cylindrical cavity are described by the cylindrical Rayleigh-Plesset equation [98]

$$\left(R\ddot{R}+\dot{R}^2\right)\log\frac{R}{R_\infty}+\frac{1}{2}\dot{R}^2=\frac{1}{\rho}\left[p_\infty-\left(p_v-\frac{2\sigma}{R}\right)+E_{visc}\right], \tag{7.1}$$

where a dot denotes differentiation with respect to time and E_{visc} models viscous dissipation. In the application of this model we take as R_∞ the radius of the glass disc and as p_∞ the undisturbed, or ambient, pressure. This choice is motivated by the fact that the liquid between the glass plates outside the gap where the bubble is generated is essentially stagnant.

The viscous drag depends on the velocity field which is not calculated in this model. As a first approximation we assume a parabolic velocity profile which, as shown in appendix B, leads to

$$E_{visc}=20\rho\nu R\dot{R}\left\{\frac{1}{10}\left[\frac{1}{R^2}-\frac{1}{R_\infty^2}\right]+\frac{1}{4h^2}\log\frac{R_\infty}{R}\right\}, \tag{7.2}$$

where ν is the kinematic viscosity. As for most of the process $h << R$ this expression can be approximated by

$$E_{visc}\approx 5\rho\nu R\dot{R}\frac{1}{h^2}\log\frac{R_\infty}{R}. \tag{7.3}$$

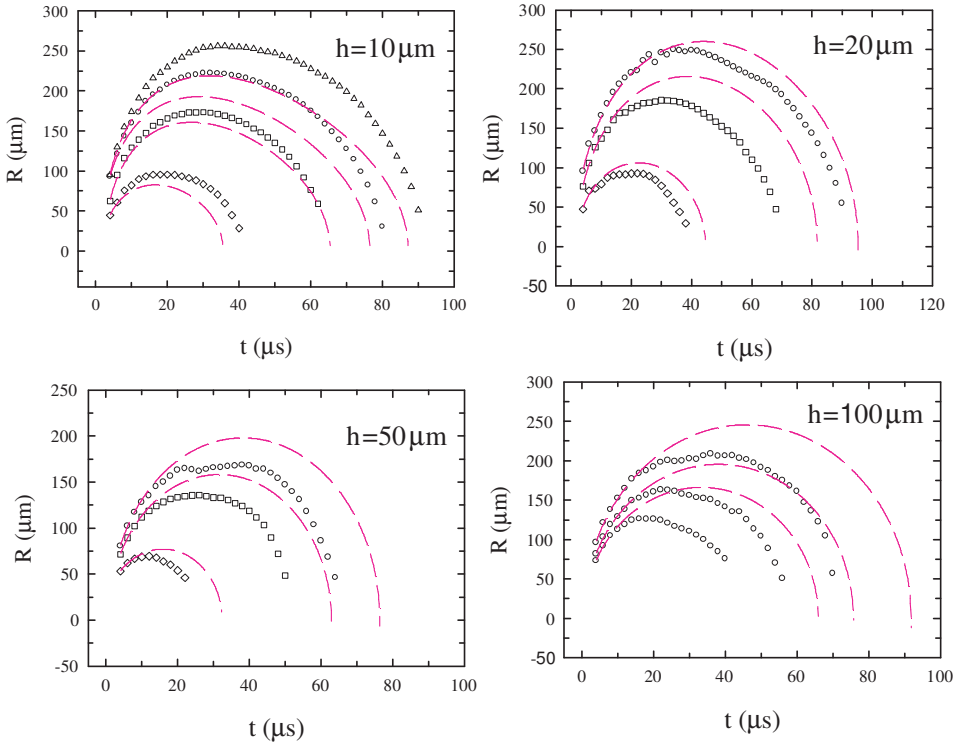

Figure 7.4: Open symbols: experimental bubble radius. Dashed lines: results from solving the cylindrical Rayleigh-Plesset model, Eqs. (7.1) and (7.3), with the initial conditions listed in table 7.1.

Supplying the initial bubble radius and velocity, Eq.(7.1) can be solved. These initial conditions are determined from the experimental data and are listed in table 7.1 for various gap heights and laser pulse energies. From this table it is clear that the bubble radii that serve as the initial condition are either larger than the gap height or comparable to it so that the vapor pressure has already dropped substantially so that we can disregard it. The liquid properties used are: $\rho = 10^3\,\mathrm{kg/m}$, $\mu = 10^{-3}\,\mathrm{kg/m\,s}$ and $\sigma = 0.073\,\mathrm{N/m}$. All calculation are carried out with the extent of the liquid equal to the size of the disc, thus $R_\infty = 7.5\,\mathrm{mm}$.

The results of the model are shown in figure 7.4 by the magenta dashed curves, together with the experimental data (open symbols). Clearly the model underestimates the viscous dissipation for all disc spacings except the smallest. The assumption of a parabolic velocity profile does not seem to be valid, particularly for the larger gap

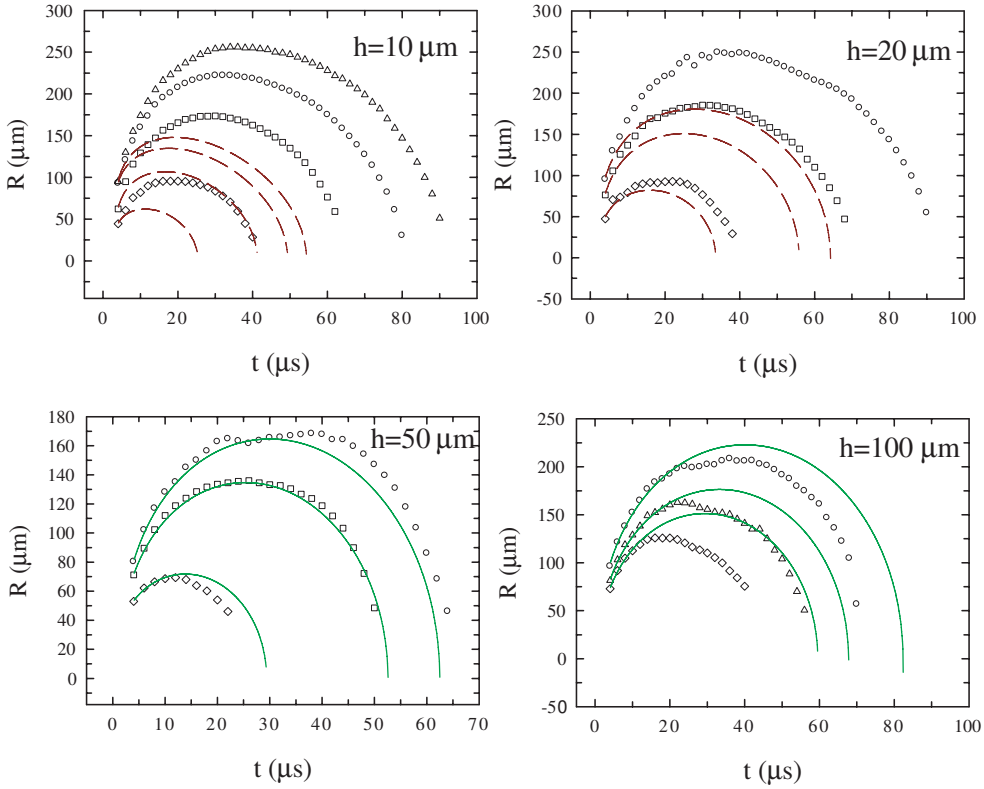

Figure 7.5: Open symbols: experimental bubble radius. Dashed/solid lines: results from solving the cylindrical Rayleigh-Plesset model. The viscous dissipation is model used is Drag I, i.e. using Eqs. (7.4) and (7.3).

heights. The dissipation can be increased by taking into consideration the time evolution of a viscous boundary layer of thickness δ at the discs' surface. This leads to replacing h by δ in Eq. (7.3):

$$E_{visc} = 5\rho\nu R\dot{R}\frac{1}{h\delta}\log\frac{R_\infty}{R}. \tag{7.4}$$

The boundary layer thickness is estimated as

$$\delta = \sqrt{\pi\nu t} \tag{7.5}$$

during the growth phase and as

$$\delta = \sqrt{\pi\nu(t - t_{max})} \tag{7.6}$$

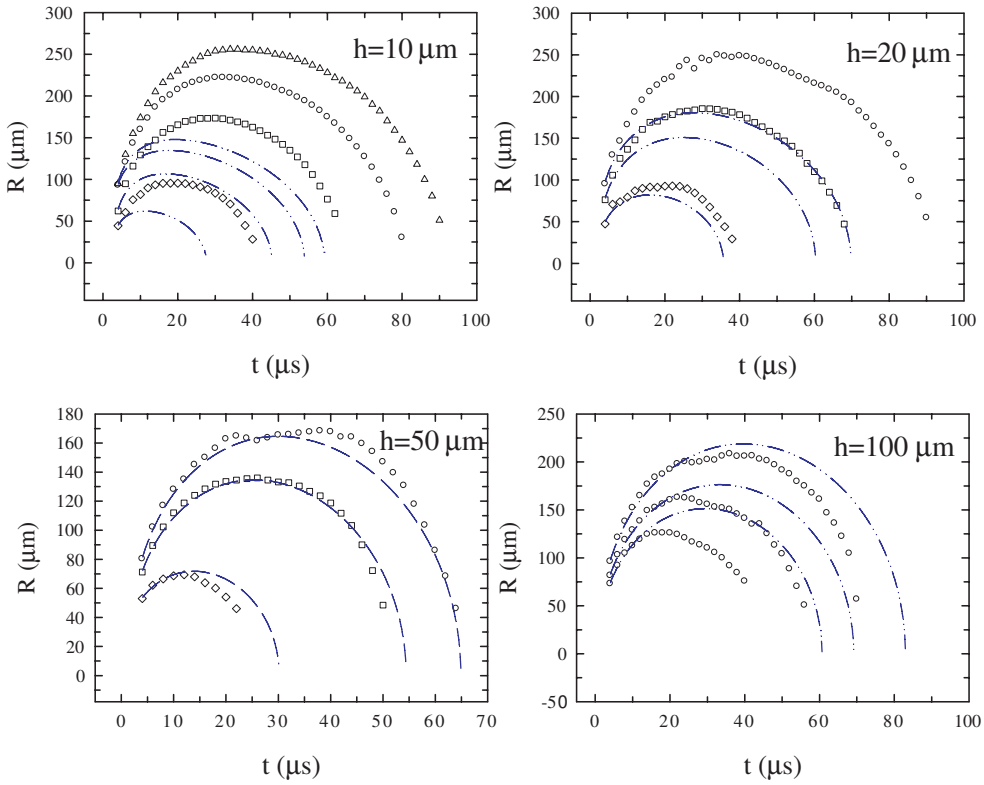

Figure 7.6: Open symbols: experimental bubble radius. Dashed lines: results from solving the cylindrical Rayleigh-Plesset model. The viscous dissipation is model used is Drag II, i.e. using Eq. (7.4) for both growth and collapse.

during the collapse, where t_{max} is the time of maximum expansion of the bubble. This procedure accounts for the restart of the flow after the liquid velocity approximately vanishes at the bubble maximum. For the collapse phase we have also used (7.3). In the following we refer to the combination of (7.4) and (7.3) as Drag I, while when the boundary layer model is used for both growth and collapse we call it Drag II.

The results of these models are quite similar and are shown in figures 7.5 and 7.6 respectively. The predicted bubble sizes are much smaller with these viscous dissipation models. However, for the largest gap heights the models still predict a bubble size that is too large. For $h = 50\,\mu$m they are able to fit the experimental data, while for the two smallest gaps the predicted bubble radius is too small.

7.3.2 Including thermal effects

Just as was seen for the tube, a model based on purely mechanical effects cannot explain the bubble dynamics. We proceed similarly to our treatment of the one-dimensional case including thermal effects by writing an energy balance for the vapor. This balance equates the latent heat of phase change with the sum of the energy flow from the liquid to the vapor and the energy needed to maintain the vapor at saturation state. The latent heat of phase change is

$$\begin{aligned} L\frac{d}{dt}\left(\rho_v V\right) &= L\frac{d}{dt}\left(\rho_v \pi R^2 h\right) \\ &= 2\pi RhL\rho_v \dot{R} + \pi R^2 hL\dot{\rho}_v \\ &= 2\pi RhL\rho_v \dot{R} + \pi R^2 hL\left(\frac{L}{\mathscr{R}T_s} - 1\right)\frac{\rho_v}{T_s}\frac{dT_s}{dt}, \end{aligned} \tag{7.7}$$

with L the latent heat of phase change, V the bubble volume, $\mathscr{R}$ the universal gas constant divided by the vapor mass and T_s the temperature at the bubble surface.

The energy conducted at the vapor/liquid interface contains two terms, one for the flux at the cylindrical interface at $r = R$ and one for the flux at the glass discs

$$2\pi Rhk\left.\frac{\partial T}{\partial r}\right|_{r=R} + 2\pi R^2 k\left.\frac{\partial T}{\partial z}\right|_{z=0}, \tag{7.8}$$

where k is the thermal conductivity of the liquid. One final term is needed to express the energy required to maintain saturation conditions for the vapor and is written as

$$\rho_v c_s V\frac{dT_s}{dt} = \rho_v c_s \pi R^2 h\frac{dT_s}{dt}, \tag{7.9}$$

where $c_s = c_{p,v} - L/T_s$ is the vapor specific heat along the saturation curve. Combining the three terms and dividing by $\pi R^2 h$ one arrives at

$$\begin{aligned} \rho_v c_s\frac{dT_s}{dt} &= 2k\left(\frac{1}{R}\left.\frac{\partial T}{\partial r}\right|_{r=R} + \frac{1}{h}\left.\frac{\partial T}{\partial z}\right|_{z=0}\right) \\ &\quad - \left(L\frac{2\rho_v \dot{R}}{R} + \left[\frac{L^2}{\mathscr{R}T_s} - L\right]\frac{\rho_v}{T_s}\frac{dT_s}{dt}\right). \end{aligned} \tag{7.10}$$

We solve this model for the two smallest gaps only, because the previous mechanical model where the vapor pressure was taken approximately zero already predicted bubble sizes and bubble lifetimes that were too large. The presence of thermal effects

$h = 10\,\mu$m	Energy (μm)	$T_s(0)\,^\circ$C	$h = 20\,\mu$m	Energy (μm)	$T_s(0)\,^\circ$C
$\delta = 1\,\mu$m	19.54	220	$\delta = 1\,\mu$m	19.54	185
	13.06	205		13.06	168
	8.17	207		8.17	148
	3.48	190			

Table 7.2: Initial bubble surface temperature and thermal boundary layer thickness selected for the model including thermal effects for various laser pulse energies and gap heights of $h = 10, 20\,\mu$m.

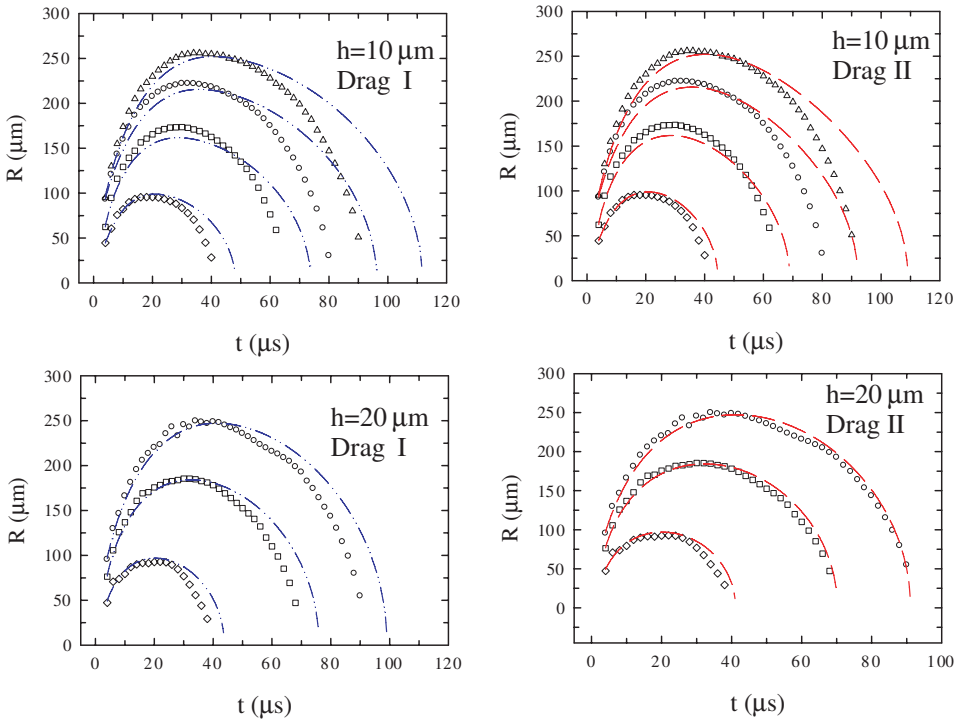

Figure 7.7: Open symbols: experimental results for bubble radius. Dashed lines: Results of the model including thermal effects and the glass discs are treated adiabatically.

will only enhance this feature as the vapor pressure remains higher during the collapse slowing it down. The present model requires an initial temperature distribution that needs to be specified. As for the tube, a Gaussian distribution is assumed

$$T(r,0) = T_\infty + \Delta T \exp\left(-\frac{r}{\delta_T}\right)^2, \tag{7.11}$$

where ΔT is the initial difference between the vapor temperature and the ambient temperature, and δ_T is the initial thermal boundary layer thickness. The initial conditions selected for this model are shown in table 7.2. As a first approximation we will consider the glass discs to be adiabatic, so that $[\partial T/\partial z]_{z=0} = 0$. Figure 7.7 shows the results of the model for gap heights of $h = 10$ and $20\,\mu$m using both models, Drag I and Drag II, for the viscous dissipation. We see that the maximum bubble size is captured but the bubble lifetime is overestimated. This overestimation is particularly clear for the small gap, indicating that the vapor temperature is decreasing too slowly so that the pressure remains high for too long. This is not surprising as we neglected the energy flux at the glass discs, which may be considerable.

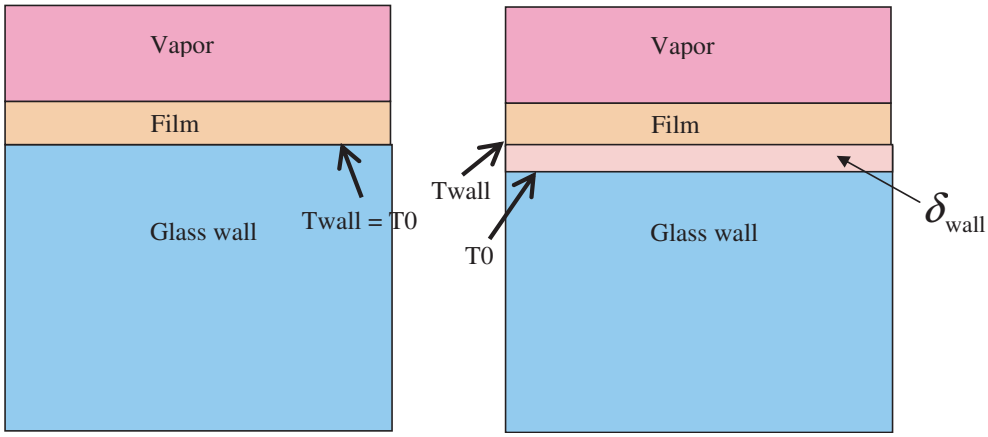

Figure 7.8: Sketch for the 1D conduction at the glass disc. The left part shows the situation at $t = 0$ when there has been no conduction. The right part shows the development of a thermal boundary layer in the glass thus raising the temperature at the glass/liquid interface.

In order to properly account for this effect, we must realize that, due to the no-slip condition, a thin liquid film of thickness δ_l separates the vapor from the glass plates (see figure 7.8). The vapor heat is conducted to the glass through this liquid film and gives rise to a thermal boundary layer in the glass discs. The size of this boundary

layer may be approximated as

$$\delta_{wall} = \sqrt{\pi D_{wall} t} \tag{7.12}$$

The heat flux from the liquid film to the glass must be the same as the energy put into the thermal boundary layer δ_{wall}, so

$$k_l \frac{T_s - T_{wall}}{\delta_l} = k_w \frac{T_{wall} - T_0}{\delta_{wall}}, \tag{7.13}$$

with k_l,k_w the thermal conductivities of the liquid and the glass respectively, and the other quantities as defined in figure 7.8. From this the temperature at the liquid/glass interface is obtained as

$$T_{wall} = \frac{\frac{\delta_{wall}}{\delta_l} k_l T_s + k_w T_0}{\frac{\delta_{wall}}{\delta_l} k_l + k_w}. \tag{7.14}$$

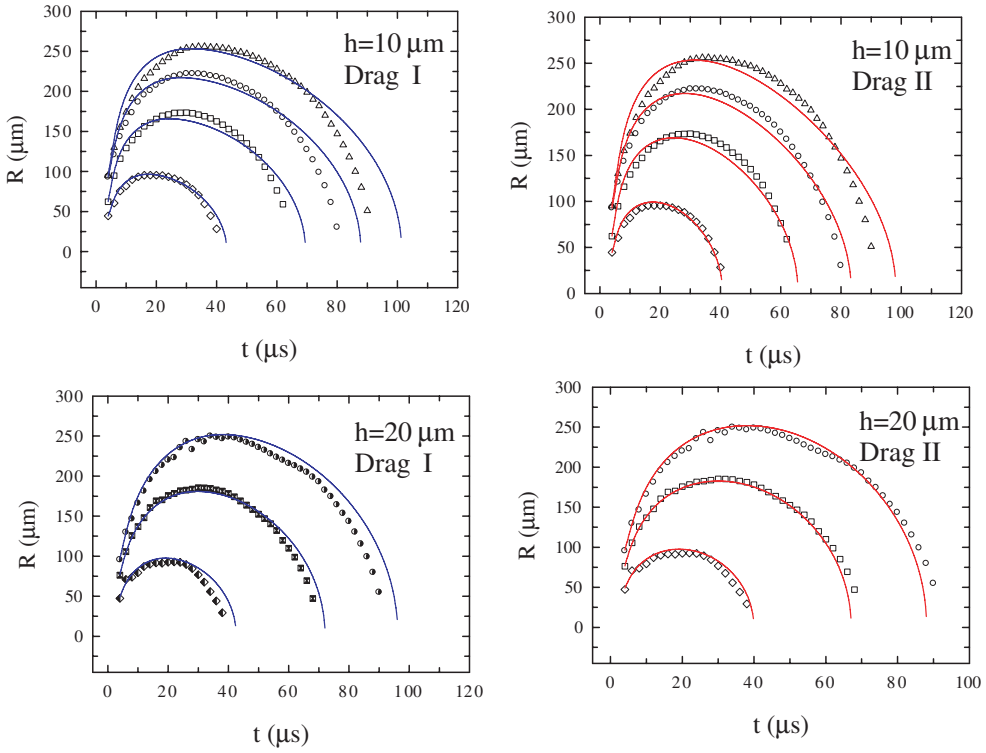

Figure 7.9: Open symbols: experimental results for bubble radius. Dashed lines: Results of the model including thermal effects and a non-zero heat flow into the glass.

From the experiments the liquid film thickness was estimated as 1 μm for all cases.

The results of solving the model with the non-zero heat flux at the glass discs are shown in figure 7.9. The prediction of the bubble lifetimes has improved considerably for the small gap case. For the larger gap the wall heat flux does not seem to have much influence. The reason for this may lie in the fast decrease of vapor temperature. Almost all of the energy is expended in the initial phase of the growth. For the larger gap the temperature has dropped to its final value by the time the bubble has grown to a size comparable to the gap height, so that the heat flux at the glass discs is negligible. For the small gap on the other hand the heat flux may still be important as the bubble reaches the size of the gap before the energy has been expended.

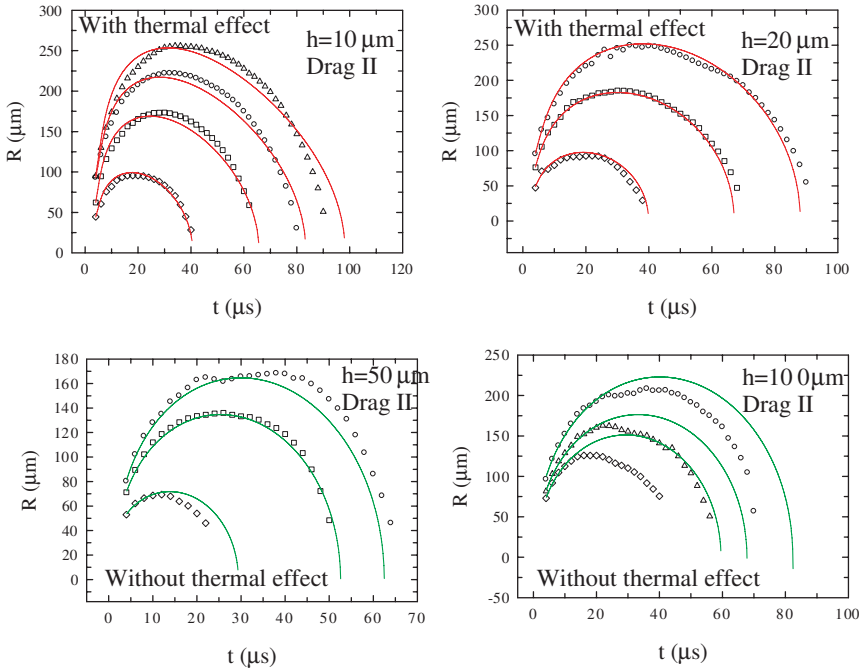

Figure 7.10: Best results that we acquired from the model. The small gap heights are modeled including thermal effects. The large gap heights already overestimate the bubble size. Including thermal effects for these cases would only enhance the overestimation.

To summarize the quality of the various models presented we plot the best results for all gap heights in figure 7.10. The thermal effects are used for the two smallest gaps. The two largest gaps have been modeled neglecting the thermal effects because this already leads to the minimum possible vapor pressure and the bubble lifetime is

already too long. Even though a reasonable fit has been obtained for all cases, it is clear that we had to resort to many *ad hoc* assumptions to obtain these fits. Furthermore, in contrast to the one-dimensional model of chapter 2 which was sufficient to account for all cases without adjustments, here the fits for the various gap heights are obtained using different models. Clearly, the system is too complex to be described by a simple model. These results suggest that a fuller simulation of the underlying physics is required to reveal the complexities of the bubble dynamics.

7.4 Simulation setup

The results of the numerical method applied to the tube geometry were qualitatively similar to the experimental data. Even though a quantitative comparison with experiment was not possible due to the differences in tube aspect ratios, the computational results did correspond well quantitatively with an estimate based on a simplified model. Furthermore, the full solution of the governing equations of the system provides detailed knowledge about the bubble shape and the temperature field in the liquid. Information about the bubble shape is important because it affects and is affected by the fluid flow. In the present case of a bubble between the discs, where the system cannot be viewed from the side, the numerical method therefore provides additional information that cannot be obtained otherwise.

A schematic of the computational domain used for the simulations of the current system is shown in figure 7.11. Once more we take advantage of symmetry and simulate a quarter of the domain imposing symmetry on the midplane. Hence for simulating a bubble between discs of diameter D and gap height h the computational domain is of size $[0, D/2] \times [0, h/2]$. The top boundary is the glass disc and therefore

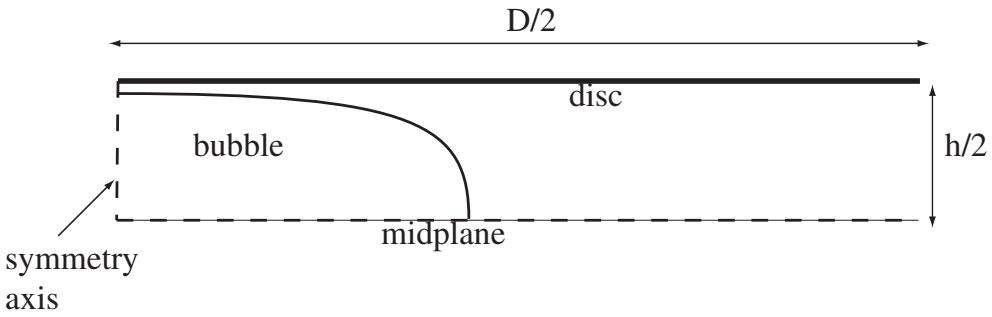

Figure 7.11: Schematic of the computational domain

no-slip conditions are imposed there. As for the tube calculation, we make sure the bubble does not come into contact with the top boundary as the velocity extrapolation routine needs valid velocity values. For this purpose the axial velocity component with which the interface is advected is put to zero. As before, here this restriction has only a minor influence as the flow near the plate is extremely slow anyway. For the purpose of solving the energy equation, the top boundary is treated either as adiabatic or isothermal. At the outer edge of the computational domain the pressure is required to equal the reference pressure, which is taken as atmospheric, and the velocity gradients normal to the boundary are set to vanish. The domain on which the energy equation is solved is again only part of the momentum domain. We choose it large enough so that the temperature at the right thermal domain boundary remains at its undisturbed value of $T_\infty = 25\,^\circ C$.

The disc size and gap heights used in the experiment result in aspect ratios, defined as the ratio of disc diameter to gap height, ranging from 150 to 1500. Therefore, we find ourselves in the same situation as in the tube simulations and take a smaller aspect ratio for the numerical treatment for the same reasons explained in the previous chapter. We have performed our simulations with an aspect ratio of 20. Some comments on the effect of the aspect ratio will be included later (section 7.5)

The scales used for non-dimensionalizing the governing equations are the same as in the tube geometry except for the length scale, which in this case is taken as the gap height between the discs, h. Thus the velocity scale is

$$V = \sqrt{\frac{\Delta p h}{\rho D}} = \sqrt{\frac{\Delta p}{\rho A}}, \tag{7.15}$$

where $A = D/h$ is the aspect ratio and $\Delta p = p_v(t=0) - p_\infty$. A time scale is defined using the length and velocity scales, $t^\star = h/V$. The temperature is normalized as

$$\theta = \frac{T - T_\infty}{T_{sat}(p_\infty) - T_\infty}, \tag{7.16}$$

with $T_{sat}(p_\infty)$ the saturation temperature evaluated at the reference pressure. Using these scales Reynolds, Weber and Péclet numbers are defined in the usual way

$$Re = \frac{\rho V D}{\mu}, \qquad We = \frac{\rho V^2 D}{\sigma}, \qquad Pe = \frac{V D}{\alpha}. \tag{7.17}$$

The liquid properties are also selected as they were in the simulations of the bubble in the tube, so $\rho = 10^3\,\mathrm{kg/m^3}$, $\mu = 1.4 \times 10^{-3}\,\mathrm{kg/ms}$, $\sigma = 0.073\,\mathrm{N/m}$ and $\alpha = 8.5 \times 10^{-7}\,\mathrm{m^2/s}$.

$h\,(\mu\mathrm{m})$	$T_v(t=0)(^\circ\mathrm{C})$	Re	We	Pe
50	170	226	27	372
	185	271	39	446
	200	320	55	528
	227	424	96	698

Table 7.3: Parameters for the simulations carried out for $h = 50\mu$m. Initial vapor temperature and corresponding non-dimensional numbers. The initial thermal boundary layer for all cases is $\delta = 0.75R_0$.

7.5 Simulation results

We start by simulating a system for which the thermal and viscous boundary layers can be resolved with confidence, i.e. a system with moderate Re and Pe numbers. For this we take a gap height of $h = 50\,\mu$m. The bubble is initialized as a sphere of radius R_0 and the the liquid temperature field as a Gaussian distribution:

$$T(r,z,0) = T_\infty + \Delta T \exp\left[-\left(\frac{|\mathbf{x}| - R_0}{\delta_T}\right)^2\right], \tag{7.18}$$

where $|\mathbf{x}| - R_0$ is the distance from the point $\mathbf{x}$ to the bubble surface, ΔT is the temperature difference between the initial vapor temperature and T_∞ and δ_T is the thermal boundary layer thickness. All simulations are carried out with $\delta_T = 0.75R_0$, and adiabatic conditions at the top boundary are imposed on the temperature. Various initial vapor temperatures are used, which are listed in table 7.3 together with the resulting non-dimensional numbers. Note that these are the same parameters as we chose for the simulations carried out for the bubble in the tube. The bubble radius is calculated as the distance from the axis of symmetry of the point of intersection of the bubble surface with the midplane of the system. The bubble interface velocity is calculated at this point also.

The results for the bubble radius, interface velocity, vapor temperature and pressures for these parameters are shown in figure 7.12. Several observations can be made from these results. First of all the trend of the predicted bubble radius agrees well with that from the experimental data. The collapse phase, which for this geometry is markedly different from that of the tube geometry, is correctly captured by the numerical method. This can be seen clearly from the interface velocity which becomes very negative near the end of the collapse. As before, we cannot carry out a direct quantitative comparison with experiment due to the different aspect ratios and

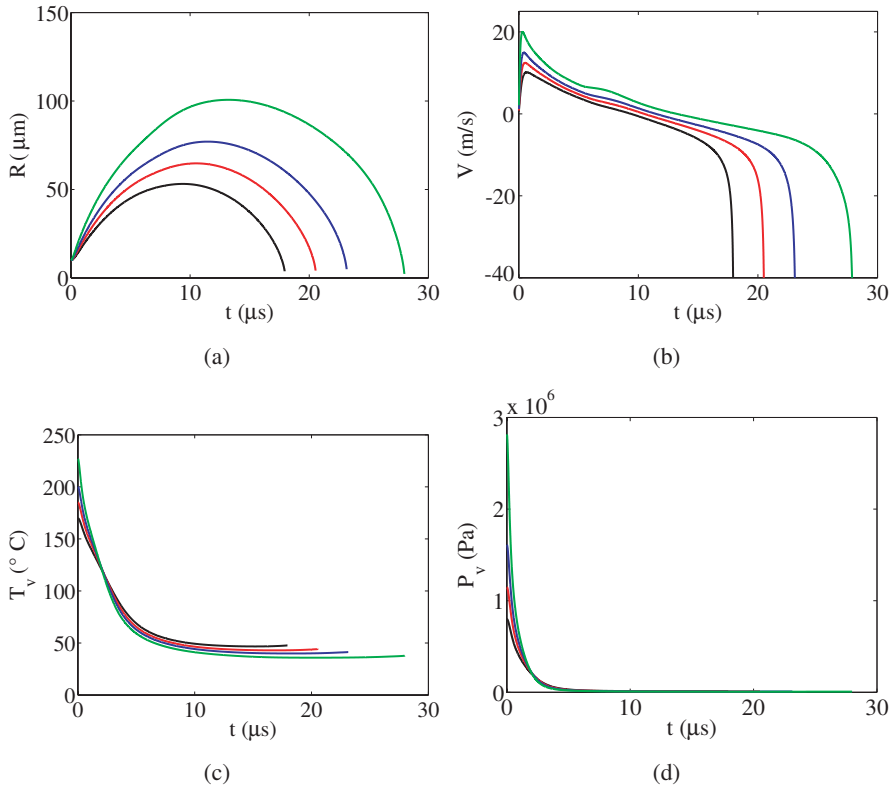

Figure 7.12: Simulation results for a gap height of $50\,\mu$m and aspect ratio of 20. The system is simulated with various initial vapor temperatures. Black: $T_v(0) = 170\,^{\circ}$C, red: $T_v(0) = 185\,^{\circ}$C, blue: $T_v(0) = 200\,^{\circ}$C, green: $T_v(0) = 227\,^{\circ}$C. The initial thermal boundary layer thickness is $\delta_{therm} = 0.75R_0$.

the unknown initial conditions. However, the discrepancy between the predicted bubble lifetime for this system and the experimentally observed values for this quantity is much smaller than was seen in the tube geometry, even though the aspect ratio in the experiments was 15 times larger than that used in the simulation. The bubble lifetimes from experiments for $h = 50\,\mu$m ranged from 25 to $65\,\mu$s, while the predicted values are approximately twice as short. This would imply that the aspect ratio does not have a large influence on the dynamics for this geometry. We may explain this by the fact that the liquid inertia is proportional to the logarithm of the ratio of the bubble radius to outer domain boundary (see Eq. (B.25)). Therefore, to increase the amount of inertia by a factor of two, the outer domain boundary must be increased a

factor $e^2 \simeq 7.4$ times. This remark is interesting as it leads one to expect a smaller difference with experiment than was found in the tube case. The vapor temperature and pressure curves are very similar to what was seen in the tube geometry. Also here there is little variation in the final vapor temperatures that are reached for different initial vapor temperatures.

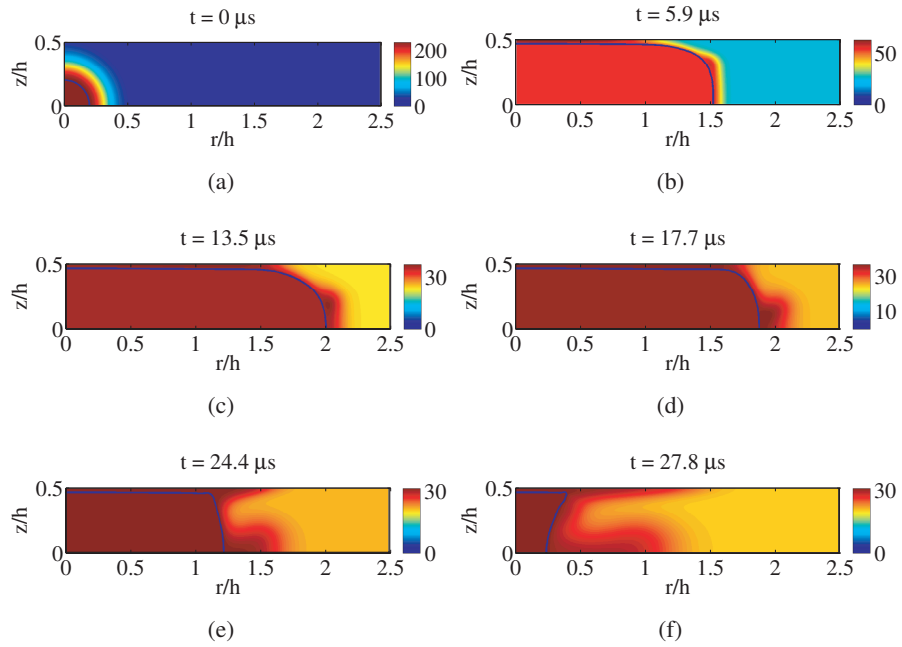

Figure 7.13: Several instants during growth and collapse showing the bubble interface and temperature field. $Re = 424$, $We = 96$, $Pe = 698$

The evolution of the temperature field for the simulation started with a vapor temperature of 227 °C is shown in figure 7.13. The figure shows the bubble interface and the temperature field at several instants during growth and collapse. The initial state is shown in panel (a). After about $6\,\mu$s the bubble has almost reached its maximum size, as seen in panel (b), and has a cylindrical shape. The temperature has dropped almost to its final value, indicating that the expansion is proceeding essentially by inertia. Also for this geometry a region of hotter fluid is seen. For the tube geometry this region was immediately above the spherical cap of the bubble on the axis of symmetry, where it remained during the rest of the process. Here however the hot region starts away from the midplane close to the disc. At maximum expansion,

$h\,(\mu\mathrm{m})$	$T_v(t=0)(^\circ\mathrm{C})$	Re	We	Pe
100	170	452	55	744
	185	541	78	892
	200	641	110	1056
	227	847	192	1396

Table 7.4: Parameters for the simulations carried out for $h = 100\mu$m. Initial vapor temperature and corresponding non-dimensional numbers. The initial thermal boundary layer for all cases is $\delta = 0.75R_0$.

as shown in panel (c), this region is advected towards the midplane during the flow reversal. The temperature field during the collapse phase, panels (d-f), shows similar features as for the tube. The temperature field is stretched due to advection and the formation of a tongue of cooler liquid separating the hotter regions near the glass disc and the midplane is seen. An interesting difference however is seen in the bubble shape, specifically during the final stages of the collapse. While the bubble in the tube remained convex during the whole collapse, here it acquires a concave shape in the final stages. This phenomenon appears due to the much larger velocities which conservation of the kinetic energy requires in a converging flow such as the present one. The liquid near the glass plates cannot keep up with this large acceleration. This geometrical effect is evidently absent in the tube case where surface tension is able to prevent the inward folding of the interface. Figure 7.14 shows the bubble shapes during growth and collapse for all four cases. The time between successive shapes is $0.1t^\star$. The concave shape during collapse is seen for all initial conditions, although it is most pronounced for the simulations started with the highest initial vapor temperature. From the distance between successive curves one can get an idea of the velocity magnitude causing the deformation of the bubble.

This effect should be stronger when surface tension and viscous effects are weaker. This is the case for a system with a larger gap between the discs. Therefore we simulated the same system with a gap of $h = 100\,\mu$m. The initial vapor temperatures and corresponding non-dimensional numbers are listed in table 7.4. As the resulting Re and Pe numbers are larger obtaining truly grid-independent results requires the use of grids with a higher resolution than the one we used for these simulations. Nevertheless, the qualitative features are clearly captured. The bubble shapes are shown in figure 7.15. The weaker surface tension is noticeable both in the growth and collapse phase. During the growth the advancing front of the bubble can be seen to oscillate, which is most clearly visible in parts (e) and (g). These are capillary waves, also due

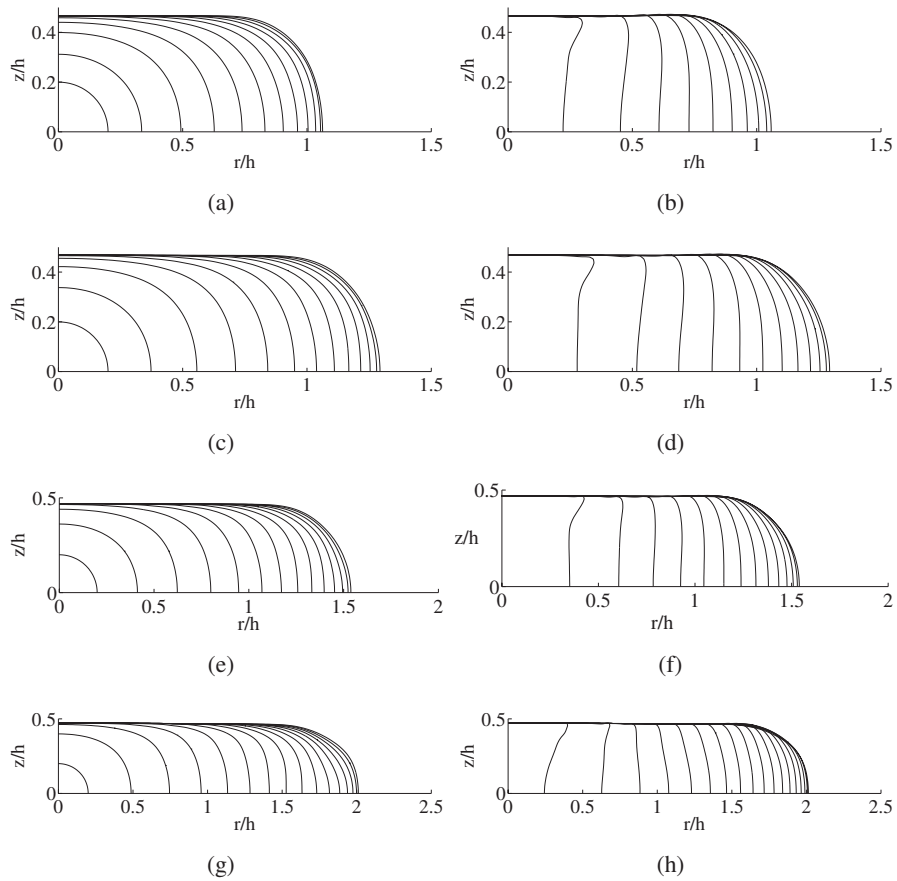

Figure 7.14: Bubble shapes for the simulation with $h = 50\mu$m. The figures on the left show the bubble shape during the expansion, on the right the collapse phase is shown. The results for the four initial temperatures used are shown. (a),(b): $T_v(0) = 170\,^\circ$C, (c),(d): $T_v(0) = 185\,^\circ$C, (e),(f): $T_v(0) = 200\,^\circ$C, (g),(h): $T_v(0) = 227\,^\circ$C. The bubble shapes during growth phase are quite similar to those seen for the bubble growing in the tube. The collapse however proceeds quite differently. The bubbles acquire a concave shape in the final stages of collapse, whereas in the tube geometry the bubbles stayed convex.

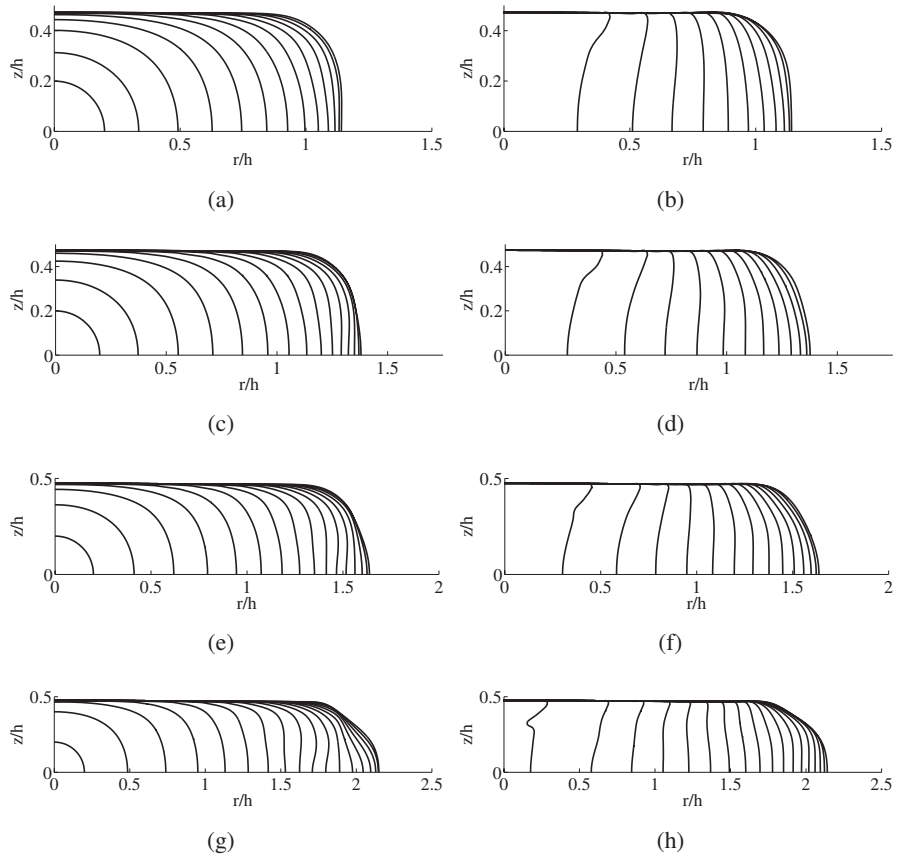

Figure 7.15: Bubble shapes for the simulation with $h = 100\mu$m. The figures on the left show the bubble shape during the expansion, on the right the collapse phase is shown. The results for the four initial temperatures used are shown. (a),(b): $T_v(0) = 170\,^\circ$C, (c),(d): $T_v(0) = 185\,^\circ$C, (e),(f): $T_v(0) = 200\,^\circ$C, (g),(h): $T_v(0) = 227\,^\circ$C.

to weak surface tension effects. From the collapse stages it is clear that the bubble becomes concave earlier and also to a larger degree. The kink in the final curve of part (h) is probably an artifact caused by an insufficient resolution.

7.6 Ray tracing

In figure 7.2 we showed several frames of the bubble evolution for gap heights of 10 and 100 μm. A lot of structure in the light intensity was seen from these measurements. Bright and dark rings could be clearly seen. For the smaller gap these rings remained thin throughout the growth and collapse, but for the larger gap a broad dark ring was observed during the collapse of the bubble. These rings must be the result of the way light travels through the system, reflecting and refracting at the liquid/vapor interfaces. Using geometrical optics the propagation of a light ray through the system can be calculated. In this section we carry out such calculations with model bubble shapes suggested by the numerical simulations, to determine whether these can indeed produce the structures seen in the light intensity. For this purpose we have written our own basic ray propagation algorithm. We proceed as shown in figure 7.16.

Although, for simplicity, we use a prescribed model bubble shape, we still use the level set function to calculate the normal vectors to the interface. The level set

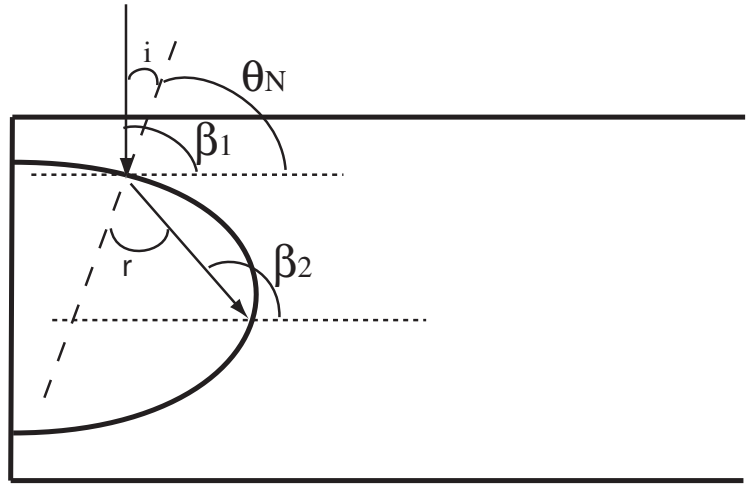

Figure 7.16: Schematic illustrating the angles involved in computing the propagation of a light ray refraction at the vapor-liquid interface.

function is calculated from Eq. (3.16) in a domain discretized by means of square computational cells as usual. This discretized grid is also useful to calculate the ray path as we now explain.

Light rays enter the top glass plate normally. As it propagates downward, a light ray traversing a plane $z = z_j$ at a distance r_j from the axis of symmetry, traverses the plane $z_{j-1} = z_j - \Delta z$ at a distance given by

$$r_{j-1} = r_j - \frac{\Delta z}{\tan(\beta_j)} \tag{7.19}$$

where β_j is the angle that it makes with the horizontal. The level set function at the new position (r_{j-1}, z_{j-1}) is computed by interpolation, as the new location in general does not coincide with a grid point. By comparing the signs of the level set function at the new and old locations it can be determined whether the light ray has crossed an interface. In this case, a new propagation angle needs to be computed. For this Snell's law for refraction is used

$$n_i \sin\theta_i = n_r \sin\theta_r\,, \tag{7.20}$$

with θ_i and θ_r the angles of incidence and refraction respectively. For the water refractive index we take $n_w = 1.3$ and for the vapor $n_v = 1$. The angle of incidence must be computed first. This is done by computing the angle between the normal vector at the point where the ray crosses the interface and the radial axis. As the radial and axial components N_r and N_z of the normal vector are known, this angle is calculated as $\tan\theta_N = N_z/N_r$. The angle of incidence is then given by $\theta_i = \beta_j - \theta_N$. The new propagation angle, β_{j-1} is then expressed in terms of the old propagation angle β_j and the angles of incidence and refraction as

$$\beta_{j-1} = \beta_j + \theta_r - \theta_i\,, \tag{7.21}$$

which is obvious from the figure. Propagation of the ray then continues in the same fashion with this new angle, until it crosses the interface again, whereupon the above procedure is repeated to compute a new propagation angle.

In addition to refraction, a ray may also undergo total reflection at the interface. This can only happen when the ray is going from the optically denser medium to the less dense medium, i.e. from the liquid to the vapor. With the previous values of the indices of refraction, the critical angle is $\theta_c = \arcsin(n_v/n_w) = 50.3^\circ$. Thus, when the ray hits the bubble interface with an angle of incidence larger than θ_c, there is no refraction but only reflection. We take this into account in the ray propagation algorithm.

As a test case let us consider a spherical bubble, which refracts the incoming light similar to a negative lens. The results of this calculation are shown in figure 7.17. Part (a) shows the light rays refracting and reflecting from the bubble surface. Only the rays that hit the bubble, and from these only one out of ten is shown. The figure clearly shows the spreading effect of the bubble, as the light falling on it is distributed over a larger area. A relative intensity for the light arriving at the bottom disc can be defined by counting the number of rays that arrive within a certain spatial interval, which we typically take as $20\Delta r$ (with Δr the grid spacing) and dividing this number by the number of rays incident on the top glass disc in an equal interval. The rays that are counted at the bottom are only the ones that interact with the bubble. The rays that travel vertically downwards unhindered are not included in the calculation. This procedure is justified by the fact that in practice these rays would be essentially totally absorbed by the dye in the water. This strong absorption will also prevent the rays strongly deflected sideways from being visible from the bottom. In practice, one may expect that only rays propagating mostly through the vapor will contribute to the recorded image. These considerations should be borne in mind in interpreting the intensity calculations to be shown below.

The calculated relative intensity for the spherical bubble is shown in figure 7.17(b). Directly beneath the bubble we see a relatively high intensity. Moving away from the bubble we get a monotonic decrease in intensity.

The experiments for the larger gaps show a distinct broad ring with very low intensity during the collapse phase. An example of this is shown in figure 7.18 which is one frame during collapse from an experiment with $h = 100\ \mu$m. The intensity aver-

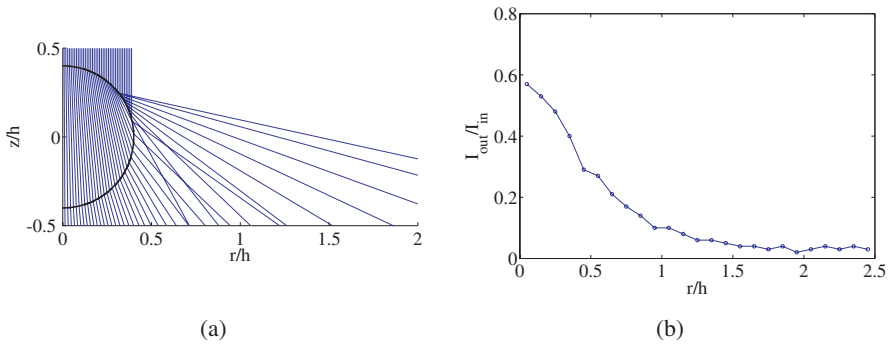

(a) (b)

Figure 7.17: (a): Propagation of rays through a spherical vapor bubble. (b): Relative intensity at the bottom glass plate

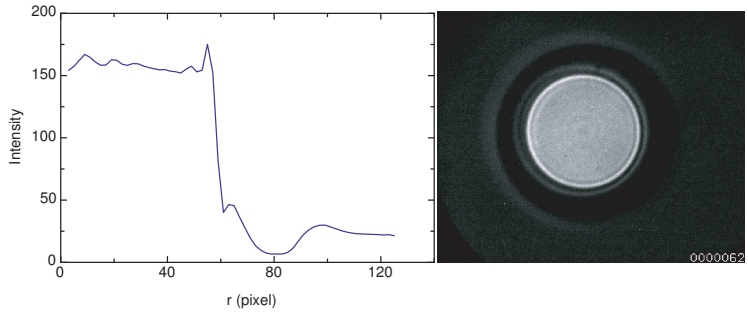

(a)

Figure 7.18: Left: Average intensity calculated from the experimental data for one instant during the collapse phase. The gap height for this experiment was $h = 100\mu$m. Right: video frame for the instant for which the average intensity is calculated.

aged over the entire 2π angle from this frame is shown as a function of distance from the axis of symmetry on the left. This intensity is fairly constant in the central part of the bubble away from the rim. Close to the edge a peak is visible corresponding to the bright ring in the figure on the right. Right next to it another peak is visible with a much lower intensity. Then the intensity drops to a very low value, corresponding the the dark ring, before reaching a fairly constant level again. This constant level is most likely due to light that travels through the liquid straight down to the bottom plate without meeting the bubble. It is interesting to note that the intensity in the dark ring is lower than this constant intensity. This is one of the features of the image that we now explain.

In trying to associate the observed light intensity with the bubble shape, for several reasons it is preferable to use model shapes rather than the computed shapes. In the first place, the geometrical optics calculation is rather crude due to the use of a discretized model and to the neglect of light absorption. Secondly, the precise instant of time, and the bubble shape corresponding to the experimental image, are unknown. Thirdly, the model shape permits us to accentuate certain features that bring out more clearly the expected effect on the light intensity. We assume a bubble shape described by a polynomial containing only even terms to reflect the expected symmetry about the midplane:

$$r(z) = a_0 + a_1\left(\frac{z}{h}\right)^2 + a_2\left(\frac{z}{h}\right)^4 + a_3\left(\frac{z}{h}\right)^6 + a_4\left(\frac{z}{h}\right)^8. \tag{7.22}$$

We take two shapes differing in the amount of concavity. The more pronounced

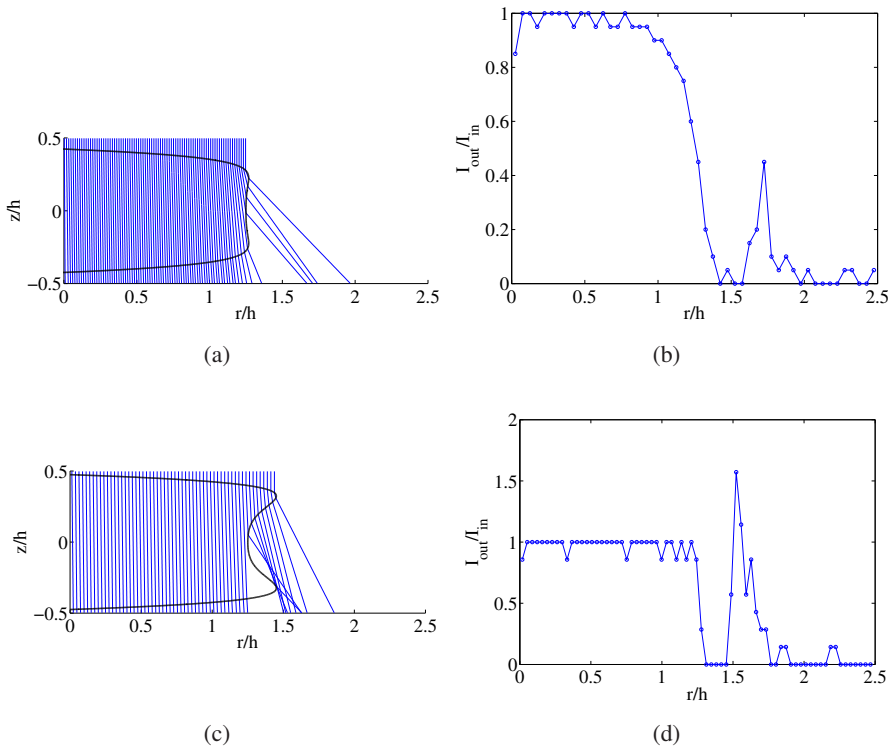

Figure 7.19: (a): Computation using the ray tracing algorithm for light rays propagating through a bubble exhibiting a slight concave shape. The bubble shape is not exactly the same resulting from simulation. Nevertheless, a dark region is seen to result due to the concavity. (b): Relative intensity resulting from the ray tracing computation.

concave shape would be attained by the bubble in the final moments of the collapse phase as shown e.g. in figure 7.15. The gap height for the calculation is taken as $h = 100\,\mu$m. The bubble shapes and the ray tracing results are shown in figure 7.19. Parts (a) and (c) show the bubble shapes and the rays refracting/reflecting at the liquid/vapor interface. In both cases a region where the rays do not arrive is clearly visible between the central plateau and a neighboring peak in parts (b) and (d) which show the calculated relative intensity profiles. These two dark regions have however a very different nature. The first one (part b) would be modified if we had retained the effect of the rays not interacting with the bubble. However, the second one (part d) would not, as clearly seen from part (c). The adjacent peaks are due to the light refracted by the edge of the bubble, although the relative intensity is probably over-

estimated by the neglect of absorption.

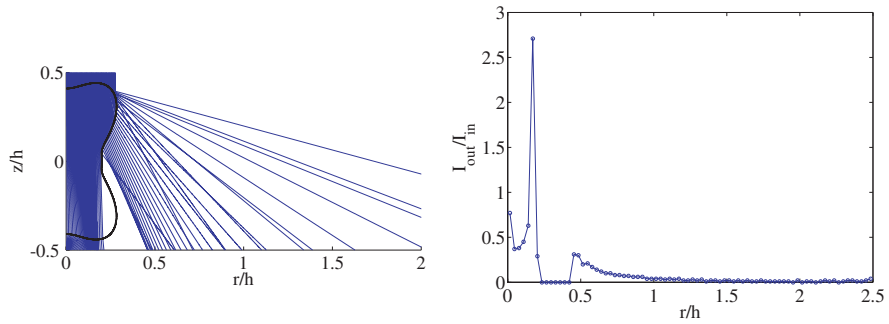

(a) (b)

Figure 7.20: (a): Ray tracing calculation for a bubble exhibiting a dimple near its edge. The dimple has a focussing effect which is clearly visible in the right figure. (b): Relative intensity resulting from the ray tracing computation.

By introducing an additional feature of the bubble shape we can account for the bright ring at the edge of the nearly uniform intense light region in figure 7.18. For this purpose we use a bubble shape given by

$$r(z) = R_0 \left[1 + \varepsilon_1 P_2(\cos\theta) + \varepsilon_2 P_4(\cos\theta) + \varepsilon_3 P_6(\cos\theta)\right] , \tag{7.23}$$

where

$$\cos\theta = \frac{r}{\sqrt{r^2 + z^2}} , \tag{7.24}$$

and the P_n's are Legendre polynomials. The distinctive feature of this shape is the dimple near the edge of the bubble, which has the effect of focusing the light as shown in the calculated intensity in the right part of figure 7.20.

Although qualitatively satisfactory, the results of these geometrical optics calculations should be taken with some reservations. The ray tracing calculation disregards absorption and the rays' interaction with the glass plates and other components of the system. Furthermore, the optical system used to image the bubble has a transfer function that is unknown. Finally, the multiple reflections between the bubble interface and the glass discs, which may be responsible for the fine features similar to Newton rings observable in some images, have not been included.

7.7 Summary

In this chapter we have considered the growth and collapse of a laser-generated vapor bubble confined between two solid discs and we have compared several different theoretical predictions with data.

Various models based on both purely mechanical effects and including thermal effects have been proposed for describing the dynamics of the bubble. We found that the model based on solely mechanical effects was unable to describe the data adequately, specifically for small gaps. Including thermal effects by writing an energy balance for the vapor we were able to get a better correspondence with the experimental data for the smaller gaps. However, a good understanding of the dynamics is not attained for the larger gaps by means of these models. Therefore the system has been studied numerical using the method of chapter 4. For practical reasons we did not use the same disc size as in experiment. Furthermore, the initial liquid temperature field is unknown and had to be assumed. For these reasons a direct quantitative comparison with experiment was not possible. However we did find that the trends of the dynamics were captured satisfactorily. Furthermore, as this system is relatively insensitive to the aspect ratio due to the logarithmic dependence of inertia on this quantity, our bubble lifetimes were comparable with those observed in experiment.

In the simulations we focussed on the bubble shape during collapse. The predictions showed that the rim of the bubble attains a concave shape during this stage, which had not been seen earlier. The reason for this shape is the fact that the strong radial velocity gradients dominate surface tension effects so that surface tension is not able to sustain the spherical shape that was seen for the tube. For corroborating that the bubble attains this concave shape in reality we used the experimental measurement of the light intensity with which the system is imaged. The intensity profile shows a broad low intensity ring structure seen only during collapse and most clearly for the larger gaps. We show by a simplified geometrical-optics calculation of the trajectories of light rays through the bubble that this ring structure is indeed formed by refraction and reflection for a bubble shape with a concave edge.

A

Derivation of the vapor-side heat flux

With the assumption of a spatially uniform pressure inside the bubble, the equation for the conservation of enthalpy may be written as

$$\frac{\partial}{\partial t}(\rho_v h_v) + \nabla \cdot (\rho_v h_v \mathbf{u}_v + \mathbf{q}_v) = \dot{p}_v \,, \tag{A.1}$$

where $\mathbf{q}_v$ is the heat flux and $\dot{p}_v = dp_v/dt$. Here and throughout this appendix vapor quantities are designated by the subscript v; liquid quantities carry no subscript. For a perfect gas, $\rho_v h_v = \gamma p_v/(\gamma-1)$, where γ is the ratio of specific heats. Upon integrating over the bubble volume we thus find

$$\frac{V}{\gamma-1}\dot{p}_v + \frac{\gamma}{\gamma-1}\, p_v \oint_S \mathbf{u}_v \cdot \mathbf{n}\, dS = -\oint_S \mathbf{q}_v \cdot \mathbf{n}\, dS \,. \tag{A.2}$$

Conservation of energy at the interface is expressed by

$$(\mathbf{q} - \mathbf{q}_v) \cdot \mathbf{n} = L\rho_v (\mathbf{u}_v - \mathbf{v}) \cdot \mathbf{n} \,, \tag{A.3}$$

with L the latent heat of phase change and $\mathbf{v}$ the interface velocity. Integrating over the interface where the temperature T_s is uniform and, therefore, the vapor density ρ_v is constant, gives

$$\begin{aligned} \oint_S \mathbf{u}_v \cdot \mathbf{n}\, dS &= \oint_S \mathbf{v} \cdot \mathbf{n}\, dS + \frac{1}{\rho_v L} \oint (\mathbf{q} - \mathbf{q}_v) \cdot \mathbf{n}\, dS \\ &= \dot{V} + \frac{1}{\rho_v L} \oint (\mathbf{q} - \mathbf{q}_v) \cdot \mathbf{n}\, dS \,. \end{aligned} \tag{A.4}$$

Upon substituting into Eq. (A.2) and rearranging we have

$$\oint_S \mathbf{q}\cdot\mathbf{n}\,dS = \frac{c_s}{c_{pv}}\oint_S \mathbf{q}_v\cdot\mathbf{n}\,dS - \frac{L}{(\gamma-1)\,c_{pv}T_v}\left(V\dot{p}_v + \gamma p_v\dot{V}\right) \tag{A.5}$$

When the characteristic time scale for surface temperature variation is long compared with the diffusion time in the vapor, the vapor is nearly isothermal. Under this hypothesis, the energy equation in the vapor can be approximated as

$$\rho_v c_{pv}\dot{T}_v - \dot{p}_v \simeq -\nabla\cdot\mathbf{q}_v\,. \tag{A.6}$$

A formal derivation of this result for a spherical bubble can be found in [99]. Upon integration over the bubble volume we have

$$\oint \mathbf{n}\cdot\mathbf{q}_v\,dS \simeq -V\left(\frac{\gamma}{\gamma-1}\frac{p}{T_s}\dot{T}_s - \dot{p}\right), \tag{A.7}$$

which, upon substitution into (A.5), gives Eq (3.10)

B

Cylindrical Rayleigh-Plesset model for a bubble between discs

Assuming a parabolic velocity profile, the velocity $u(r,z)$ can be obtained from continuity

$$u = Cz(h-z) \tag{B.1}$$

$$2\pi r \int_0^h u dz = 2\pi R\dot{R}h \tag{B.2}$$

$$u = \frac{6R}{r}\frac{z(h-z)}{h^2}\dot{R} \tag{B.3}$$

Defining the Lagrangian function

$$L = T - U = T\,, \tag{B.4}$$

as there is not potential energy considered in this system. The equation of motion is then derived from the Euler-Lagrange equation

$$\frac{d}{dt}\left(\frac{\partial L}{\partial \dot{R}}\right) - \frac{\partial L}{\partial R} = \frac{\partial W}{\partial \dot{R}} + \frac{\partial \varphi}{\partial \dot{R}}\,, \tag{B.5}$$

with W the work done by the pressure on the bubble, and φ the viscous dissipation.

The kinetic energy can be expressed by means of the velocity field as

$$L = \frac{1}{2} 2\pi\rho \int_R^{R_\infty} r dr \int_0^h u^2 dz \tag{B.6}$$

$$L = \frac{1}{2} 2\pi\rho \int_R^{R_\infty} r dr \int_0^h \frac{36R^2}{r^2} \frac{z^2(h-z)^2}{h^4} \dot{R}^2 dz \tag{B.7}$$

$$= \int_R^{R_\infty} r dr \frac{36\pi\rho R^2}{r^2} \int_0^1 \eta^2 (1-\eta)^2 \dot{R}^2 d\eta \tag{B.8}$$

$$= \frac{6}{5}\pi\rho h R^2 \dot{R}^2 \log\frac{R_\infty}{R}, \tag{B.9}$$

where we have used the variable transformation $\eta = z/h$ The terms on the left hand side of Eq. (B.5) can then be computed.

$$\frac{d}{dt}\left(\frac{\partial L}{\partial \dot{R}}\right) = \frac{12}{5}\pi\rho h \left\{ (R^2\ddot{R} + 2R\dot{R}^2)\log\frac{R_\infty}{R} - \dot{R}^2 R \right\} \tag{B.10}$$

$$\frac{\partial L}{\partial R} = \frac{12}{5}\pi\rho h \left\{ R\dot{R}^2 \log\frac{R_\infty}{R} - \frac{1}{2} R\dot{R}^2 \right\} \tag{B.11}$$

$$\frac{d}{dt}\left(\frac{\partial L}{\partial \dot{R}}\right) - \frac{\partial L}{\partial R} = \frac{12}{5}\pi\rho h \left\{ (R^2\ddot{R} + R\dot{R}^2)\log\frac{R_\infty}{R} - \frac{1}{2}\dot{R}^2 R \right\} \tag{B.12}$$

The work that is done by the pressure difference is expressed as

$$W = -(p_v - p_\infty) 2\pi h \dot{R} R h \tag{B.13}$$

$$\frac{\partial W}{\partial \dot{R}} Rh = 2\pi(p_\infty - p_v) Rh \tag{B.14}$$

The viscous dissipation is defined through the rate of strain tensor. The only non-zero contributions are the diagonal terms.

$$u = \frac{6R}{r}\frac{z(h-z)}{h^2}\dot{R} \tag{B.15}$$

$$e_{rr} = \frac{\partial u}{\partial r} = -\frac{6R}{r^2}\frac{z(h-z)}{h^2}\dot{R} \tag{B.16}$$

$$e_{rr2} = \frac{u}{r} = \frac{6R}{r^2}\frac{z(h-z)}{h^2}\dot{R} \tag{B.17}$$

$$e_{zz} = \frac{1}{2}\frac{\partial u}{\partial z} = 3\frac{R}{r}\frac{h-2z}{h^2}\dot{R} \tag{B.18}$$

$$e^2 = e_{rr}^2 + e_{rr2}^2 + e_{zz}^2 = \frac{36R^2}{r^2}\dot{R}^2\left\{\frac{2}{r^2}\eta^2(1-\eta)^2 + \frac{1}{4h^2}(1-2\eta)^2\right\} = \frac{36R^2\dot{R}^2h}{r^2}\left\{\frac{1}{15r^2} + \frac{1}{12h^2}\right\} \tag{B.19}$$

Integrating over the whole liquid domain to get the dissipation

$$\int_R^{R_\infty} 2\pi r dr \int_0^h e^2 dz = 72\pi R^2\dot{R}^2h\left\{\frac{1}{30}\left(\frac{1}{R^2} - \frac{1}{R_\infty^2}\right) + \frac{1}{12h^2}\log\frac{R_\infty}{R}\right\} \tag{B.20}$$

$$\varphi = F_D\dot{R} = 144\mu\pi R^2\dot{R}^2h\left\{\frac{1}{30}\left(\frac{1}{R^2} - \frac{1}{R_\infty^2}\right) + \frac{1}{12h^2}\log\frac{R_\infty}{R}\right\} \tag{B.21}$$

$$F_D = 144\mu\pi R^2\dot{R}h\left\{\frac{1}{30}\left(\frac{1}{R^2} - \frac{1}{R_\infty^2}\right) + \frac{1}{12h^2}\log\frac{R_\infty}{R}\right\} \tag{B.22}$$

Combining the results for all three terms, we arrive at the momentum equation

$$\frac{12}{5}\pi\rho h\left\{(R^2\ddot{R} + R\dot{R}^2)\log\frac{R}{R_\infty} + \frac{1}{2}\dot{R}^2R\right\} \tag{B.23}$$

$$= 2\pi Rh(p_\infty - p_v) + 144\mu\pi R^2\dot{R}h\left\{\frac{1}{30}\left(\frac{1}{R^2} - \frac{1}{R_\infty^2}\right) + \frac{1}{12h^2}\log\frac{R_\infty}{R}\right\} \tag{B.24}$$

$$(R\ddot{R} + \dot{R}^2)\log\frac{R}{R_\infty} + \frac{1}{2}\dot{R}^2 = \frac{5}{6}\frac{(p_\infty - p_V)}{\rho} + 20\nu R\dot{R}\left\{\frac{1}{10}\left(\frac{1}{R^2} - \frac{1}{R_\infty^2}\right) + \frac{1}{4h^2}\log\frac{R_\infty}{R}\right\} \tag{B.25}$$

References

[1] J. Kim, "Review of nucleate pool boiling bubble heat transfer mechanisms", International Journal of Multiphase Flow **35**, 1067–1076 (2009).

[2] V. K. Dhir, "Boiling heat transfer", Ann. Rev. Fluid Mech. **30**, 365–401 (1998).

[3] Lord Rayleigh, "On the pressure developed in a liquid during the collapse of a spherical cavity", Phil. Mag. **34**, 94–98 (1917).

[4] M. S. Plesset and S. A. Zwick, "The growth of vapor bubbles in superheated liquids", J. Appl. Phys. **25**, 493–500 (1954).

[5] H. K. Forster and N. Zuber, "Growth of a vapor bubble in a superheated liquid", J. Appl. Phys. **25**, 474–478 (1954).

[6] B. B. Mikic, W. M. Rohsenow, and P. Griffith, "On bubble growth rates", Int. J. Heat Mass Transfer. **13**, 657–666 (1970).

[7] P. Dergarabedian, "The rate of growth of vapor bubbles in superheated water", J. Appl. Mech. **20**, 537–545 (1953).

[8] A. Asai, T. Hara, and I. Endo, "One-dimensional model of bubble growth and liquid flow in bubble jet printers", Japan. J. Appl. Phys. **26**, 1794–1801 (1987).

[9] A. Asai, "Application of the nucleation theory to the design of bubble jet printers", Japan. J. Appl. Phys. **28**, 909–915 (1989).

[10] A. Asai, "Bubble dynamics in boiling under high heat flux pulse heating", J. Heat Transfer. **113**, 973–979 (1991).

[11] R. R. Allen, J. D. Meyer, and W. R. Knight, "Thermodynamics and hydrodynamics of thermal ink jets", Hewlett-Packard J. **36**, 21–27 (1985).

[12] L. Lin, A. P. Pisano, and A. P. Lee, "Microbubble powered actuator", Proceedings of the International Conference on Solid-State Sensors and Actuators. 1041–1044 (1991).

[13] D. M. van den Broek and M. Elwenspoek, "Explosive micro-bubble actuator", Proc. Transducers. **2**, 2441 (2007).

[14] J. Tsai and L. Lin, "A thermal-bubble-actuated micronozzle-diffuser pump", J. Microelectromech. Syst. **11**, 665–671 (2002).

[15] Z. Yin and A. Prosperetti, "'Blinking bubble' micropump with microfabricated heaters", J. Micromech. Microeng. **15**, 1683–1691 (2005).

[16] R. Dijkink and C. D. Ohl, "Laser-induced cavitation based micropump", Lab Chip. **8**, 1676–1681 (2008).

[17] T. H. Wu, L. Gao, Y. Chen, K. Wei, and P. Y. Chiou, "Pulsed laser triggered high speed microfluidic switch", Appl. Phys. Lett. **93**, 144102 (2008).

[18] A. N. Hellman, K. R. Rau, H. H. Yoon, S. Bae, J. F. Palmer, K. S. Phillips, N. L. Allbriton, and V. Venugopalan, "Laser-induced mixing in microfluidic channels", Anal. Chem. **79**, 4484–4492 (2007).

[19] C. D. Ohl, M. Arora, R. Dijkink, V. Janve, and D. Lohse, "Surface cleaning from laser-induced cavitation bubbles", Appl. Phys. Lett. **89**, 074102 (2006).

[20] H. Yuan, H. N. Oguz, and A. Prosperetti, "Growth and collapse of a vapor bubble in a small tube", Int. J. Heat Mass Transfer. **42**, 3643–3657 (1999).

[21] R. Scardovelli and S. Zaleski, "Direct numerical simulation of free-surface interfacial flow", Annu. Rev. Fluid. Mech. **31**, 567–603 (1999).

[22] S. Osher and R. P. Fedkiw, "Level Set methods: an overview and some recent results", J. Comput. Phys. **169**, 463–502 (2001).

[23] S. O. Unverdi and G. Tryggvason, "A front-tracking method for viscous, incompressible, multi-fluid flows", J. Comput. Phys. **100**, 25–37 (1992).

[24] J. Glimm, J. W. Grove, X. L. Li, K. Shyue, Y. Zeng, and Q. Zhang, "Three dimensional front tracking", SIAM J. Sci. Comput. **19**, 703–727 (1998).

[25] J. A. Sethian and P. Smereka, "Level set methods for fluid interfaces", Annu. Rev. Fluid Mech. **35**, 341–372 (2003).

[26] G. Ryskin and L. G. Leal, "Orthogonal mapping", J. Comput. Phys. **50**, 71–100 (1983).

[27] G. Ryskin and L. G. Leal, "Numerical solution of free-boundary problems in fluid mechanics. part 2", J. Fluid. Mech. **148**, 19–35 (1984).

[28] M. J. Fritts, D. E. Fyre, and E. S. Oran, "Numerical simulations of fuel droplet flows using a Lagrangian triangular mesh", NASA CR-168263. (1983).

[29] B. J. Daly, “Numerical study of the effect of surface tension on interface instability”, Phys. Fluids. **12**, 1340–1354 (1969).

[30] B. J. Daly, “A technique for including surface tension effects in hydrodynamic calculations”, J. Comput. Phys. **4**, 97–117 (1969).

[31] F. H. Harlow and J. E. Welch, “Numerical calculation of time-dependent viscous incompressible flow of fluid with a free surface”, Phys. Fluid. **8**, 2182–2189 (1965).

[32] C. W. Hirt and B. D. Nichols, “Volume of fluid (VOF) method for the dynamics of free boundaries”, J. Comput. Phys. **39**, 201–226 (1981).

[33] W. F. Noh and P. Woodward, “Slic (simple line interface calculation)”, Proc. 5th Int. Conf. Fluid Dyn. **59**, 330–340 (1976).

[34] W. J. Rider and D. B. Kothe, “Reconstructing volume tracking”, J. Comput. Phys. **141**, 112–152 (1998).

[35] D. L. Youngs, “Time-dependent multi-material flow with large fluid distortion”, Numerical Methods for Fluid Dynamics, edited by K.W. Morton and M.J. Baines (Academic Press, New York, 1982), p.273 .

[36] S. Osher and J. Sethian, “Fronts propagating with curvature dependent speed: algorithms based on Hamilton-Jacobi formulations”, J. Comput. Phys. **79**, 12–49 (1988).

[37] D. Chopp, “Computing minimal surfaces via level set curvature flow”, J. Comput. Phys. **106**, 77–91 (2002).

[38] M. Sussman, P. Smereka, and S. Osher, “A level set approach for computing solutions to incompressible two-phase flow”, J. Comput. Phys. **114**, 146–159 (1994).

[39] J. Sethian, “A fast marching level set method for monotonically advancing fronts”, Proc. Nat. Acad. Sci. **93**, 1591–1595 (1996).

[40] G. Russo and P. Smereka, “A remark on computing distance functions”, J. Comput. Phys. **163**, 51–67 (2000).

[41] D. Enright, R. Fedkiw, J. Ferziger, and I. Mitchell, “A hybrid particle level set method for improved interface capturing”, J. Comput. Phys. **183**, 83–116 (2002).

[42] M. Sussman and E. Fatemi, "An efficient, interface-preserving level set redistancing algorithm and its applications to interfacial incompressible fluid flow", SIAM J. Sci. Comput. **20**, 1165–1191 (1999).

[43] M. Sussman and E. G. Puckett, "A coupled level set and volume-of-fluid method for computing 3d and axisymmetric incompressible two-phase flows", J. Comput. Phys. **162**, 301–337 (2000).

[44] M. Sussman, "A second order coupled level set and volume-of-fluide method method for computing growth and collapse of vapor bubbles", J. Comput. Phys. **187**, 110–136 (2003).

[45] L. Lee and R. J. Leveque, "An immersed interface method for incompressible Navier-Stokes equations", SIAM J. Sci. Comput. **25**, 832–856 (2003).

[46] B. T. Helenbrook, L. Martinelli, and C. K. Law, "A numerical method for solving incompressible flow problems with a surface of discontinuity", J. Comput. Phys. **148**, 366–396 (1999).

[47] R. P. Fedkiw, T. Aslam, B. Merriman, and S. Osher, "A non-oscillatory Eulerian approach to interfaces in multimaterial flows (the Ghost Fluid Method)", J. Comput. Phys. **152**, 457–492 (1999).

[48] M. Kang, R. P. Fedkiw, and X. D. Liu, "A boundary condition capturing method for multiphase incompressible flow", J. Sci. Comput. **15**, 323–360 (2000).

[49] S. W. J. Welch, "Local simulation of two-phase flows including interface tracking with mass transfer", J. Comput. Phys. **121**, 142–154 (1995).

[50] G. Son and V. K. Dhir, "Numerical simulation of saturated film boiling on a horizontal surface", J. Heat Transfer. **119**, 525–533 (1997).

[51] D. Juric and G. Tryggvason, "Computations of boiling flows", Int. J. Multiphase Flow. **24**, 387–410 (1998).

[52] S. W. J. Welch and J. Wilson, "A volume of fluid based method for fluid flow with phase change", J. Comput. Phys. **160**, 662–682 (2000).

[53] G. Son and V. K. Dhir, "Numerical simulation of film boiling near critical pressures with a level set method", J. Heat Transfer. **120**, 183–192 (1998).

[54] A. Esmaeeli and G. Tryggvason, "Direct numerical simulations of boiling flows", Proceedings of the Fourth International Conference on Multiphase Flow,IMCF-2001, New Orleans, Louisiana .

[55] G. Son and V. K. Dhir, "A level set method for analysis of film boiling on an immersed solid surface", Numerical Heat Transfer. **52**, 153–177 (2007).

[56] E. Ory, H. Yuan, A. Prosperetti, S. Popinet, and S. Zaleski, "Growth and collapse of a vapor bubble in a narrow tube", Physics of Fluids **12**, 1268–1277 (2000), URL `http://link.aip.org/link/?PHF/12/1268/1`.

[57] T. Ye and J. L. Bull, "Direct numerical simulations of micro-bubble expansion in gas embolotherapy", ASME J. Biomech. Eng. **126**, 745–759 (2004).

[58] A. Mukherjee and S. G. Kandlikar, "Numerical simulation of growth of a vapor bubble during flow boiling of water in a microchannel", Microfluidics and Nanofluidics **1**, 137–145 (2005).

[59] Y. Suh and G. Son, "A level-set method for simulation of a thermal inkjet process", Numerical Heat Transfer. Part B. **54**, 138–156 (2008).

[60] Y. Hong, N. Ashgriz, J. Andrews, and H. Parizi, "Numerical simulation of growth and collapse of a bubble induced by a pulsed microheater", J. MEMS **13**, 857–869 (2004).

[61] M. S. Plesset and A. Prosperetti, "Bubble dynamics and cavitation", Annu. Rev. Fluid Mech. **9**, 145–185 (1977).

[62] C. E. Brennen, *Cavitation and Bubble Dynamics* (Oxford University, Oxford) (1995).

[63] M. P. Brenner, S. Hilgenfeldt, and D. Lohse, "Single-bubble sonoluminescence", Rev. Mod. Phys. **74**, 425–484 (2002).

[64] A. Mazouchi and G. M. Homsy, "Thermocapillary migration of long bubbles in cylindrical capillary tubes", Phys. Fluids. **12**, 542–549 (2000).

[65] V. S. Ajaev, G. M. Homsy, and S. J. S. Morris, "Dynamic response of geometrically constrained vapor bubbles", J. Colloid Interface Sci. **254**, 346–354 (2002).

[66] V. S. Ajaev and G. M. Homsy, "Modeling shapes and dynamics of confined bubbles", Annu. Rev. Fluid Mech. **38**, 277–307 (2006).

[67] H. Yuan and A. Prosperetti, "The pumping effect of growthing and collapsing bubbles in a tube", J. Micromech. Microeng. **9**, 402–413 (1999).

[68] Z. Yin and A. Prosperetti, "A microfluidic 'blinking bubble' pump", J. Micromech. Microeng. **15**, 1–9 (2005).

[69] T. K. Jun and C. J. Kim, "Microscale pumping with traversing bubbles in microchannels", Solid-state sensor and actuator workshop (Hilton Head Island). 144–147 (1996).

[70] T. K. Jun and C. J. Kim, "Valveless pumping using traversing vapor bubbles in microchannels", J. Appl. Phys. **83**, 5658–5664 (1998).

[71] Z. Yin, A. Prosperetti, and J. Kim, "Bubble growth on an impulsively powered microheater", Int. J. Heat Mass Transfer. **47**, 1053–1067 (2004).

[72] E. Zwaan, S. Le-Gac, K. Tsuji, and C. D. Ohl, "Controlled cavitation in microfluidic systems", Physical Review Letters **98**, 254501 (2007).

[73] B. Yang and A. Prosperetti, "Vapour bubble collapse in isothermal and non-isothermal liquids", J. Fluid Mech. **601**, 253–279 (2008).

[74] L. D. Landau and E. M. Lifshitz, *Statistical Physics* (Pergamon Press, Oxford) (1980).

[75] D. R. Lide and W. M. H. (editors), *CRC Handbook of Chemistry and Physics* (Internet Version 2010) (2010).

[76] A. Harten, B. Engquist, S. Osher, and S. Chakravarthy, "Uniformly high order accurate essentially non-oscillatory schemes III", J. Comput. Phys. **71**, 231–303 (1987).

[77] S. Osher and C. W. Shu, "High order essentially non-oscillatory schemes for Hamilton-Jacobi equations", SIAM J. Numer. Anal. **28**, 902–921 (1991).

[78] C. W. Shu and S. Osher, "Efficient implementation of essentially non oscillatory shock capturing schemes", J. Comput. Phys. **77**, 439–471 (1988).

[79] C. W. Shu and S. Osher, "Efficient implementation of essentially non oscillatory shock capturing schemes II", J. Comput. Phys. **83**, 32–78 (1989).

[80] G. S. Jiang and D. Peng, "Weighted ENO schemes for Hamilton Jacobi equations", SIAM J. Sci. Comput. **21**, 2126–2143 (2000).

[81] G. S. Jiang and C. W. Shu, "Efficient implementation of weighted ENO schemes II", J. Comput. Phys. **126**, 202–228 (1996).

[82] A. J. Chorin, "Numerical solution of the navier-stokes equations", Math. Comput. **22**, 745 (1968).

[83] F. Gibou, R. P. Fedkiw, L. Cheng, and M. Kang, "A second order accurate symmetric discretization of the poisson equation on irregular domains", J. Comput. Phys. **176**, 205–227 (2002).

[84] S. Tanguy, T. Mnard, and A. Berlemont, "A mevel met method for vaporizing two-phase flows", J. Comput. Phys. **221**, 837–853 (2007).

[85] S. Popinet and S. Zaleski, "Bubble collapse near a solid boundary: a numerical study of the influence of viscosity", J. Fluid Mech. **464**, 137–163 (2002).

[86] S. Osher and R. Fedkiw, *Level Set Methods and Dynamic Implicit Surfaces* (Springer-Verlag, New York) (2003).

[87] F. Gibou and R. Fedkiw, "A fourth order accurate discretization for the Laplace and heat equations on arbitrary domains, with applications to the stefan problem", J. Comput. Phys. **202**, 577–601 (2004).

[88] A. du Chene, C. Min, and F. Gibou, "Second order accurate computation of curvatures in a level set framework using novel high order reinitialization schemes", SIAM J. Sci. Comput. **35**, 114–131 (2007).

[89] J. U. Brackbill, D. B. Kothe, and C. Zemach, "A continuum method for modeling surface tension", J. Comput. Phys. **100**, 335–354 (1992).

[90] R. Verzicco and P. Orlandi, "A finite-difference scheme for three-dimensional incompressible flows in cylindrical coordinates", J. Comput. Phys. **123**, 402–414 (1995).

[91] S. Prosperetti and G. T. (editors), *Computational methods for multiphase flow* (Cambridge University Press, Cambridge) (2007).

[92] T. Aslam, "A partial differential equation approach to multidimensional extrapolation", J. Comput. Phys. **193**, 349–355 (2004).

[93] S. Popinet and S. Zaleski, "A front-tracking algorithm for accurate representation of surface tension", Int. J. Numer. Methods. Fluids. **30**, 775–793 (1999).

[94] M. Seifollahi, E. Shirani, and N. Ashgriz, "An improved method for calculation of interface pressure force in PLIC-VOF methods", European Journal of Mechanics B/ Fluids **27**, 1–23 (2008).

[95] B. Yang and A. Prosperetti, "A second-order boundary-fitted projection method for free-surface flow computations", J. Comput. Phys. **213**, 574–590 (2006).

[96] L. Florschuetz and B. Chao, "On the mechanics of vapour bubble collapse", J. Heat. Transfer. **87**, 209–220 (1965).

[97] Y. Hao and A. Prosperetti, "The collapse of vapor bubbles in a spatially non-uniform flow", Intl. J. Heat Mass Transfer. **43**, 3539–3550 (2000).

[98] H. N. Oguz and A. Prosperetti, "Dynamics of bubble growth and detachment from a needle", J. Fluid Mech. **257**, 111–145 (1993).

[99] Y. Hao and A. Prosperetti, "The dynamics of vapour bubbles in acoustic pressure fields", Phys. Fluids. **11**, 2008–2019 (1999).

[100] D. Adelsteinsson and J. A. Sethian, "A fast level set method for propagating interfaces", J. Comput. Phys. **118**, 269–277 (1995).

[101] D. Peng, B. Merriman, S. Osher, H. Zhao, and M. Kang, "A PDE based fast local level set method", J. Comput. Phys. **155**, 410–438 (1999).

[102] W. L. Nyborg and D. L. Miller, "Biophysical implications of bubble dynamics", App. Sci. Res. **38**, 17–24 (1982).

[103] C. D. Ohl, M. Arora, R. Dijkink, N. de Jong, M. Versluis, M. Delius, and D. Lohse, "Sonoporation from jetting cavitation bubbles", Biophys. J. **91**, 4285–4295 (2006).

Summary and Outlook

Understanding the behavior of vapor bubbles in confined geometries has become increasingly important with the development of microfluidics in view of the many applications that rely on the rapid dynamics of these entities. Studying these systems theoretically has not been easy due to the complexity of the problem. The difficulties consist of the extreme transient nature of the bubble shape, the presence of solid walls and the occurrence of phase change. For this reason models developed for vapor bubble dynamics tend to depend on oversimplifying assumptions. Typically the bubble is modeled as one-dimensional and furthermore evaporation and condensation are neglected in most studies.

In chapter 2 we study the dynamics of a vapor bubble growing and collapsing in a microtube both experimentally and theoretically. We model the bubble as one-dimensional and show that a quantitative correspondence with the experimental data is not acquired when thermal effects are neglected. Rather it is made clear that thermal effects play a significant role throughout the growth and collapse, so that the usual attitude of assuming these effects to be of minor importance is shown to be erroneous.

Models such as those described in chapter 2 are useful for gaining a basic understanding of the bubble dynamics but it is clear that a more complete picture must be pursued by different means. The last two decades have seen a rapid development of numerical methods capable of computing two-phase flows including phase change effects. These methods have now reached a level of sophistication where physically realistic results can be obtained. The primary objective of this thesis concerns the development and implementation of a numerical method capable of simulating vapor bubbles in confined geometries.

For this purpose the governing equations, put forth in chapter 3, describing conservation of mass, momentum and energy need to be solved with the correct boundary conditions. In chapter 4 the numerical method which has been developed and implemented is described in detail. The method is based on a finite difference discretization of the governing equations on a fixed staggered uniform grid, in cylindrical coordinates and assuming axial symmetry. The equations are solved only for the liquid

phase. The vapor bubble is modeled as a region with spatially uniform but time dependent temperature and pressure. Essentially then, the effect of the vapor is reduced to providing the pressure and temperature conditions at the interface. The vapor-liquid interface is captured implicitly by means of the Level Set method. In order to impose the conditions that hold on the interface and to facilitate the discretization of the equations near to it, a novel method of velocity extrapolation is developed. This extrapolation satisfies the incompressibility constraint resulting in a more accurate advection of the interface. The bubble dynamics and fluid flow are strongly dependent on the interface conditions. Therefore, it is extremely important that the thermal gradients at the interface are approximated with a high degree of accuracy. To achieve this the energy equation is solved on a separate grid with a higher resolution. This can be done without increasing the computation time because the domain on which the thermal equation is solved can be decreased significantly. The reason for this is the fact that the temperature field typically shows variations only in the immediate neighborhood of the bubble. Quantities needed on both grids are computed by means of linear interpolation.

The numerical method is validated in chapter 5 by means of several test cases. By simulating a static bubble in equilibrium we find the magnitude of spurious currents arising from the discretization of interface curvature to be negligible. The temporal and spatial accuracy of the method are determined from simulation of a bubble undergoing damped volume oscillations. The spatial accuracy is found to be second order while the temporal accuracy is determined to be first order. The accuracy of the thermo-mechanical coupling is studied by simulating a collapsing vapor bubble in a subcooled liquid. Due to the particularly strong coupling between thermal and inertial effects this test is extremely stringent from a computational point of view. Even though converged results are not obtained for this case, the method was able to capture the rebound which the bubble undergoes in the very early stages of collapse.

The growth and collapse of a laser pulse induced vapor bubble in a microtube are studied in chapter 6 once more but this time by means of the numerical method. Performing simulations with the exact experimental parameters requires too much computational effort with the current implementation. Therefore they are carried out assuming a tube much shorter than used in the experiments. Furthermore, due to the unknown initial energy distribution in the liquid a direct comparison with experiment is difficult to achieve. Nevertheless, it is found that not only the trend of the dynamics are captured excellently by the numerical method but also the prediction of the bubble shape during the whole process corresponds well to those seen in experiment. Due to the shorter tube the bubble lifetime predicted by the simulations is much shorter. A scaling argument is given to reconcile the difference. The initial

liquid temperature distribution, which is unknown, influences greatly the subsequent bubble dynamics. Various simulations are carried out with varying initial conditions in order to understand their effects on the dynamics. The temperature distribution is characterized by two parameters; the difference between initial vapor temperature and the temperature far from the bubble as well as the initial thermal boundary layer. We find that the latter strongly affects the maximum size that the bubble attains. A thin boundary layer is able to transport the energy released by the condensation of the vapor efficiently resulting in a smaller maximum bubble size.

The growth and collapse of a vapor bubble in a second type of confinement provided by two parallel glass discs is studied in chapter 7. In the same spirit as the tube geometry two models are developed based on the cylindrical Rayleigh-Plesset equation. One neglecting thermal effects, the other including them. The models are applied for various values of the distance between the glass discs. It is found that for this geometry the models are not as successful in describing the experimental data. The numerical method is used for simulating the bubble dynamics in this geometry. Once more the trend of the dynamics is captured very well. The evolution of the temperature field shows qualitatively the same features as that of the tube geometry. However, the bubble shape develops quite differently. Instead of remaining convex as was the case for the bubble in the tube, here the bubble edge becomes concave during its collapse. This is determined to be the result of the much higher velocities which conservation of kinetic energy requires for these converging flows. A contributing factor is the smaller surface tension effects compared to the tube geometry, therefore the inward folding of the interface is not prevented. The prediction of the concave bubble shape is further corroborated by means of calculations based on geometrical optics in which the trajectories of light rays through the bubble are computed. It is found that the bright/dark ring structures that are seen in the experimental data are indeed due to the refraction and reflection of light rays at a bubble with a concave edge.

Improvements and outlook

The main limiting factor of the current implementation of the numerical method is its speed. The computation time needed to perform simulations in which grid independent results are obtained grows quickly with increasing grid resolution The parts of the method that require most of the computational effort are solving the pressure Poisson equation and the high order methods used for the advection and reinitialization of the level set function. Several aspects can be improved in order to speed up the computations.

- Currently the level set function is defined in the whole computational domain while it is needed only in the close neighborhood of the interface. For this reason it is useful to implement the so-called ”narrow band approach” [100, 101] in which the level set treatment is localized in a region close to the interface thus saving much computational effort.

- The libraries used in the current code have the means of solving the Poisson equation using multi-grid techniques. This avenue must be pursued in the future for optimization of the code.

- The grids used in the current implementation are uniform. In combination with the fact that the vapor bubble typically comprises only a small part of the domain it is evident that most of the computational effort is spent in regions of low interest. The most advanced technique of dealing with the existence of different spatial scales uses adaptive grid refinement. However, the implementation of this technique is extremely complex. The problems that are suitable for the current method however typically require a high resolution in a fixed part of the domain. For instance, the vapor bubble growing and collapsing in a tube acquires a certain maximum size which is much smaller than the tube length. Therefore the simulation would benefit from a grid with high resolution in the part of the tube where the bubble resides, while in the region far from the bubble a lower resolution may be used. The implementation of such fixed non-uniform grids should not be too problematic, the rewards however would be great.

With these improvements in mind the type of problems that can be studied using the free surface method are diverse. The rather fundamental subject of this thesis can be studied in more detail by performing a parametric study on the various effects of viscosity, surface tension, aspect ratio of the tube (or discs) etc.

Other interesting situations may be envisaged such as the micro-bubble actuator fabricated in [13]. This device consist of a liquid filled cavity with a resistive heater on the lower wall and a membrane as its top wall. A vapor bubble nucleates by means of a short but intense electric pulse through the heater element. The subsequent bubble dynamics is extremely rapid and violent setting the fluid in motion which results in the deflection of the membrane. The motion of the bubble and the subsequent motion of the membrane are coupled which may be difficult to simulate in full. However, the membrane deflection is small compared to the dimensions of the cavity so that with appropriate approximations for the coupling the numerical method can be used to study the characteristics of this device.

Another problem of interest is the dynamics of an ultrasound driven microbubble situated near a solid wall. Such bubbles are used for instance in the medical community for their ability to induce cell membrane permeability which enhances drug uptake for the cell [102, 103]. The mechanism for this process is intricately connected to the bubble dynamics and the induced flows but it is not understood well yet. This configuration may be readily simulated treating the acoustic field as a time-dependent pressure boundary condition.

Samenvatting

De studie naar het gedrag van dampbellen in begrensde geometriën is steeds belangrijker geworden vanwege de ontwikkeling van de vloeistof fysica op microschaal. Veel applicaties ontwikkeld in dit veld werken op basis van de snelle en krachtige dynamica van deze dampbellen. De theoretische beschrijving van deze entiteiten wordt bemoeilijkt door de veranderende belvorm, de aanwezigheid van vaste wanden en de verdamping/condensatie processen die plaatsvinden. Modellen die ontwikkeld zijn voor het beschrijven van deze processen hebben hierom de neiging om de complexiteiten te versimpelen of compleet te negeren. De bel wordt gewoonlijk als één-dimensionaal gemodelleerd en fase overgangen worden vaak genegeerd.

In hoofdstuk 2 bestuderen we de groei en ineenstorting van een dampbel in een micro-tube op zowel experimentele als theoretische wijze. Ook wij modelleren de bel hier als zijnde één-dimensionaal en we laten zien dat de experimentele data niet goed beschreven kan worden wanneer de thermische effecten verwaarloosd worden. We laten zien dat juist deze effecten een grote rol spelen gedurende het gehele proces en niet alleen tijdens de initiele groei. De gewoonlijke houding dat de thermisch effecten maar een kleine rol spelen wordt dus als incorrect beschouwd.

Modellen zoals beschreven in 2 zijn nuttig om een basis begrip te verkrijgen van de dynamica, maar het is duidelijk dat een beter begrip verkregen moet worden via andere middelen. De laatste twintig jaar hebben numerieke methoden die twee-fase stromingen met fase overgangen kunnen simuleren een snelle ontwikkeling doorgemaakt. Deze methoden zijn tegenwoordig in staat om fysisch relevante resultaten te genereren. Het primaire doel van dit proefschrift is het ontwikkelen en implementeren van een numerieke methode waarmee dampbellen in begrensde geometriën gesimuleerd kunnen worden.

Hiervoor moeten de geldende vergelijkingen voor het systeem met de randvoorwaarden, die in hoofdstuk 3 geintroduceerd worden, opgelost worden. De numerieke methode die geimplementeerd is wordt in hoofdstuk 4 in detail beschreven. De vergelijkingen worden opgelost door middel van eindige verschillen op een uniform rooster in cilindrische coordinaten met de aanname van as-symmetry. De vergelijkingen worden alleen voor de vloeistof opgelost. De dampbel wordt gemodelleerd als

een regio waar een uniforme temperatuur en druk heerst. Deze zijn wel afhankelijk van de tijd. Op deze manier is het effect van de damp gereduceerd tot het bepalen van de druk en temperatuur conditie die moet gelden op het beloppervlak. De belvorm is erg veranderlijk in de tijd. Om de vorm in de tijd te volgen wordt de ”Level Set” methode gebruikt. De snelheid van de vloeistof die berekend wordt vanuit de vergelijkingen wordt geëxtrapoleerd in de dampbel. Dit om de condities te vervullen die op de belwand gelden en tegelijkertijd vergemakkelijkt dit het oplossen van de vergelijkingen. De extrapolatie die wij geïmplementeerd hebben respecteerd de incompressibiliteits conditie van de vloeistof, hetgeen resulteerd in een nauwkeuriger advectie van de beloppervlak. De beldynamica en vloeistof stroming zijn nauw verbonden met de condities de gelden op de belwand. Vandaar dat het erg belangrijk is om een goede approximatie te hebben van de temperatuur gradienten bij de belwand. Om dit te bewerkstelligen wordt de energie vergelijking opgelost op een apart rooster met een hogere resolutie. Dit kan gedaan worden zonder de benodigde rekentijd te vergroten omdat de grootte van het domein waarop de temperatuur opgelost wordt relatief klein gekozen kan worden. De reden hiervoor is dat het temperatuursveld typisch varieert in de directe omgeving van de bel. Ver van de bel is en blijft de temperatuur uniform. De grootheden die op beide roosters nodig zijn worden benaderd door interpolatie.

In hoofdstuk 5 wordt de numerieke methode gevalideerd aan de hand van enkele test situaties. Door het simuleren van een statische bel in evenwicht wordt de grootte van valse stromingen, die gegenereerd worden door de discrete behandeling van de belwand kromming, onderzocht en we laten zien dat hun effect erg klein is. Aan de hand van berekeningen aan een bel die gedempte trillingen uitvoert wordt de nauwkeurigheid van de methode bepaald. De methode is tweede orde nauwkeurig in de ruimte en eerste orde nauwkeurig in de tijd. De koppeling tussen thermische en inertiaal effecten wordt bestudeerd aan de hand van een ineenstortende dampbel in een vloeistof met een temperatuur iets lager dan de kooktemperatuur. Vanuit numeriek oogpunt is dit een zeer veeleisende test vanwege de sterke koppeling tussen de verschillende effecten. Hierdoor zijn geconvergeerde resultaten niet verkregen met de methode. Het was echter wel in staat om de korte periode van groei te berekenen die in de vroege periode van het proces gezien wordt.

In hoofdstuk 6 gebruiken we de numerieke methode om de dynamica van een dampbel in een micro-tube te bestuderen. De parameters die gebruikt zijn voor de simulaties komen niet exact overeen met de experimentele situatie. De reden hiervoor is het feit dat de lengte van de tube erg groot is ten opzichte van zijn diameter, het simuleren hiervan zou te veel tijd kosten met de huidige implementatie van de methode. Daarom is in de simulaties een kortere tube gebruikt. Een directe vergelijking met de experimentele data wordt hierdoor bemoeilijkt. Een ander aspect dat vergeli-

jking met experimenten belemmerd is het feit dat de initiële temperatuursverdeling onbekend is en dus aangenomen moet worden. Desondanks is de trend van de beldynamica berekend met de numerieke methode zeer vergelijkbaar met de trend die gezien wordt vanuit de experimentele data. Ook de belvorm gedurende de groei en ineenstorting van de bel komen goed overeen met de vorm die zichtbaar is vanuit experimenten. Door de kortere tube die in de simulaties gebruikt wordt is de levensduur van de bel veel korter dan die van de experimentel bellen. Een schalings argument wordt gegeven om dit verschil te verzoenen. De onbekende initiële temperatuursverdeling heeft een grote invloed op de bel dynamica. We voeren simulaties uit met verschillende keuzes voor deze grootheid om deze invloed te bestuderen. Het temperatuursveld wordt beschreven door twee paramters; het initiële verschil tussen damp temperatuur en de temperatuur ver van de bel, en de dikte van de thermische grenslaag. We zien dat deze laatste ook erg belangrijk is voor de maximale belgrootte die behaald wordt. Een dunne grenslaag is in staat om de energie die vrijkomt door condensatie efficiënt te transporteren zodat de bel niet de kans krijgt om veel te groeien.

In hoofdstuk 7 bestuderen we de dynamica van een dampbel die groeit en ineenstort tussen twee parallelle glazen schijven. Op dezelfde manier als voor de bel in de tube stellen we twee modellen voor gebaseerd of the cilindrische Rayleigh-Plesset vergelijking. De één beschouwd alleen inertiaal effecten, de ander modelleerd ook thermische effecten. In tegenstelling tot de tube geometrie werken deze modellen niet adequaat. We gebruiken daarna de numerieke methode om deze situatie te simuleren. Ook hier wordt de trend van de dynamica goed voorspeld. De resultaten voor het temperatuursveld zijn kwalitatief vergelijkbaar als die voor de tube. Echter, de belvorm in deze situatie ontwikkeld zich geheel anders. Tijdens het ineenstorten van de bel verandert de vorm van bol naar hol. Dit komt doordat er veel hogere snelheden behaald worden in deze convergerende stromingen. Ook oppervlaktespanning speelt hier een rol. Voor deze geometrie zijn deze effecten kleiner dan voor de tube geometrie, waardoor het ineenvouwen van de bel niet tegengewerkt kan worden. Om na te gaan of deze aspecten van de belvorm fysisch zijn en niet alleen het resultaat van de numerieke methode berekenen we de paden die lichtstralen afleggen door de vloeistof en bel. Hiervoor gebruiken we de geometrische optica. Door belvormen aan nemen met kwalitatief dezelfde eigenschappen als de voorspelde belvormen zijn we in staat om de licht intensiteit profielen die in de experimenten gevonden worden te verklaren, zodat geconcludeerd kan worden dat de voorspelde belvormen inderdaad fysisch zijn.

Verbeteringen en toekomstig werk

De grootste beperkende factor voor de huidige implementatie van de numerieke methode is snelheid. De rekentijd die nodig is voor het verkrijgen van geconvergeerde resultaten groeit snel wanneer de resolutie vergroot wordt. De meeste computationele inspanning ligt bij het oplossen van de Poisson vergelijking voor het druk veld en de methoden die worden gebruikt voor de advectie en herinitialisatie van de Level Set functie die de interface representeerd. Verschillende aspecten kunnen worden verbeterd om de snelheid van de berekeningen te vergroten.

- Momenteel is de Level Set functie gedefinieerd in het hele domein, terwijl deze alleen nodig is in de directe omgeving van de interface. Om deze reden is het zinvol om de zogenaamde ”smalle band aanpak” te implementeren, [100, 101] waarin de functie gedefinieerd word in een smalle regio in de buurt van de interface.

- De bibliotheken die worden gebruikt in de huidige code beschikken over functies waarmee de Poisson vergelijking opgelost kan worden met behulp van multi-grid technieken. Dit kan in een grote toename in snelheid resulteren.

- De roosters die gebruikt worden in de huidige implementatie zijn uniform. In combinatie met het feit dat de dampbel en de omgeving dicht bij de bel slechts een klein deel van het domein beslaan, is het duidelijk dat het grootste gedeelte van de computationele inspanning wordt besteed in regio’s waar men kan volstaan met een lagere resolutie. De meest geavanceerde techniek voor het omgaan met de verschillende ruimtelijke schalen is het gebruik van adaptieve grid verfijning. De implementatie van een dergelijke techniek is echter complex. De problemen die geschikt zijn om met de huidige methode aan te pakken vergen echter doorgaans een hoge resolutie in een deel van het domein dat van te voren bekend is. Bijvoorbeeld, de expanderende dampbel in een buis groeit tot een bepaalde maximale grootte die veel kleiner is dan de lengte van de buis. Voor dit probleem zou een non-uniform rooster gedefinieerd kunnen worden met een hoge resolutie in een fractie van de buis terwijl de resolutie gelijdelijk aan verlaagd word naarmate de afstand tot the maximale belgrootte toeneemt. De implementatie van dergelijke vaste non-uniform grids is veel minder complex.

Met deze verbeteringen in het achterhoofd, kunnen diverse problemen efficient gesimuleerd worden. Het onderwerp van dit proefschrift kan in groter detail bestudeerd worden, door het uitvoeren van een parametrische studie zodat de effecten van vis-

cositeit, oppervlaktespanning, aspect ratio van de buis (of schijven) e.a. apart onderzocht kunnen worden.

Andere interessante situaties kunnen bestudeerd worden, zoals de micro-bel actuator vervaardigd in [13]. Dit systeem bestaat uit een holte gevuld met een vloeistof. Op de bodem van deze holte is een warmte element geplaatst en de bovenkant bestaat uit een membraan. Een dampbel wordt gecreëerd door het insturen van een korte maar zeer intense elektrische puls. De beldynamica is erg snel en explosief, waardoor de vloeistof in beweging komt en daarmee ook het membraan. De dynamica van de bel en membraan vormen een gekoppeld systeem hetgeen numeriek welliswaar moeilijk te simuleren is. De beweging van het membraan is echter veel kleiner dan de afmetingen van de holte zodat met enkele aannames dit systeem toch gesimuleerd kan worden.

Een ander probleem van groot belang is de dynamica van oscillerende microbellen, aangedreven door ultrageluid, gesitueerd nabij een wand. Deze bellen worden bijvoorbeeld gebruikt in medische applicaties vanwege hun vermogen om de permeabiliteit van celmembranen te vergroten, waardoor het opnemen van medicijnen door de cel verhoogt wordt [102, 103]. Het mechanisme hiervoor is nauw verbonden met de beldynamica en de geïnduceerde stromingen. Echter, een goed begrip van dit proces ontbreekt vooralsnog. Dit systeem kan eenvoudig gesimuleerd worden door het akoestische veld te modelleren als een randvoorwaarde voor de druk die tijdsafhankelijk is.

Acknowledgements

I believe that all PhD students, irrespective of particular field or subject, go through times of great frustration, worry and fear of not finishing successfully. The thing that enables one to endure these tough times is the environment that one find himself in. For this reason I am grateful that my environment was the Physics of Fluids group. Despite the tough periods, the past four years were most of all fun. I would therefore like to thank all the people in the group in general for the nice discussions on varied subjects, the coffee breaks and all the help in all forms.

I would like to thank Michel Versluis for first contacting me about doing a PhD when I just started my masters project in a different group. I am grateful to Prof. Detlef Lohse for giving me the opportunity to work in this group, and visit my advisor's group in Balitmore where I had the privilege to study.

I would have never been able to do this work without the excellent guidance of my advisor, Prof. Andrea Prosperetti. I don't know how many times I went into his office proclaiming that the code works, showing him graphs and figures, whereupon he would look at them and suggest doing some other test case. Following his suggestions almost invariably brought to light some error which needed to be fixed. This uncanny knack of seeing through the data and expose errors still leaves me baffled. After so many failures I thought about quitting many times. His patience, continuing encouragement and trust that I would get it to work were the things that kept me from giving up. His suggestions, explanations and help with writing the thesis were invaluable and much appreciated.

The importance of good office mates cannot be stressed enough. I feel lucky I shared an office with Kazuyasu Sugiyama and Enrico Calzavarini during the first two years. Their knowledge on numerical methods is impressive and I learned a lot from them. The final two years I had the pleasure of sharing the office with Stephan Gekle, Daniel Chehata Gómez and Sylvain Joubaud. To all I am grateful for their pleasant nature, and our discussions scientific and otherwise.

I thank Chao Sun for the great experiments concerning the vapor bubble dynamics described in this thesis. His positive take on things and enthusiasm are contagious. I don't think I have ever seen him in a bad mood.

Many questions I directed to Jacco Snoeijer, Gerrit de Bruin and Prof. Leen van Wijngaarden and I always found their doors were open even though no direct connection to my work existed. For this I am grateful to them, their suggestions and explanations always were very useful.

In my view the group runs smoothly for a large part due the the supporting staff. To me Bas Benschop and Joanita Leferink have been of great importance. Thank you for solving all problems quickly, efficiently and with a pleasant character.

Of course life extends outside the workplace. I cannot express how important my family is to me. Thank you for your encouragement, support and love. Finally I thank my wife Sylvia, you are my greatest support.

About the Author

Edip Can was born the 10th of June 1980 in Enschede, the Netherlands. He graduated from high school in 1999 and started studying Applied Physics at the University of Twente later that year. In 2003 he spent three months at Stanford University as an intern working on optical pulse compression by means of an optical grating. In December 2005 he graduated in the Laser Physics group led by Prof. K. J. Boller on a numerical study of ”Coherent Storage and Manipulation of Optical Solitons in Atomic Media”. Hereafter he joined the Physics of Fluids group at the University of Twente to study the dynamics of vapor bubbles in confined geometries, the results of which are described in this thesis.